Investigation of Active Control of Aircraft Wing Tip Vortices and Wake Turbulence

by

Manjul Gupta

A thesis submitted to the Graduate Faculty of
Auburn University
in partial fulfillment of the
requirements for the Degree of
Master of Science

Auburn, Alabama
December 12, 2011

Approved by

Anwar Ahmed, Chair, Professor of Aerospace Engineering
Roy Hartfield, Professor of Aerospace Engineering
Gilbert Crouse, Associate Professor of Aerospace Engineering

Abstract

The present work was focused on study and application of active flow control methods to alleviate the wake turbulence problem in commercial aircraft. Sinusoidal perturbations were introduced into the tip vortex generated off one of the wings in a two wing system. Various forcing frequencies and oscillation amplitudes were investigated in a towing tank facility. Measurement techniques included invasive and non-invasive methodologies such as flow visualization, hot film anemometry and particle image velocimetry (PIV).

Tilting of the plane of the vortices under forcing conditions was observed. The initiation of long-wave Crow instability was observed. This was also confirmed by flow visualization results. For 20Hz forcing frequency, elliptical deformation of the core for both the vortices was observed. This was an indication of short wave Elliptic instability. When perturbed at a particular frequency and amplitude, the overall system showed earlier onset of instabilities.

Acknowledgments

I would like to thank my family for encouraging and providing the resources to allow me to pursue graduate level education at Auburn University. I owe my deepest gratitude to Dr Ahmed, whose encouragement, guidance and support from the beginning to the final stages of this effort helped me to develop a deeper understanding of the subject. I am indebted to many of my colleagues Vivek Ahuja, Hamza Ahmed, Kyle Lynch, Zach Reid, Abhishek Bichal and Manish Kulkarni for their assistance and feedback during the research. I also want to thank Dr Hartfield, Dr Thurow, Dr Crouse and Dr Shelton for their approachability. Thanks also go out to Andy Weldon and Jim Lin for their patience during the manufacturing phases of this research effort.

Lastly, I would like to thank God and all of my family and friends for having faith in me and being my constant source of inspiration. Special thanks go out to Mahesh Gupta, Sadhana Gupta, Ahmed Faraz, Manuj Ahuja, Sapana Shrivastava, and Rohit Kulkarni.

Table of Contents

List of Tables

List of Figures

Nomenclature

GTW	Gross Take-off Weight
AVOSS	Aircraft Vortex Spacing System
LAROF	Low-Aspect-Ratio-Oscillating Flap
AOA	Angle of attack
CCWT	Closed Circuit Water Tunnel
RPM	Revolutions per minute
SVS	Single Vortex System
CRVS	Counter Rotating Vortex System
BVI	Blade Vortex Interaction
Γ	Circulation
V_θ	Resultant velocity
Γ_0	Root circulation
r	Radial distance
a	Vortex core radius
L_0	Lift at the wing root
ρ	Density of air
v	Velocity in y direction
w	Velocity in z direction
$\vec{\omega}$	Vorticity

ω_x	Axial Vorticity
U_∞	Towing velocity
b	Span of the wing
c	Chord length of the wing
A	Amplitude of oscillation (peak to peak)
Re_c	Reynolds number based on chord
Re_Γ	Reynolds number based on circulation
λ	Wavelength of instability
b_0	Initial vortex separation
b_s	Lateral vortex separation
$t^* = tU_\infty / c$	Non-dimensionalised time for SVS
$t^* = t\Gamma_0 / 2\pi b_o^2$	Non-dimensionalised time for CRVS
$\Gamma^* = \Gamma / (U_\infty c)$	Non-dimensionalised circulation
$U^* = V / U_\infty$	Non-dimensionalised maximum velocity
$KE^* = KE / U_\infty^2$	Non-dimensionalised kinetic energy
$\omega^* = \omega c / U_\infty$	Non-dimensionalised vorticity
$a^* = a / c$	Non-dimensionalised vortex core radius
$b^* = b_s / b_0$	Non-dimensionalised lateral separation

Subscripts

∞	Free-stream condition
s	Separation
0	Initial conditions

1. Introduction

1.1 Background

Recent concerns over the hazard posed by trailing vortices (Figure-1.1) generated by a heavy aircraft have stimulated research into one of the oldest subjects in fluid mechanics [1]. The counter rotating vortex pair resulting from this effect represents one of the simplest flow configurations for understanding elementary flow which can yield useful information about the physics of more complex turbulent flows [2]. Lift is generated due to the differential pressure between the upper and lower surfaces of the wings. This pressure difference leads to the creation of vortices that trail behind the aircraft and persist downstream of the vehicle. Immediately behind the generating aircraft is a zone known as the roll-up region, where the nature of the wake that is shed from individual components (wing tips, landing gear, fuselage and flaps) changes rapidly with distance because of self induced velocities (Figure-1.2). Shortly after the rollup region is a wake area known as the plateau region where vortices have either merged if they have the same direction of rotation and/or attained a nearly constant structure. Farther downstream from the generating aircraft is a region known as the decay region, where the vortices decay due to viscous or turbulence [3].

Figure-1.1: Aircraft‘s tip vortices [4]

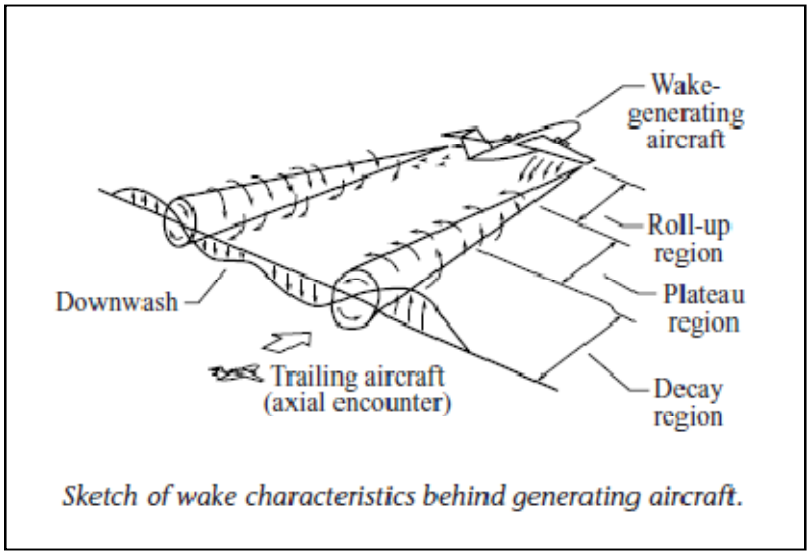

Figure-1.2: Sketch of wake characteristics behind generating aircraft [3]

For heavy and large transport aircraft, velocities in the tip vortices can be strong, long-lived and a serious threat to aircraft encountering the wake, especially small general aviation aircraft. Depending upon the following aircraft’s orientation with respect to the wake of the generating aircraft, the following aircraft experiences an induced rolling moment, an upwash or downwash and consequently increased aerodynamic and structural loads (Figure-1.3) [3]. If an

encounter occurs at low altitudes, especially during the landing approach, loss of control and ground impact may occur. At higher altitudes, the longevity of the wake is not an issue since the likelihood of encounter is extremely small and the aircraft has a time to recover. In the vicinity of airports, however, all aircraft are limited to fly specific air corridors during takeoff and landing, therefore the possibility of encounter is much greater [3]. Depending on the size, weight, distance between the two aircraft and the probability of wake encounter, the severity of wake hazard varies for a given local atmospheric condition that influences the position, merging, strength and decay of vortices. In general, a pair of vortices drifts downward with time behind the generating aircraft and the strategy followed by a pilot for avoiding vortex encounters is for the trailing aircraft to fly at an altitude equal to or higher than the flight path of the leading aircraft. However, on many occasions the vortices may persist at the generated altitude or even move to slightly higher altitude due to the local atmospheric conditions. If the vortices reach the ground, they typically move outward from the aircraft at a speed of about 2 to 3 knots in the calm wind conditions. However, if there is an ambient wind, then the net movement of the vortices will be a resultant of wind velocity and no wind motion of each vortex. Due to the non-deterministic combination effects of these factors, the fundamental nature of wake vortices and their attenuation have been a difficult problem since the early operation of commercial flights. A comprehensive bibliography of work on wake vortex hazard is discussed by Hallock [5].

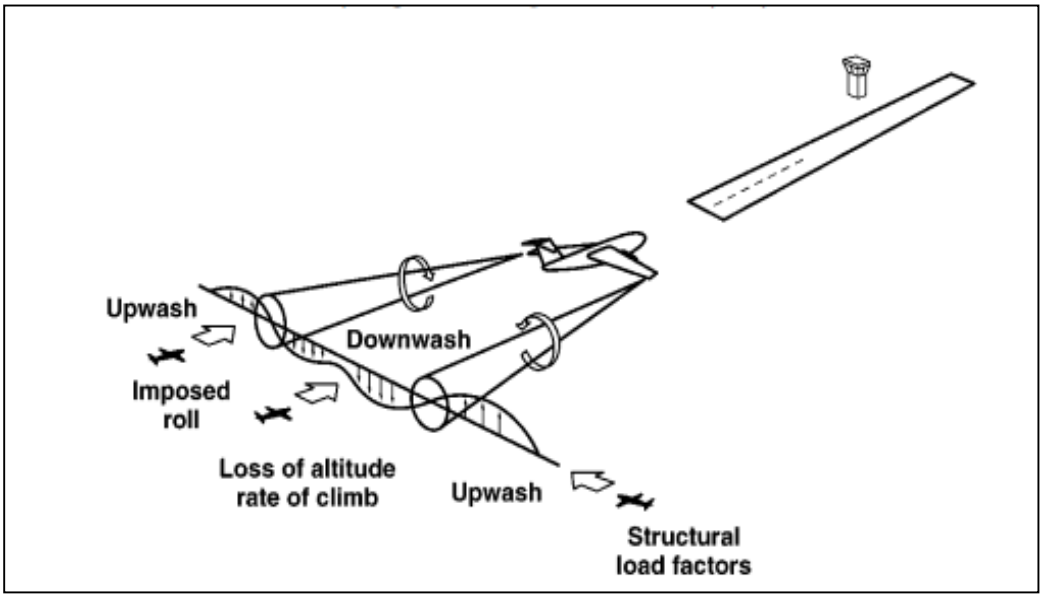

Figure-1.3: Possible encounter of the trailing aircraft with lift generated wake of leading aircraft [3].

In order to understand the physics of trailing vortices, consider an airplane typical load distribution, where section lift L varies from a maximum at the root (L_0) to zero at the wing tips. In the wake of an aircraft, there exist two counter rotating vortices with equal and opposite circulation i.e. ±Γ. According to the potential theory for finite wings, the strength of the vortices is directly related to weight and inversely related to the speed and span of the aircraft. For a steady flight, the lift produced by the aircraft is equal its weight. Therefore, the strength of the circulation is given by Equation-1.1[6]:

$$\Gamma = L_0 / \rho\, U_\infty b \tag{1.1}$$

For takeoff and landing, the aircraft requires with maximum lift. Since the lift is high and the speed is low, the vortices are at their strongest and this magnifies the problem of wake turbulence [6].

The severity of the hazard caused by wake vortex encounters can be gauged by past incidents. In particular, a series of incidents and accidents involving the Boeing-757 during its landing approach resulted in serious concern regarding the wake characteristics of that aircraft. In one such accident on December 18, 1992, a Cessna Citation, trailing a Boeing-757, crashed during a landing approach under VFR at the Billings Logan International Airport, Billings, Montana. The people on-site reported that the aircraft suddenly and rapidly rolled left and then contacted the ground while in a near vertical dive. This is a classic indication of wake vortex encounter. The Citation was about 2.8 nmi behind the Boeing 757 and at a flight altitude which was about 300 ft below the flight path of the 757. This level of separation is below the current FAA standards as is discussed in the next section [3]. Similarly, on December 15, 1993, an Israel Aircraft Industries Westwind, operating at night, crashed on VFR approach to the John Wayne Airport, Santa Ana, California while trailing a Boeing-757. Once again, the people on-site reported that the aircraft lost control and rolled abruptly [3]. The Westwind was about 2.1 nmi behind the Boeing 757 and on a flight altitude which was about 400 ft below the flight path of the 757.

Table-1.1: FAA aircraft weight classification procedure [6]

Category	Maximum Certified Gross Takeoff Weight(GTW)
Heavy	$Weight \geq 255{,}000lb$
Large	41,000 lb$\leq Weight \leq 255{,}000lb$
Small	$Weight \leq 41{,}000lb$

Before 1970, Radar separation limits, and, to a lesser extent, Runway occupancy restrictions dictated aircraft separation standards [3, 7]. These regulatory aircraft separations

were not imposed because of wake vortices. In 1970, NASA, FAA and the industry conducted flight tests to determine the wake vortex characteristics of existing aircraft. Based on these tests, the separation requirements for IFR were established. Until March 1976, separation distances of 5 nmi were required for “non-heavy” aircraft (less than 300,000lb) trailing behind a heavy aircraft (greater than or equal to 300,000lb), and separations of 3 nmi for all other combinations of aircraft. In 1976, the distances were increased, with the maximum being 6 nmi for a “small” aircraft (less than 12,500 lb) trailing a heavy aircraft.

Recently, with an increase in demand for air transportation it is estimated that the air traffic volume will be doubled or even tripled by 2025[8]. As a result, the possibility of trailing aircraft encountering the wake of the leading aircraft has increased significantly. To overcome this hazard, FAA has prescribed mandatory spacing standards that are dependent on the Maximum- Takeoff-Weight (MTOW) of leading and trailing aircraft. The current matrix of required aircraft separations shown in Table-1.1 and Table-1.2 was in response to the introduction of the Boeing-747 in 1970. Shortly after the establishment of these mandatory spacing rules, it was realized that the airport capacity will be affected in the long run and research work was initiated to answer this fundamental problem after 1970 [6].

Table-1.2: FAA separation distance [6]

Following aircraft	Leading Aircraft(Distance in miles)			
	Heavy	B-757	Large	Small
Heavy	4	4	2.5	2.5
Large	5	4	2.5	2.5
Small	5,6	5	3,4	2.5

Helicopter main rotor blades represent another area where vortex-structure interaction compromises structural integrity of the blades. Each rotor blade sheds a tip vortex which interacts with the following blades and the tail-rotor blades. This interaction results in large unsteady forces due to rapid changes in local velocity around the blades. These unsteady forces can cause premature rotor-blade fatigue and excessive noise [9]. This type of noise is large and impulsive in nature and is therefore significant for both military and civilian applications. A rotor blade can intersect a trailing vortex at different angles depending on the blade's azimuth position and the vortex age. The most prominent Blade-Vortex Interaction (BVI) event is one where the trailing vortex is nearly parallel to the blade, usually occurring near azimuth angles of 70 to 80 deg. Parallel-BVI is known to be the strongest and most important event for acoustics because of the brief and dramatic changes the blade experiences along its entire span as it travels through the vortex flow field [10].

Reduction in the strength of tip vortices is beneficial for military applications as well. An example of this is seen during in-flight refueling operations when lighter and smaller combat aircraft fly in close proximity to one of the tip vortices of the tanker aircraft when a hose-and-drogue system of refueling is being used. A second application is vortex breakdown in delta wing aircraft and missile configurations. This phenomenon occurs when the vortex undergoes a rapid transition from high tangential velocities and small core radius to low tangential velocities, reversed axial velocities and large core radius. During this process, vortical fluid experiences large decelerations which are the sole cause of unsteady vortex structure interaction near the location of the breakdown [9].

The current standards limit airport capacities (see Figure-1.4). In most cases, the current standards are enough to avoid wake vortex encounter under the IFR rules but occasionally, they

can still be outlasted by wake vortices. Crouch [11] has reported that there have been experiments and computations suggesting that vortices can remain coherent for larger distances than the spacing rules imposed by current standards.

Figure-1.4 Wake-vortex separation requirements under instrument flight rules conditions aggravate airport capacity problem [3].

1.2 Previous Work

Aircraft spacing rules have become a limiting factor in increasing airport capacity. Expanding the infrastructure of an airport would be next legitimate solution. However the location and cost of upgrades restrict the expansion of most airports in large cities. A more scientific and fundamentally better approach to surmount the wake vortex hazard issue is to find ways of increasing the capacity of airports and runways by understanding the physics of the problem. In this way, counter measures to the problem can be developed instead of circumventing them.

In the 1970's several attempts were made to alleviate this problem. A variety of techniques were explored and a lot of fundamental insights were gained into the problem.

Although some techniques showed promise, none of them were practically applicable on the aircraft. This problem was ignored since air traffic never reached the levels that were initially feared. In the 1990s, when the air traffic again came into spotlight, more attempts were made to tackle this problem with more sophisticated experimental and computational techniques. The strategies that have been explored can be divided into two main categories: a) Detection & Avoidance and b) Wake control & Alleviation

1.2.1 Detection and Avoidance:

The main idea in the case of detection and avoidance is to know the location of wake vortices after the takeoff and landing of an aircraft and determine if they are strong enough to cause any hazard to following aircraft. Since the current spacing rules are based on IFR, modified spacing based on actual scenarios will definitely reduce the necessary spacing and allow for increased numbers of operations (landings and take off).

The main drawback with this strategy is the need to continuously measure the location of vortices in a large airspace with reasonable accuracy. A variety of measurements techniques have been developed for this purpose since the wake vortex hazard first become a problem. Light Detection and Ranging (LIDAR) was the first technique used to measure velocities in the large airspace at long ranges. This technique determines the flow field parameters by measuring the velocity of the aerosols present in the air. Extensive literature on this methodology is available (Huffaker [12]). Simulations were also performed to further study this technique and reasonable analytical solutions were also developed to compliment the simulations (Thomson and Meng [13]). Later, Hannon and Thomson [14] experimented with pulsed lidar rather than CW and showed that although the finite pulse time limits the accuracy of velocity measurements, much

greater ranges (> 2 km) could be achieved. Harris et al. [15] and Keane et al. [16] experimented with a pulsed lidar system oriented in the axial direction to determine if such systems could be used for vortex detection and were successful in measuring the wakes of several large aircraft.

Radar-acoustic detection was another technique developed for accurate measurements of the wake. The main principle in this technique involves overlapping a radar and acoustic beam and quantifying the resulting radar backscatter which occurs due to changes in the refractive index of air caused by the acoustic beam (Rubin [17]). This technique has been confirmed by CW LIDAR measurements. In conjunction with these experiments, it was also validated in numerical studies of Boluriaan and Morris [18]; Boluriaan and Morris [19] and Shariff and Wray [20].

Finally, attempts have been made to integrate a wake detection system, real-time weather predictions and vortex decay and transport predictions into a single system which is able to provide a complete picture. The Aircraft Vortex Spacing System (AVOSS) developed by NASA is an example of such a system. A detailed account of the system is given in Hinton [21].

The main drawback with the detection and avoidance schemes explored to date is that they are costly and error prone. On calm day vortices tend to linger longer without diffusing or decaying. Therefore, even if wake detection system could be made more reliable to predict the vortex path accurately, it would be of no use in reducing current spacing standards. A wake alleviation system tackles the problem more directly.

1.2.2 Wake Alleviation and Control:

Wake alleviation and control schemes rely on altering the characteristics of the vortex wake by altering the thickness, turbulence and longitudinal velocities in the vortex sheet out of which the core is formed. Some of the possibilities that could help to intensify the turbulence diffusion or decay mechanisms are to:

- introduce more turbulence into the rotational/irrotational layers during the roll up process to enhance Helmholtz and Rayleigh instabilities in the discontinuous velocity profiles, to increase the core radius and the overlapping of counter rotating vortices , and to hasten Crow instability and linking[19]
- use structural modification along the trailing edge of the wings and flaps, e.g. wing tip splines , winglets to enhance the three dimensionality of the flow and turbulence in the shear layer after their rollup[20]

These modifications can be achieved either by active control or passive control techniques. Passive control involves alleviation achieved through methods which involve no time dependent forcing where as active control relies on time dependent forcing.

1.2.2.1 Passive Alleviation Schemes:

Passive wake alleviation strategies rely on modifying the structure of the wake using control mechanisms in a static mode with no time dependent forcing. The crux of the technique lies in either modifying the wake rollup so that the resulting vortex wake is benign to the following aircraft or passively exciting some instability in the vortex, resulting in rapid diffusion of vorticity i.e. reduction in strength of the vortex.

Much of the early research into solving the wake vortex hazard passively involved modifying the structure of the wake before roll up by changing the geometry of the body, in turn changing the loading distribution. Rossow [22] performed theoretical studies using 2D inviscid computations to determine the loading distribution which would result in a wake that would either not roll up or have very diffused vorticity fields. Loading distribution where section lift coefficient decreases linearly from root to tip as well as loading distributions with abrupt variation in lift were examined. The results showed that both type of loading distributions resulted in a diffused vorticity field. The wake produced by an optimized loading distribution displayed a notable decrease in the induced rolling moment that would be encountered by the following aircraft compared to the standard case. Holbrook et al [23] performed experiments with a variable twist wing and came to the same general conclusion. Corsiglia and Dunham Jr. [24] performed experiments, including flight test and showed that the standard configuration of a Boeing 747 can be slightly modified to shift the centre of pressure inboard and produce a less hazardous wake. Graham et al. [25] performed tests on a notched loading distribution and showed that it resulted in more diffused wake.

In addition to geometric modification of the wings, a variety of experiments were performed on adding static devices to already existing planforms. Lezius [26] performed flow visualizations in a tow tank on the wing with and without a triangular leading edge extension at the wing tip. He showed that the modified wing tip produced a much more diffuse wake than the clean wing, but no quantitative measurements were made. Patterson [27] experimented with splines mounted directly downstream of the wing tip such that their bluff body shape would interfere directly with the tip vortex. They were found to be effective in increasing the size of the vortex core but they also created a large drag penalty. Other splines as well as various wing tip

shapes were reviewed in experiments by Traub et al. [28] who noted similar results. Croom [29] performed wind tunnel experiments as well as flight tests installing spoilers on the suction side of wings typically used as air brakes on commercial aircraft and observed significant increases in the vortex core size.

A large amount of work has gone into the idea of using fins mounted on the suction or pressure side of wings in order to modify the loading distribution and/or add another discrete vortex to the wake that might interact with the tip vortex in a beneficial way. Rossow [30] performed wind tunnel tests and attempted to determine an optimal placement and orientation for a fin and found that a fin on the suction side of the wing creating a vortex that is counter-rotating with respect to the tip vortex tended to produce the most benign wake. Later, Schell et al. [31], Ozger et al. [32], Heyes and Smith [33] and Scholl et al. [34] experimented with various fin designs on both experimental wings as well as realistic aircraft wing shapes and showed that a more diffused wakes could be achieved. The idea of blowing air jets near the wing tips was examined by Tanaka et al. [35] and later by Simpson et al. [36] and Zhou and Zhang [37]. A significant increase in the dispersion of the tip vortex was observed. Also, the extent to which the tip vortex was perturbed was found to be sensitive to the velocity and position of the jet. Heyes and Smith [33] and Bearman et al. [38] found the similar general trends.

Most recently, other passive techniques have been researched wherein the goal was to use a passive device to excite some natural instability in the trailing vortex system. Ortega et al. [39, 40] performed tow tank experiments with a rectangular wing equipped with triangular flaps at the tips that extend the trailing edge. These flaps create a pair of inboard vortices that are counter-rotating with respect to tip vortices. Various flap sizes were examined such that the strength of the inboard vortices ranged from -40% to -70% of the outboard vortex strength. It

was shown that the vortices generating by flapping undergoes a rapidly growing instability where in the flap vortex is entrained by the outboard vortex in sinusoidal fashion. Stumpf [41] demonstrated the same mechanism numerically using RANS and LES to model the wake of a real aircraft. Durston et al. [42] used tail wings rather than triangular flaps, to produce the same instability with equal success. Haverkamp et al. [43] also followed the work of Ortega et al. using triangular flaps to passively excite the same vortex instability.

The main advantage in using passive techniques is that this would be simpler and less complex to use in practice. The absence of the time dependent forcing allows many of the proposed experimental techniques easy to be implemented. But, the main problem with passive devices is that they come with drag and lift inefficiencies and result in additional fatigue on the planform. The drag and lift efficiency can be taken care of by making sure that the device is on when needed and retracted when not required .However this is likely to increase the weight and complexity of the aircraft.

1.2.2.2 Active Alleviation Schemes

Active wake alleviation strategies rely upon some time-dependent forcing to perturb the wake of an aircraft and excite natural instabilities for rapid decay or attenuation of the vortex system.

In 1970, Crow [44] found that sinusoidal long wavelength instability (Figure-1.5 and Figure-1.6) exists for a pair of counter rotating vortices. The amplitude of instability grows exponentially with time and would likely lead to periodic linking of a vortex pair to produce a series of vortex rings. Atmospheric turbulence was cited a typical method by which this instability is excited. He investigated the breakup of vortices through excitation of instabilities.

Chevalier [45] later performed flight tests that demonstrated how elevator oscillations at a critical frequency could be used to accelerate the dissipation of high-intensity vortices. Later, Crow and Bate [46] came up with the initiative to excite the Crow instability by oscillating the lift distribution to move the vorticity centroid outboard and inboard along the wing. Bilanin and Widnall [47] conducted experiments on a full span NACA 0012 wing equipped with inboard and outboard flaps, of each a quarter span in length. Periodic flap oscillations were used to move a significant fraction of lift inboard and outboard keeping the lift constant to within ± 2%.They showed that the excitation is indeed possible but the level of oscillations in lift required to break up the vortices was excessive. The baseline lift was reduced by active control because part of lift was lost at any time during the forcing cycle.

Barber and Tymczyszyn [48] conducted flight tests with large commercial aircraft wherein lateral-control oscillations in time were made in order to excite the Crow instability. Although the spoiler deflections were too large to be feasible during take-off or landing, they demonstrated that the Crow instability could be excited in this fashion and completely destroy the wake within three nautical miles of the generating aircraft. The tow tank experiments of Jordan [49] further supported this conclusion. Rossow [50] considered the use of roll oscillations of the aircraft as a means for exciting the Crow instability. Although this could be achieved without large oscillations in lift, the passenger discomfort associated with roll oscillations is the main drawback of this strategy.

More up-to-date methods in the effort to break up the vortices endeavored to exploit instabilities that exist for multiple pair of vortices as produced by airplanes with their flaps deployed. This was first investigated by Crouch [51] who focused on the pair of trailing vortices, with co-rotating vortices on either side of the aircraft. The instabilities provoked by multiple

vortex pairs were five times higher than the Crow instability. Crouch, Miller and Spalart [52] tested the scheme based on excitation of multiple vortices instabilities and found that it leads to rapid break up of vortices with lower level of oscillations in lift.

Other recent efforts to break up trailing vortices have considered a pair of counter rotating vortices on each side of an aircraft. Rennich and Lele [53] proposed a scheme based on a special configuration of the vortex system. When the strength and position of the vortices is chosen to allow for four vortices to stay in the plane as they propagate downward, long wavelength perturbations were found to grow very rapidly. This leads to a rapid breakup of the vortices, with a small level of initial perturbations. This was analyzed by Fabre and Jacquin [54] who showed that without forcing, shorter wavelength instabilities dominates leading to the demise of weaker vortices without affecting the stronger vortices. The instability growth rates were very positive for the breakup of vortices but in reality this vortex configuration was very difficult to achieve.

Fabre et al [55] showed that two vortex pairs, with counter rotating vortices on each side can exhibit spectacular instability growth even when the conditions proposed by Rennich and Lele [53] were not met. The vortex tumble with an increase in perturbations has been observed by Ortega [56], Jacquin [57] and Haverkamp [43] et al. This instability leads to rapid break up of weaker vortices on either side of the aircraft. After the demise of the weaker vortices, the perturbations in the stronger vortices were found to be inversely proportional to strength relative to weaker pair. The stronger vortices would decay into vortex rings depending on the growth of perturbations based on wavelength. Kauertz and Neuwerth [58] tried active oscillation of winglets to modify the wake of the aircraft and it was found that the additional oscillations of winglet had no alleviating effect on the induced rolling moment compared to static winglet.

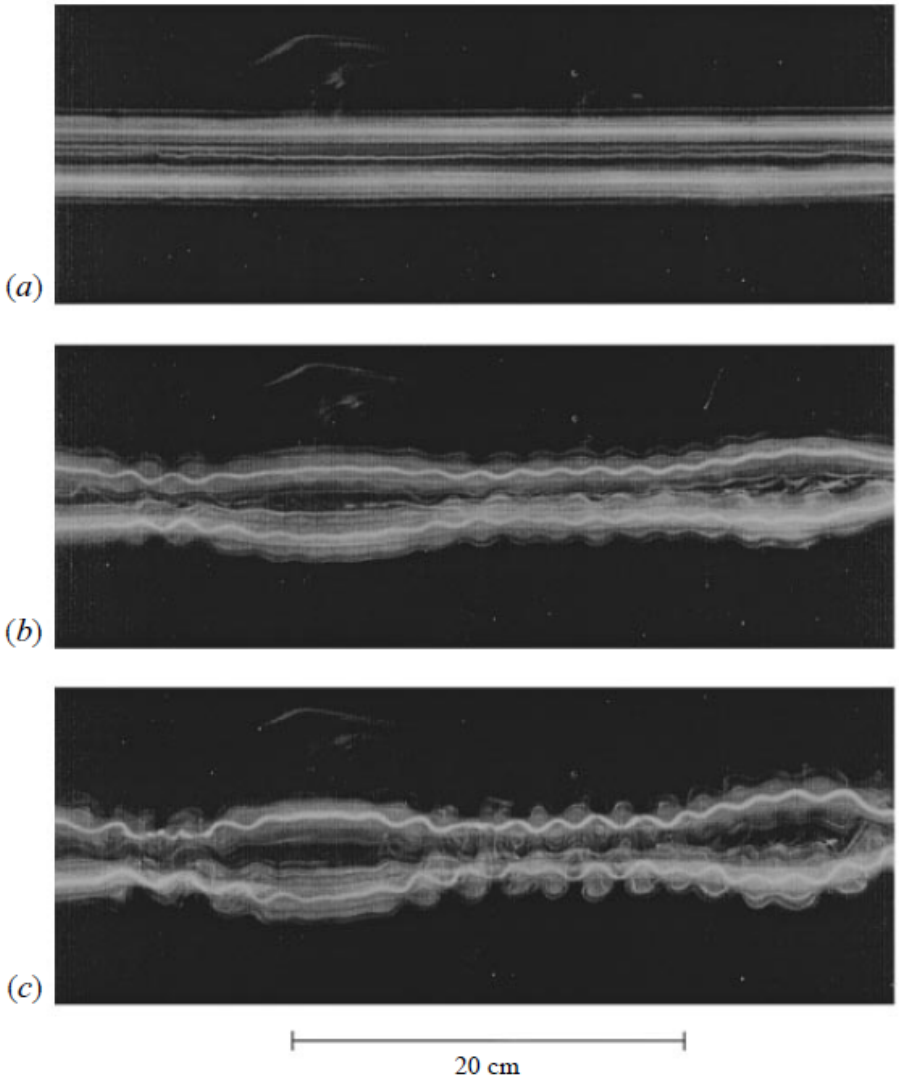

Figure-1.5: Visualization of a vortex pair evolution under the combined action of long wavelength (crow) and short –wavelength instabilities.

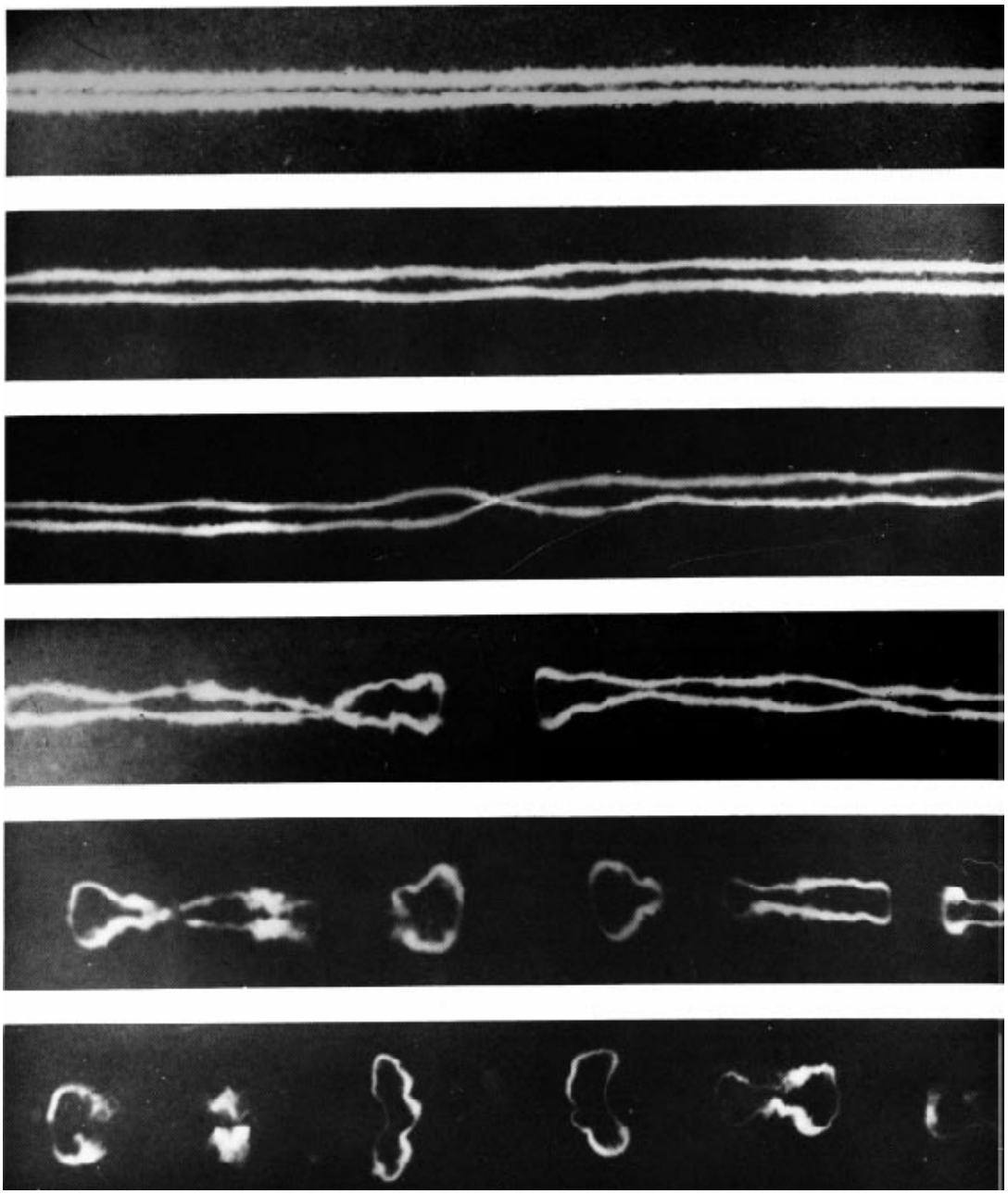

Figure-1.6: Photographs taken at 15 s intervals from below condensation wake of B-47 in cruise configuration to illustrate mutually induced instability of a vortex pair (from Crow [62] and Van Dyke [63], courtesy of Meteorology Research, Inc.).

1.3 Objectives

The objective of the present work is to use active-control techniques to achieve dissipation of the vortices. This will be accomplished by perturbing the vortex using a variable control flap at the outboard end of the trailing edge of a model wing. The effort will focus on the effect of controlled perturbations on the characteristics of a tip vortex in a single vortex system. Also, to study the interaction characteristics of a perturbed tip vortex with an unperturbed tip vortex in a dual vortex system. To investigate the possibilities of exciting instabilities to enhance dissipation of the tip vortex structure using Planar Laser Induced Fluorescence and Particle Image Velocimetry (PIV) methodologies. To investigate the frequency and amplitude dependencies of the control perturbations on the vortex structure using PIV and Hot-Film Anemometry. To investigate the transfer mechanism of the perturbation from the control surfaces to the tip vortex structure. Hot-Film Anemometry will be used. These investigations will be conducted in the water tunnel at the Department of Aerospace Engineering, Auburn University.

2. Experimental Setup

2.1 Overview

The experiments were divided into two categories i.e. the Single Vortex System (SVS) and the Counter Rotating Vortex-pair System (CRVS). As outlined in the objective the following methodologies were required:

a) PLIF : Planar Laser Induced Fluorescence
b) Hot-Film Anemometry
c) PIV: Particle Image Velocimetry

The experiments were conducted in the Auburn University Aerospace Department's Water Tunnel Facility. The water tunnel and instrumentation used are discussed in detail in the following sections.

2.2 Close Circuit Water Tunnel (CCWT) /Towing Tank Facility

The water tunnel is shown in the Figure-2.1. The test section is approximately 2 m long and 0.45 m x 0.45 m in cross-section. It is capable of a maximum speed of 1.1 m/s with a peak free stream turbulence intensity of less than 1%. On the top of the test section, there are precision rails for mounting the model and allow the movement of model on a carriage that can be traversed linearly. Thus, the test-section can be used as tow tank for conduction tests at high velocities.

Figure-2.1: Auburn University water tunnel

2.3 Design:

Wing models used for this effort consisted of a NACA 0012 airfoil section with a chord length of 2.3 inches and the span of 14 inches. The airfoils were made of aluminum using the surface co-ordinate Equation-2.1 obtained from Abbott and Von Doenhof [59].

$$y_t = \pm \frac{t}{0.2}(0.2969\sqrt{x} - 0.1260x - 0.3516\,x^2 + 0.2843\,x^3 - 0.1050\,x^4) \qquad (2.1)$$

where‘t’ is the thickness and ‘x’ and ‘y’ is the horizontal and vertical coordinates respectively.

A Low-Aspect-Ratio-Oscillating-Flap (LAROF) near the outboard trailing edge of one of the two model wings had a chord length of 0.57 inches and a span of 0.5 inches. The wings were mounted vertically in the test section such that part of the wingspan was above the free surface of

the water. They were attached to semicircular pin joint fixtures that allowed for variation in the angle of attack with a resolution of $\pm 2^{\circ}$. The pin joint fixture was in turn connected via screws to a sliding mount which allowed for adjustment of effective length of the wings in water. This sub-assembly was connected to the rectangular breadboard which had roller bearing for moving on the rails. The entire assembly was painted to prevent the chemical reaction of aluminum with water.

The LAROF was set in motion with the help of a shaft which was embedded inside one of the two wings via a brush motor. The motor used was a Limited-Angle-Torque- Motor from H2W technologies, with continuous torque of 3.5 N-cm and $\pm 60^{\circ}$ maximum angle variation. The details of the motor are given in the Appendix section-A. To accurately measure the angular displacement of the LAROF, the motor was also equipped with an incremental encoder. A LabVIEW code was written to get the instantaneous angular position of the shaft with respect to time. The main criterion was to achieve equal displacement of LAROF on both sides of the trailing edge. To achieve this, an amplitude constraint system (Figure-2.2) was installed to keep the drive shaft centered prior to being embedded in the wing. This system consisted of four springs that were connected to a rectangular piece of aluminum. The global coordinate system was defined such that the x –axis is along the streamwise direction, y axis is along the spanwise and z axis is along the transverse direction.

The LAROF was displaced in a sinusoidal manner with the help of a National Instrument DAQ card (PCI -6035 e) and LabVIEW software. The motor input was a high voltage, low current signal which was amplified by a constant current amplifier. Data acquisition was done by using LabVIEW 8.2 software. The amplifier was powered by 16 VDC from a power supply. The

brushless amplifier (ZB12A8C), connected to the motor is a constant current amplifier which has a current scaling of 1.2 A/V purchased from advanced motion controls (Figure-2.3). A detailed wiring of amplifier with motor is presented in Appendix A. The relative angular position of the shaft was acquired by National Instrument DAQ card (NI USB-6210) with the help of a code written in LabVIEW software.

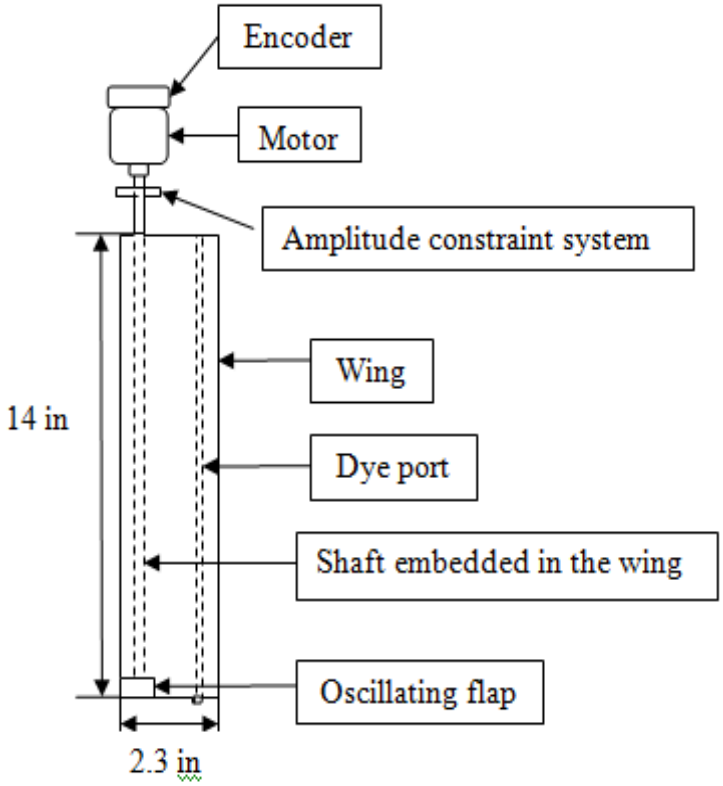

Figure-2.2: Details of the wing with motor and LAROF

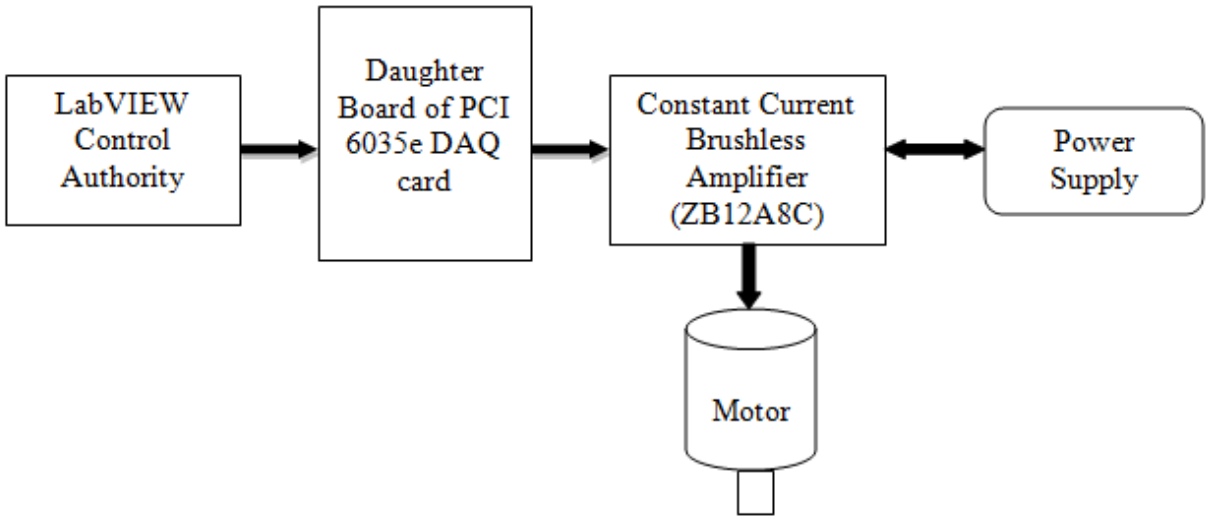

Figure-2.3: Electrical Setup

2.4 Preliminary evaluation:

The initial tests were conducted for SVS at a free-stream tunnel velocity of 0.3 m/s. The wing was held vertically in the test section at a fixed location. Both PIV and PLIF techniques were implemented at a fixed plane downstream of the wing. The detailed description of the experimental setup is discussed in the following sections. The CCWT has a honeycomb structure at the inlet section to make the flow uniform. Despite this it was discovered that there was significant flow non-uniformity in the relevant cross-planes. In addition, a vortex system caused by the pump operation was detected. This vortex system, thereafter referred to as the Tunnel Vortex, had strength which was of the same order of magnitude as the wing-tip vortex. Figure-2.4 shows the tunnel vortex which was captured during PIV experiment with the CCWT in operation without any wing in test-section. In the CCWT, the direction of tunnel vortex was seen to be counter clockwise in the field of view. With the CCWT in operation, the tip vortex was wandering because of interaction with the Tunnel Vortex. Figure-2.5 shows the velocity field in the cross plane obtained at x/c = 3. The velocity field of the vortex is not uniform around the core

of the vortex. Theoretically, the velocity field around the vortex core is expected to be azimuthally uniform. In the radial direction it is expected to have a velocity distribution similar to a Rankine vortex. In other words, moving outwards from the center of the vortex, the tangential velocity should increase steadily till the radius of the core and decrease exponentially thereafter. As seen in the Figure, the experimental data have shown a velocity distribution which is non-uniform azimuthally and radically, in contrast to the theoretical model. In addition, the unexpected region of high velocity seen below the tip vortex is probably due to the interaction effects of wing-tip vortex and the tunnel vortex.

One of the methods to negate the effect of tunnel vortex was to use a honeycomb mesh at the inlet of the test section. However, there were difficulties in installing the mesh. Even after installation, the resulting flow field downstream of the mesh was not uniform. Another method included strengthening the tip vortex to make it dominant compared to the tunnel vortex. This could be achieved either by increasing the free stream velocity of the tunnel or the AOA of the wing. To increase the free stream velocity, it was required to increase the CCWT pump RPM which in turn resulted in strengthening the tunnel vortex thereby negating the desired effect. Increasing the AOA led to separation effects on the wing, this was also not desirable.

As a result, these attempts to negate the tunnel vortex were unsuccessful. The CCWT concept proved to be unsuitable for the study of tip vortices. It was therefore decided to modify the CCWT into a towing tank facility.

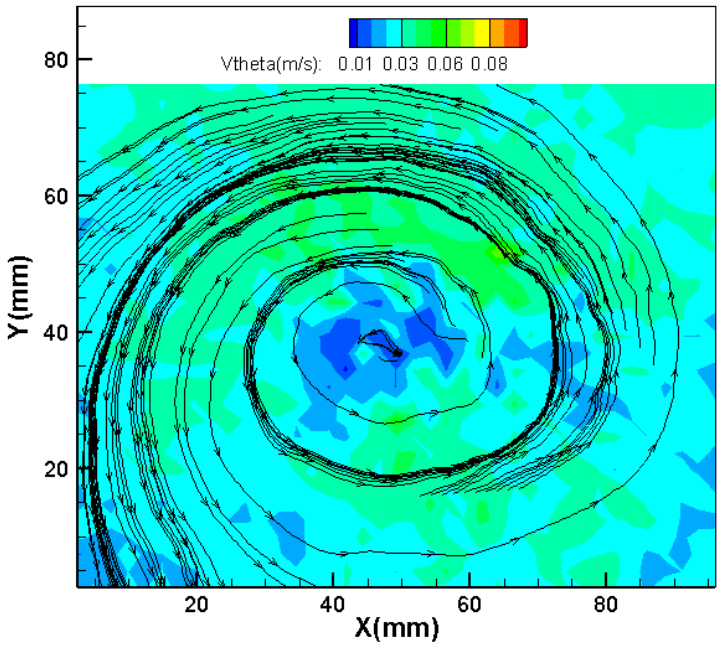

Figure-2.4: Tunnel Vortex captured in CCWT using PIV

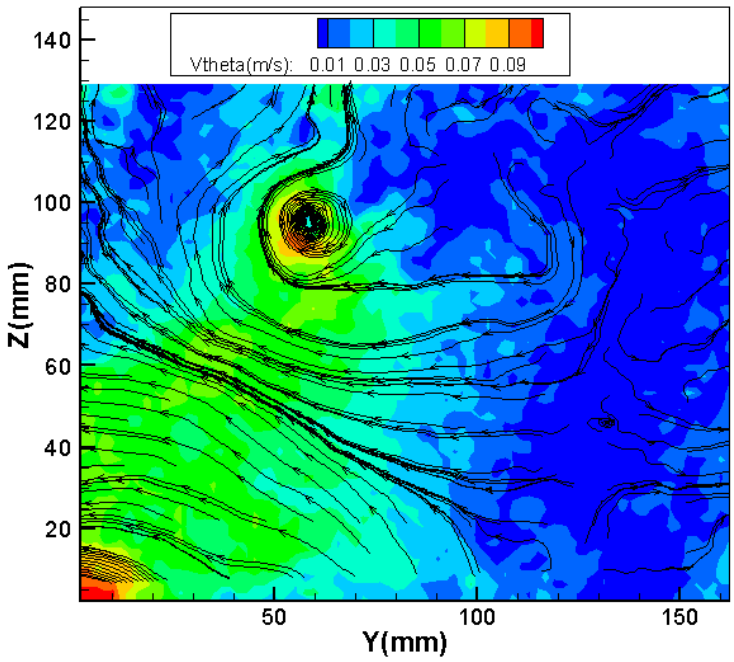

Figure-2.5: Wing tip vortex captured in CCWT using PIV

2.5 Details of the Tow Tank:

The advantages of using towing tank compared to wind tunnel or water tunnel for this effort were the absence of the tunnel vortex and the lower power to tow the model through stationary fluid as compared to CCWT [60]. Additionally, since the water in the towing tank was stationary, formation of boundary layer on the walls of the test section and subsequent reduction in the test-section cross-sectional area was eliminated.

Models were towed through the tank using a motorized carriage mounted on the rails with a speed variable from 5 cm/s to 45 cm/s with accuracy of 1%. The motorized carriage consisted of a breadboard for mounting the models and motor-spool. The motor spool was aligned with the carriage to prevent unbalanced forces. Before the start of operation, sufficient tension in the rope was ensured to avoid slacking.

A sample result is presented in Figure-2.6 which was captured using towing tank and PIV. On comparing it with previous results obtained via CCWT, it can be seen that the vortex obtained through towing tank setup is much cleaner. The vortex captured via towing tank closely resembled the theoretical vortex model. Given the higher fidelity of results, it was decided to proceed with the towing tank setup for all experiments.

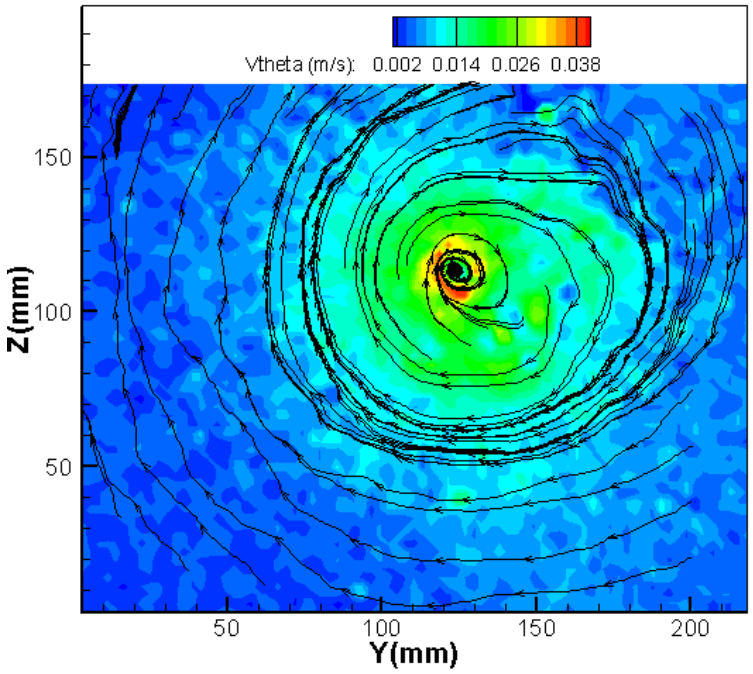

Figure-2.6: Wing tip vortex captured in towing tank

For the wing to attain a steady velocity before it reached the measurement plane, it was towed 23 times and the standard deviation in the speed of the wing was determined .Two fixed points were marked on the test-section of the towing tank. The time taken for the wing to travel the distance between the fixed points was measured and using this data, the speed of the wing was determined. The standard deviation in the wing velocity was 2.8%.

A uniform velocity of the wing all along the length of the test-section was required. To achieve this, a paper measurement tape was stuck all along the side of the test-section. The time taken for the wing to move every two inches was measured and from that the wing velocity was calculated. The Figure-2.7 shows that the velocity remained nearly constant over a distance of 20 inches. Since the measurement plane was almost in between this distance, it was evident that the wing had attained a steady velocity before data was collected.

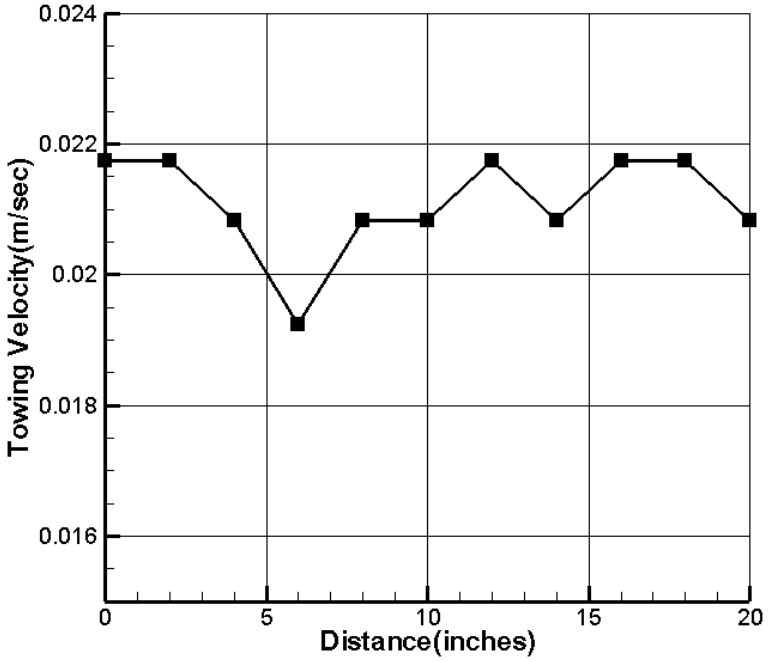

Figure-2.7 Towing velocity variation with distance

2.6 Measurement Techniques:

2.6.1 Particle Image Velocimetry (PIV):

Particle image velocimetry is a non- intrusive, optical fluid measurements technique used for quantifying the velocity of particles in a seeded flow field. The flow field is seeded with the tracer particles and illuminated by double pulse laser sheet. The camera is synchronized with the help of PIV processor to capture the image of the flow field at every pulse. Therefore, an image pair is obtained of which velocity field can be obtained by applying numerous correlation and algorithm techniques.

The PIV system used for current research consisted of a Dantec Dynamics Flow Map PIV system, a New-Wave Solo 200 mJ dual pulse Nd: YAG laser, a Dantec Dynamics High sense 1k x 1k cross-correlation CCD camera and a PIV-2100 processor. The collected images were

processed using PIVPROC software. The lens used to capture the images was 35mm f/2.8 D Nikkor AF. The seeding particles were silver coated hollow glass sphere with a mean diameter of 20 μm. The time between pulses was chosen such that the particle displacement was around 2-3 pixels between the successive images. The images was then cross correlated with sub region distortion using interrogation region of 32 px x 32 px with 50 % overlap with a number of refinement step equal to two. The thickness of the laser sheet was chosen to be 2-3 mm. The experimental setup for PIV is shown in the figures -2.8 (a) and (b).

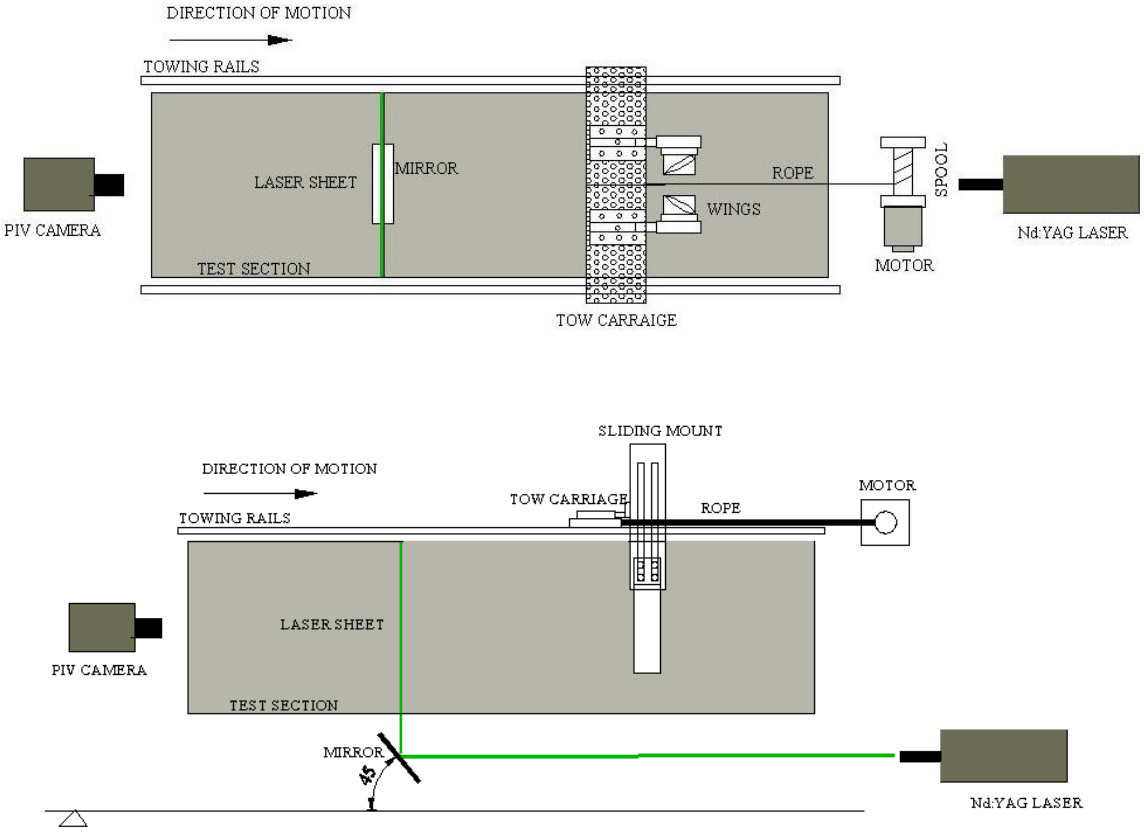

Figure-2.8 PIV experimental setup, (a) Top view, (b) Side view

Field of view is required to measure the particle displacement in the images to covert the pixel coordinates to the physical coordinates. This is done by placing the PIV calibration target

in the flow field which is square in cross-section with black spots on the white background with a fixed spacing of 5 mm between successive spots. With the help of the calibration target, the value of pixels per inch can be calculated in the physical space. The Field of view for the current setup was chosen as large as possible to capture the vortex structure for a longer period of time.

PIV was used to get the quantitative measurements of the flow field. Using the 2D cross-sectional view of the system, parameters such as velocity (V), circulation (Γ), radius of the core (a) and vorticity were evaluated. For the case of CRVS, the spacing between the vortices was also evaluated with time. Also, kinetic energy was calculated.

2.6.2 Planar Laser Induced Fluorescence (PLIF)

Fluorescence dye illuminated by a laser light sheet from Argon ion laser of 514.5 nm wavelength was used to visualize the flow in the plane of interest. The laser sheet was made parallel to the cross plane with the help of cylindrical lens and a mirror mounted at 45° with reference to the horizontal. The flow patterns were either recorded as standard video using a Cohu CCD camera and a JVC BR-S622DXU professional video recorder/player. A tube embedded into the wing at quarter chord location supplied dye for the flow visualization. A gravity feed pump was set for smooth outlet of dye through the dye ports. The experimental setup for flow visualization is same as that of the PIV setup with Nd: YAG laser being replaced with Argon-ion laser and the PIV camera being replaced with the video camera.

PLIF was used to qualitatively describe the initial structure of the vortices. It was also used to find out the wavelength of the instabilities that begin to appear in initially straight and parallel vortices.

2.6.3 Hot film Anemometry:

The power spectral density (PSD) in the wake of wings was measured with the help of hot film anemometry. The general setup is shown in Figure 2.9 (a) and (b) and consists of a TSI Inc. IFA-300 CTA systems, a National Instrument data acquisition board (NI USB-6210) and a TSI Inc 1260A-20W hot-film probe. The probe was mounted on a custom built mounting bracket and was located in a fixed plane. The positional coordinate of the probe was 0.5 in from the tip of the wing in the horizontal direction and 1 in above the tip of the wing in the vertical direction. A total of 8000 to 22,000 samples were recorded at a sampling rate of 200Hz for each measurement. The data was later analyzed in MATLAB. The experimental setup for Hot –Film Anemometry is shown in the figures below. Hot film anemometry was also used to monitor the decay of the perturbations at a fixed point in the flow field.

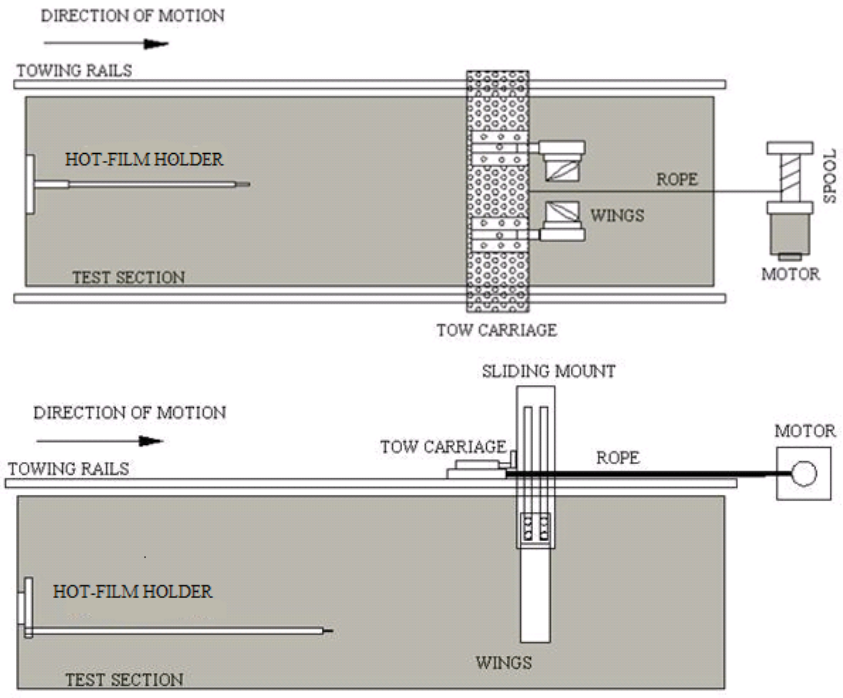

Figure-2.9: Hot-Film Anemometry setup, (a) Top view, (b) Side view

2.7 Test variables:

The following testing parameters were chosen for conducting experiments.

2.7.1 Tow speed and AOA:

Previous studies [61] have shown that experiments had to be conducted at low possible AOA and high speed to avoid separation effects. Choosing low AOA (1°- 3°) would have produced weaker vortices and high AOA (8°-12°) would have caused separation over the wing so, selecting the value of AOA in the range of 3°-6° was deemed optimum for the present effort. Additionally, it has been noted that testing at low AOA i.e. 3°-6° would prevent separated boundary layers from interfering with the wake [61]. To prevent turbulence at high speeds, a towing speed range of 0.24-0.45 m/s was chosen.

2.7.2 Spacing between the wings:

Since the instabilities in the wake develop after the vortices have come closer [62], it was required to have a long tunnel to clearly observe the formation of instability. Due to the relatively short length of the towing tank, minimum possible spacing was chosen. The exact number chosen for wing spacing are discussed later.

2.7.3 Location of measurement:

When the towed model is set in motion and stopped, it leads to the generation of starting and stopping vortices [60]. Therefore, it was ensured that the plane of measurement was midway between the starting and the stopping location. Also the data was collected for a relatively short

period of time and the data collection was stopped as soon as the stopping vortex reached the plane of measurement. This was achieved by trial and error.

2.7.4 Frequency and amplitude of oscillation

In order to perturb the vortex, it was required to oscillate the LAROF with low amplitude and at high frequency. It was decided to set constant amplitude for all frequencies by changing the input voltage for each case. The tests were carried out at two Reynolds numbers (14,000 & 25,000). The AOA of the wings was set to 5° for both the SVS and CRVS. The spacing between the wings for two vortex case was 4.4 inches.

Table-2.1: Reduced frequencies coefficients for different forcing frequencies

Oscillation Amplitude	Re = 14,000		Re = 25,000	
	Excitation Freq. (Hz)	Reduced Freq.	Excitation Frequency (Hz)	Reduced Freq.
0.12 cm	5	0.025	5	0.014
	10	0.051	10	0.028
	15	0.076	15	0.043
	20	0.10	20	0.057
	25	0.13	25	0.071
0.24 cm	10	0.10	10	0.057
	15	0.15	15	0.085
	20	0.20	20	0.11
	25	0.25	25	0.14
	30	0.31	30	0.17

2.8 Image Processing

The acquired images from PIV camera required various enhancements and modifications in order to correctly distinguish the vortex structure. With the help of MATLAB, the corrections due to system imperfections and various image enhancements techniques were employed to improve the quality of the images. In this section few samples images are presented before and after the modification to the raw data to clearly see the effect of all enhancement procedures.

Even though complete darkness was required in the room at the time of the experiment, the initial images captured by the PIV camera had few traces of ambient light. This introduced noise in the experiments that had to be accounted. Since PIV algorithms track a particle's displacement between an image pair to determine its velocity, a good contrast was required between the PIV particles and the background darkness. A contrast enhancement technique was applied in MATLAB using the function called *imadjust*. Figure-2.10 shows the image before (left) and after (right) applying contrast enhancement technique. This function maps the intensity values in a grayscale image to new values such that 1% of the data is saturated at low and high intensities of the original gray scale image. PIV algorithms were later applied on the enhanced images to yield to fluid dynamic parameters of the flow field.

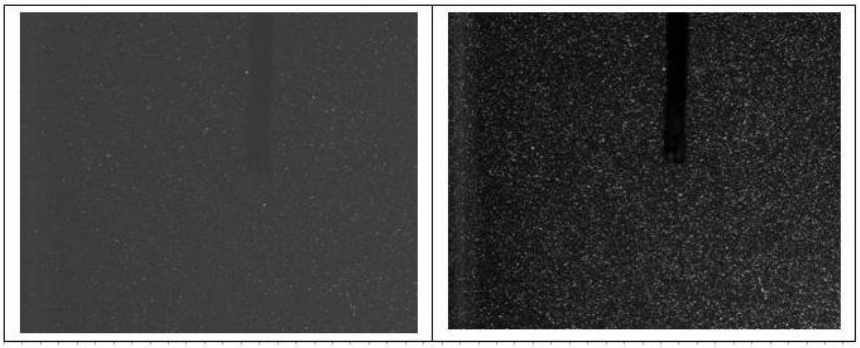

Figure-2.10 Effect of contrast enhancement

2.8.1 Image Re-sampling:

To capture the intricate details of the vortex core, it was required to have a resolved grid. A custom algorithm using 2D-bilinear interpolation scheme was applied on the original non resolved grid to convert into a resolved grid. This algorithm considered an original cell consisting of four grid nodes and interpolated values inside this cell area to get the refined solution. This resulted in the transformation of the original coarse grid (38 x37 grid points) to finer (300 x 300 grid points) as shown in Figure-2.11(a) and (b).

The vortex core, being a relatively small area compared to the net vortex structure, was difficult to capture. Image re-sampling allowed the low velocity region of the vortex core to be captured. Figure-2.12 shows a comparison example. The resulting image after bilinear interpolation was found to be much smoother.

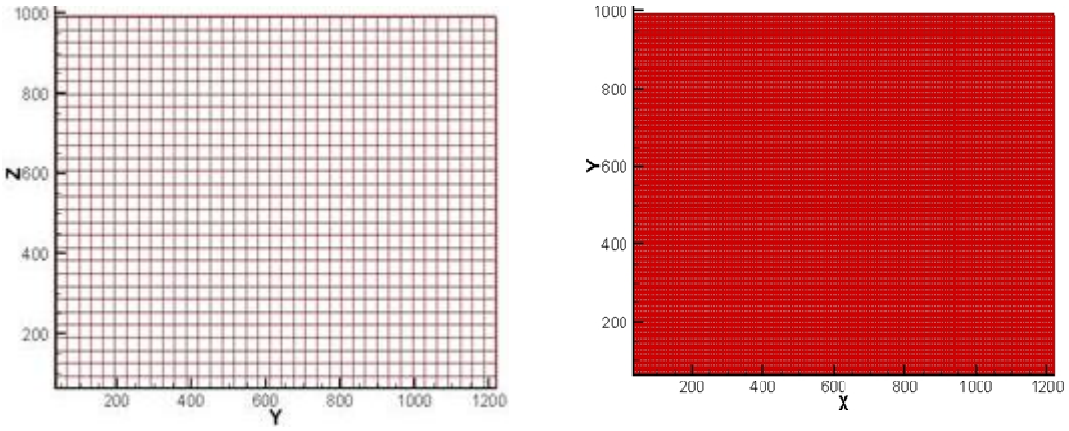

(a) **(b)**

Figure-2.11 Re-sampling, (a) Before, (b) After

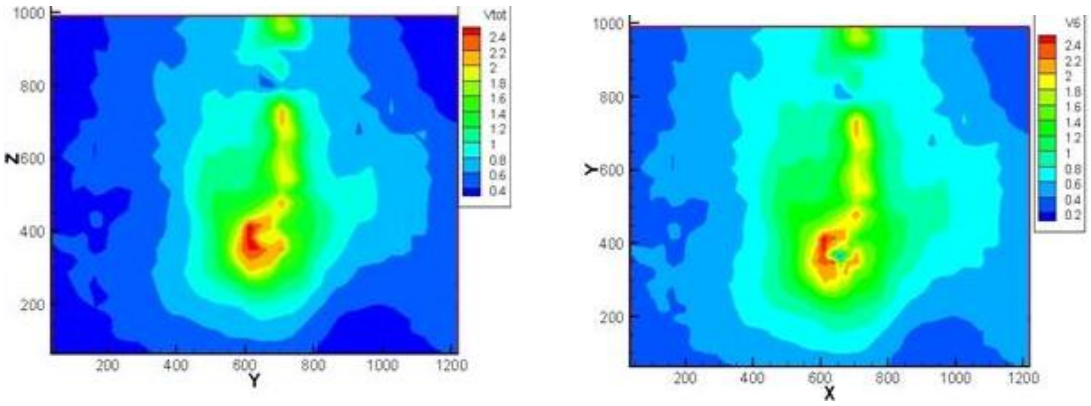

(a) **(b)**

Figure-2.12: Effects of re-sampling on 2D velocity field, (a) Before, (b) After

2.8.2 Image Stitching:

As the vortices descended under mutual induction and meandered under the influence of free stream turbulence, it was required to have a large field of view. Initially a single PIV camera (lens focal length = 35 mm) was used to capture the entire field of view but resulted in poor spatial resolution and solution fidelity. Since it was required to have a fixed field of view, it was decided to use to two cameras to capture the same field of view. This resulted in higher spatial resolution without a compromising on field of view dimensions.

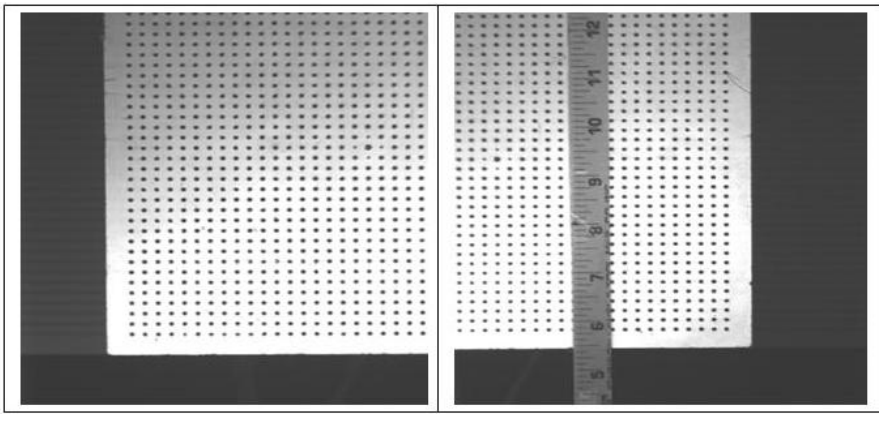

(a) **(b)**

Figure-2.13 Sample images of PIV calibration target captured by cameras, (a) Left, (b) Right

These two images were then merged to form a single coherent image of the field of view using MATLAB. This process was conducted in numerous steps. In the first step, images of the PIV calibration target from both cameras with a predefined field of view overlap were obtained (Figure-2.13(a) and (b)). In the next step, they were rotated and merged to form a single coherent image with effective field of view being the summation of two individual field of view's minus the overlap region.

Before the final merging process, PIV algorithm was applied individually on the images from both the cameras to get the initial 2D velocity field (Figure-2.14 (a) and (b)). Stitching process as mentioned above was applied to the 2D velocity field vectors to get the single coherent image (Figure-2.14(c)).

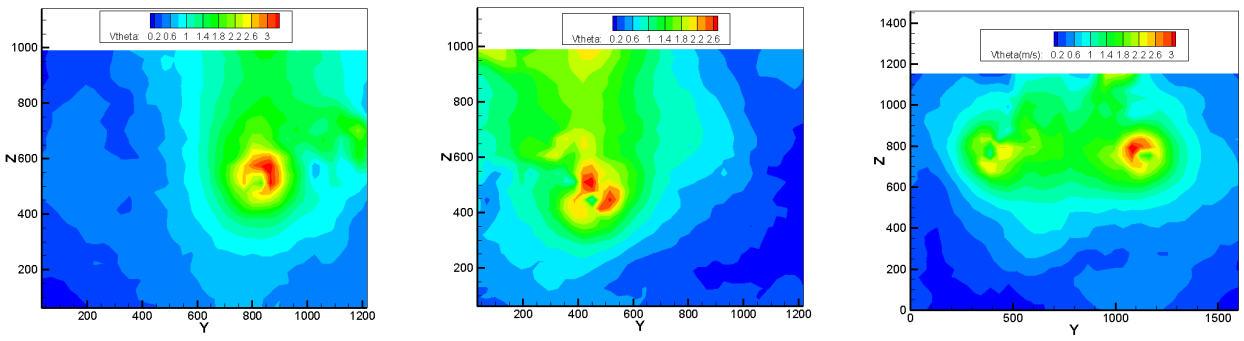

(a) **(b)** **(c)**

Figure-2.14: 2D velocity fields generated after applying PIV algorithm on individual images, (a) Left camera, (b) Right camera, (c) Final Stitched image

3. Flow Visualization and PIV Results

3.1 Results for Single Vortex System (SVS):

3.1.1 Overview:

SVS system was studied for the following reasons: 1) it was important to verify the possibility of obtaining a clean vortex with negligible interference from walls and 2) it was desired to establish a baseline for the vortex motion in the absence of mutual induction by other vortex filaments in the surroundings. The strength of the vortex was evaluated at different AOA settings and for various forcing frequencies and amplitudes using a MATLAB code. The vortex data was compared with theoretical and semi empirical models available in the literature. The data was recorded for 40 sec. Since vortex downwash is proportional to the airfoil speed and AOA, longer data sets were obtained at low speed and AOA. At higher speeds and AOA vortices travelled out of the field of view more quickly and interacted with the side walls or free surface of the towing tank, thus limiting the amount of data. Depending on the no of images that captured a vortex in the field of view camera, different conditions resulted in data collected for different time.

3.1.2 Comparison with existing vortex models:

The existing vortex models are listed in Table 3.1. Some of the more prominent vortex models are Rankine vortex, Lamb-Oseen Vortex, Hallock and Burnhman model etc. The

Rankine vortex consists of a region which rotates like a solid body containing constant vorticity known as core region and an outer region with potential flow without vorticity. The Lamb-Oseen Model is the exact solution of the Navier-Stoke Equation for laminar flow. It blends the core region with the potential region of the Rankine vortex and decay roughly with 1/r. Proctor [66] curve fitted the LIDAR field measurement data to develop Adapted vortex model. Winckelmans et al [67] did an empirical fit to the wind tunnel data of a rectangular wing (no flaps, no fuselage). Hallock and Burnhman model [65] also has been adapted from field measurement data.

Figure-3.1 shows the velocity variation in the radial direction for various vortex models and experimental data. The radius of the core which is the input variable for various models was determined from experimental data. The value of Γ_O was calculated from the maximum average tangential velocity at the radius of the core. From the figure, it is clear that the Lamb-Oseen vortex model offers the best fit to the experimental data indicating for laminar flow field.

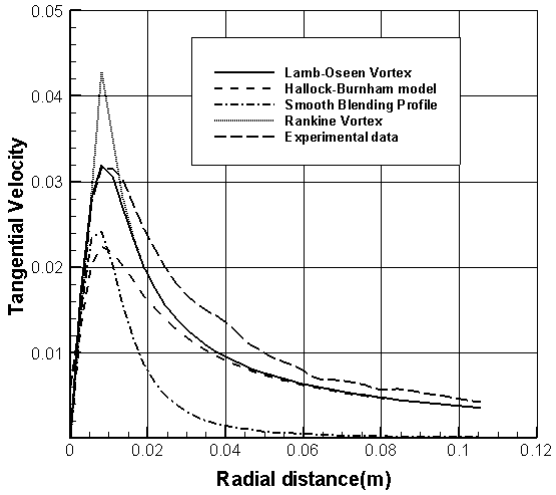

Figure-3.1 Comparison of vortex models and experimental data

Table 3.1: Theoretical Vortex models

Vortex Model	Governing Equation
Rankine model[63]	$v_\theta = \frac{\Gamma_O}{2\pi r_c}\frac{r}{r_c}$, for r $\leq r_c$ $v_\theta = \frac{\Gamma_O}{2\pi r}, for\ r > r_c$
Lamb-Oseen vortex[64]	$v_\theta(r) = \frac{\Gamma_o}{2\pi r}\left\{1 - \exp\left(-1.2526\left(\frac{r}{r_c}\right)^2\right)\right\}$
Hallock –Burnham Vortex[65]	$v_\theta(r) = \frac{\Gamma_o}{2\pi r}\frac{r^2}{r^2 + {r_c}^2}$
Adapted Vortex(Proctor)[66]	$v_\theta(r) = 1.4\frac{\Gamma_o}{2\pi r}\{1 - \exp(-10(r_c/b)^{0.75})\}$ x $\{1 - \exp(-1.2526(r/r_c)^2)\}$ for , r≤r_c, $v_\theta(r) = \frac{\Gamma_o}{2\pi r}\{1 - \exp(-10(r/b)^{0.75})\}$, for r > r_c
Smooth Blending Vortex Profile[67]	$v_\theta(r) = \frac{\Gamma_o}{2\pi r}\left\{1 - \exp\left(-\frac{\beta_i(r/b)^2}{\{1 + [(\beta_i/\beta_o)(r/b)^{5/4}]^p\}^{1/p}}\right)\right\}$, With $\beta_o, \beta_i, and\ p$ = 10,500, and 3, $respectively$

3.1.3 Data Analysis:

Standard PIV data provided only two components of the three dimensional vector fields. In order to characterize the trailing vortex wake of the rectangular airfoil, several quantities were evaluated from this vector data. The data collection was initiated when the wing traverses the laser plane (time of initiation of vortex) and continued until the vortex left the FOV of the camera.

Since the tip vortex was the dominant structure in the cross plane of the flow field, the velocity in that plane was considered as resultant velocity. This resultant velocity was defined by Equation 3.1 and calculated from the velocity vector data [63]. It was non-dimensionalised by towing velocity the wing (U_∞).

$$\vec{v} = \sqrt{{v_\theta}^2 + {v_r}^2} \tag{3.1}$$

The axial vorticity field is defined as the difference in gradients of velocities. It was calculated using the general Equation-3.2.

$$\vec{\omega} = \left(\frac{dw}{dy} - \frac{dv}{dz}\right)\hat{\imath} + \left(\frac{du}{dz} - \frac{dw}{dx}\right)\hat{\jmath} + \left(\frac{dv}{dx} - \frac{du}{dy}\right)\hat{k} \tag{3.2}$$

Since the PIV measurements captured the velocities in cross plane, the net axial vorticity is in the y-z plane given by Equation-3.3. The vorticity was non-dimensionalised by multiplying with chord length and dividing by wing velocity.

$$\omega_x = \left(\frac{dw}{dy} - \frac{dv}{dz}\right) \tag{3.3}$$

To determine the displacement of the vortex due to meander and forcing, it was required to calculate the location of the vortex core. Since the vorticity at the center of the vortex was

highest and it decreases thereafter in the outfield, the centroid of the vortex was determined by locating the point of maximum vorticity in the flow field. The vortex core radius was non-dimensionalised by the chord length of the wing.

After determining the location of the vortex core, its radius and maximum velocity were calculated .The radius of the vortex core is defined as the location of maximum tangential velocity in the vortex. Due to experimental errors, the vortex obtained was not completely uniform with respect to distribution of the velocity field. Therefore, it was decided to determine the maximum velocity by taking an average in four azimuthally locations. Maximum velocity at each point was determined separately by traversing along the fixed grid points.

Circulation (Γ), is one of the important parameter that defines the characteristics of a vortex. It also expresses the amount of vortex hazard [63] and is defined as:

$$\Gamma = \oint v_\theta \, ds = \oiint \omega_x . \, \mathrm{dy.dz} \tag{3.4}$$

For single and axi-symmetric vortex, the circulation was obtained from v_θ by [63]

$$\Gamma(r) = 2\pi r v_\theta(r) \tag{3.5}$$

There are two methods of calculating circulation based on tangential velocity or vorticity equations. Since the vortex was not spatially locked in the fixed FOV of the camera, there were instances when the vortex partly moved out of the FOV. In those cases circulation was calculated using maximum velocity and radius of the core.

The two-dimensional KE of the wake per unit mass is described as [68]

$$\mathrm{K.E} = \frac{1}{2} \int |V|^2 \, dA \tag{3.6}$$

When vortices are aligned parallel to the x-axis before the instability amplifies, the velocity field is nearly planar; hence equation above represents the true KE. An abrupt change in the KE is an indicator of two-dimensional flow converting into three dimensional flows. This equation does not represent the true KE of vortex for current calculations as substantial KE lies away from the vortex center. It only represents the summation of the Kinetic energy as captured in the FOV of camera. A MATLAB code is listed in the Appendix section G.

3.1.4 General Characteristics of SVS:

The PIV measurements for SVS indicate the steady nature of the vortex. Changing the wing speed or AOA shifts the measured value of various vortex parameters to a new value but the general trends remained unchanged. The contour plot of the velocity field is shown in the Figure-3.2(a). It clearly shows the low velocity region inside the core of the vortex, with velocity increasing in the radial direction to a maximum value and then decreasing thereafter. The vorticity field obtained by calculating the gradients of this velocity field is shown in the Figure-3.2(b). It shows the region of concentrated vorticity at the center with radial variation.

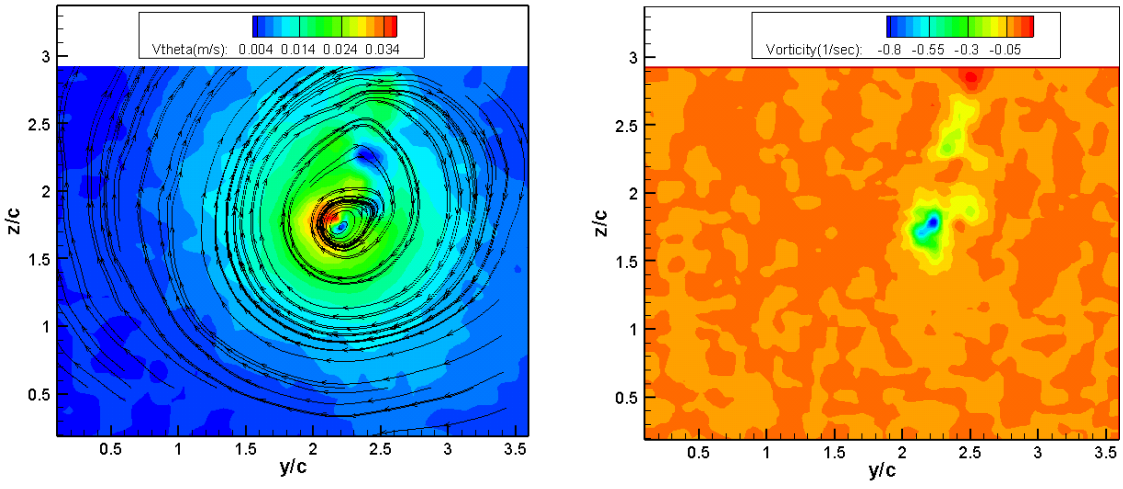

(a) **(b)**

Figure 3.2: Velocity and vorticity for no forcing case ($Re_c = 14,000$)

The sign of the vorticity depends on the direction of rotation of the vortex. In the case of SVS, the wing was set at negative AOA, resulting in a clockwise rotation hence negative vorticity. The variation of circulation for different AOA at a given speed was calculated (Figure-3.3). As seen in the figure, the trend was similar to analytical models.

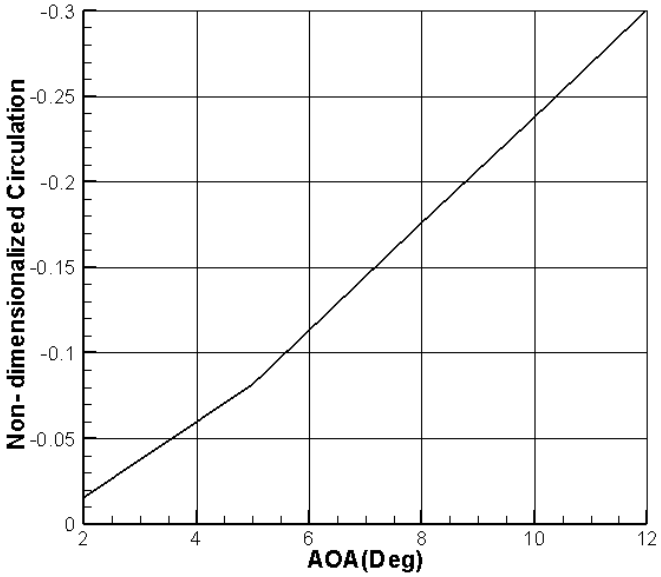

Figure-3.3 Variation of Circulation with AOA ($U_\infty = 0.3\ m/s$)

3.1.5 Effect of perturbations on the structure of SVS:

To clearly understand the effect of perturbation on the structure of the vortex core, it was considered necessary to compare the instantaneous streamline plots of the flow field of SVS for various forcing cases. Figure-3.4 shows the streamline contour for no-forcing case at different t* value. At t* = 0, the structure of the vortex core was slightly elliptical in shape (Figure-3.4 (a)). This was due to incomplete rollup of the vortex at that instant of time. At other instances of time (after t* =0), the vortex was completely circular in shape. The vortex remained coherent and decayed only by viscous diffusion (Figure-3.4(f)). In the Figure-3.4 (c), the vortex was seen to move to the right and top of the FOV. This behavior was theoretically sound.

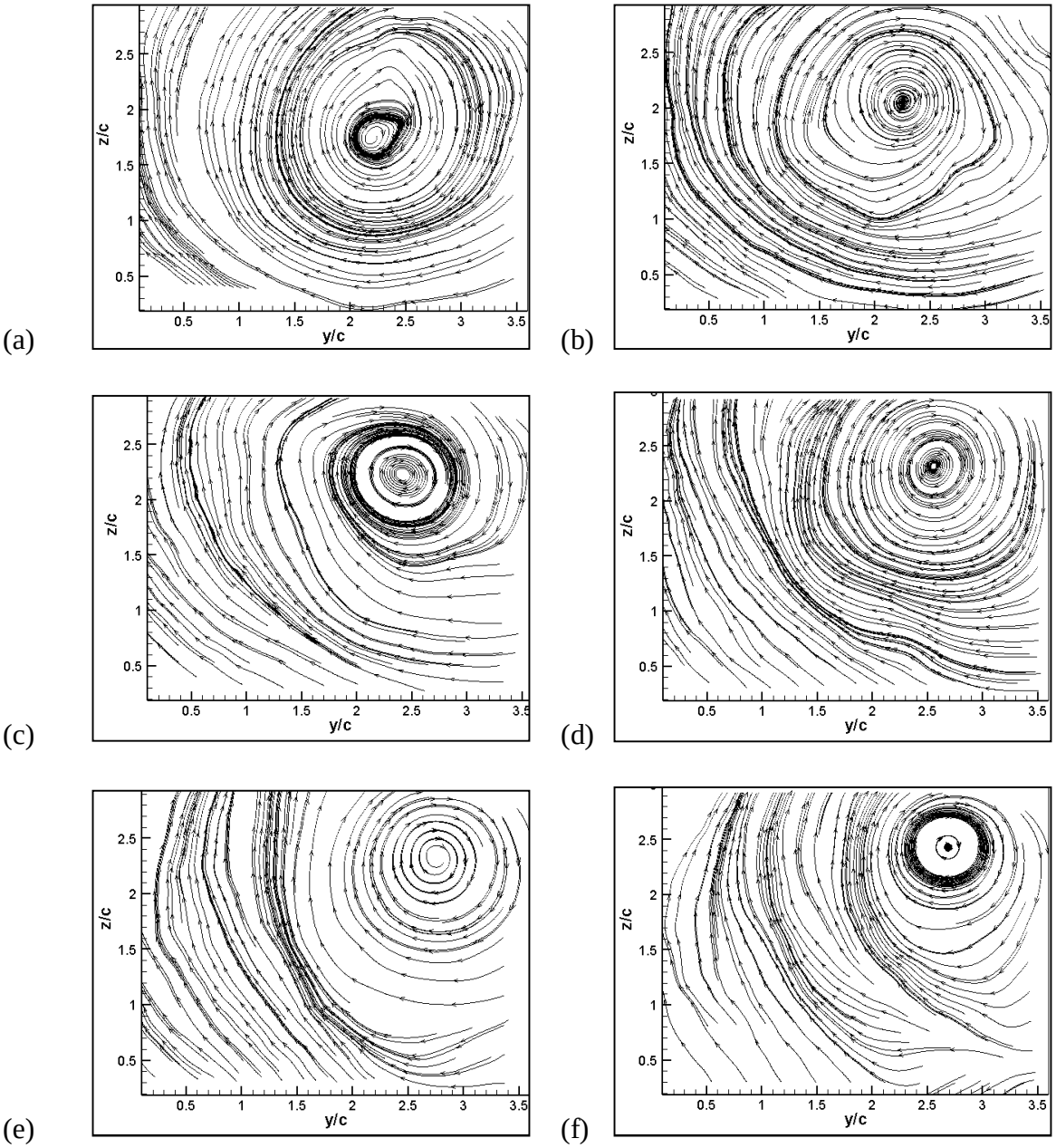

Figure-3.4 Streamline contours of SVS for no-forcing case and $Re_c = 14,000, A = 0.12\ cm$ a) t* = 0, b) t* = 16.4, c)t* = 41 ,d) t* = 74 ,e) t* = 107 and f) t* = 140

For 15Hz forcing frequency, the external perturbations resulted in slight modification of the structure of the vortex core at t*=0 (Figure-3.5(a)).The effect of perturbations seen as a deformation of streamlines around the core was observed at t*=16.4. After some time (t*=41), the vortex regained its coherent structure indicated by circular streamlines without any

deformation (Figure-3.5(c)). The vortex structure remained coherent for all later times (Figure-3.5(d-f)). It has been shown by Kelvin [69] that sinusoidal perturbation of the single vortex filaments do not grow in time, but rotate around the vortex. All results were in accordance with theoretical predictions and heuristic arguments.

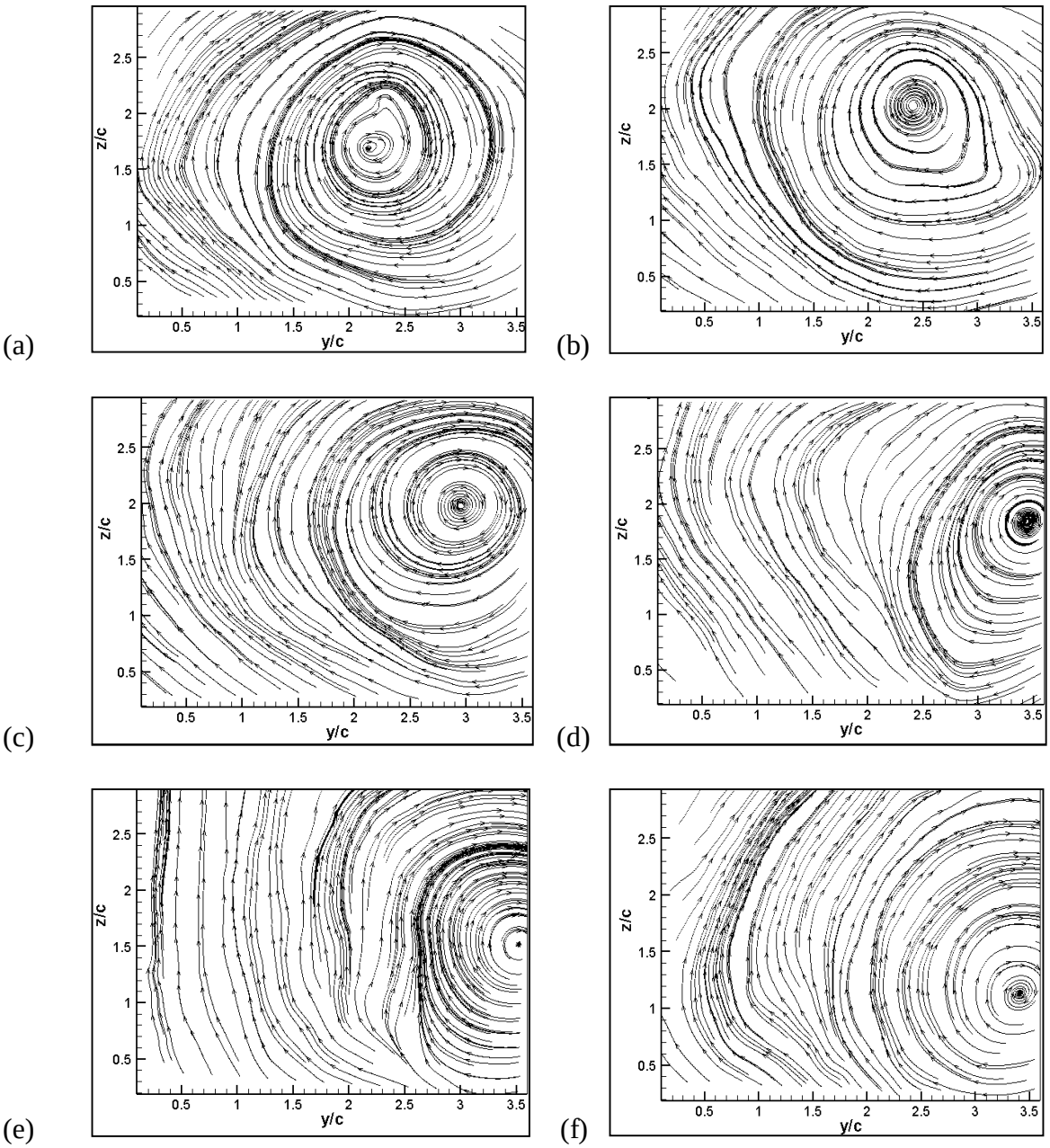

Figure-3.5 Streamline contours for SVS at 15Hz, $Re_c = 14,000, A = 0.12\ cm$ a) t* = 0, b) t* = 16.4, c)t*= 41, d) t* = 74, e) t* = 107 and f) t* = 140

3.1.6: Effect of forcing on various vortex parameters:

Next, the temporal variations in parameters of perturbed vortex are discussed for Re_c = 14,000 and A = 0.12 cm, 0.24 cm. As the vortex grew with time, it partly moved out the fixed FOV of the camera. Due to this, the data analysis was done until the vortex showed completely in FOV. The results presented therefore are based on data collected up to t^* = 60 after the wing traversed the measurement location. The maximum velocity of the vortex decreased with time as expected for all cases (Figure-3.6). In general with forcing, the maximum velocity was lower compared to the no-forcing case with the reduction being the maximum for the case of 15Hz (20% at t^* = 60). Similar trend was observed in value of minimum vorticity with the reduction being highest for 15Hz (38 % at t^* = 60) (Figure-3.7).

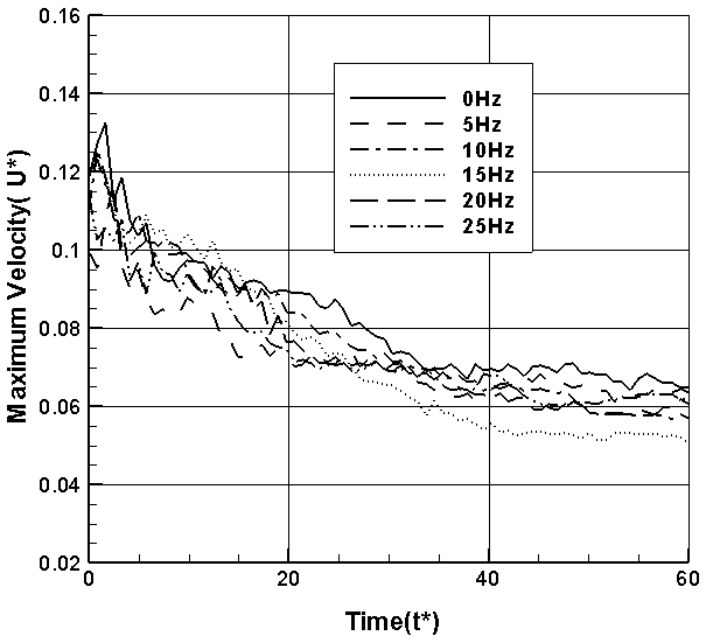

Figure-3.6: Variation of maximum velocity with time (Re_c = 14,000, A = 0.12 cm)

The vortex core radius increased with time because of viscous dissipation effects. In general with forcing, the radius increased compared to the no-forcing case with the maximum

increment being for the case of 15Hz (41 %) (Figure-3.8). In some cases, a sudden increase in a core radius was observed because of numerical error in the code. The circulation remained constant for standard as well as various forcing cases (Figure-3.9). The variation in circulation was found to be in error range i.e. ±0.1 of the mean value of circulation. The Kinetic energy of the vortex decreased when forced for all cases by variable magnitudes (Figure-3.10). The maximum reduction in KE was observed for the case of 15Hz and 25Hz (34 %). Table-3.2 shows the average values of various vortex parameters taken up to at t^* = 60 .By comparison, 15Hz forcing frequency showed maximum variation.

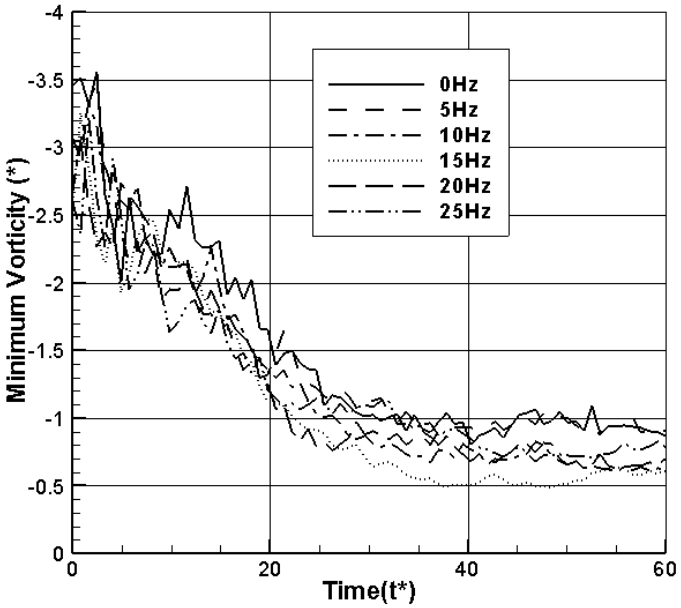

Figure-3.7: Variation of minimum vorticity with time (Re_c = 14,000, A= 0.12 cm)

For all cases i.e. forcing as well as no-forcing, the decay rates of various vortex parameters from t* = 0 to t* = 25 was high and thereafter, the decay rate decreased (Figure-3.6 to Figure-3.8). The region from t* = 0 to t* = 25 corresponds to the amount of time when the external perturbations introduced into the vortex were present in the flow field. This was indicated by varying values of parameters at same time for different forcing frequencies. The

vortex parameters remained unchanged or decayed slowly in the region from t* = 25 to t* = 60. External perturbations in the flow field dissipated after t* = 25 and therefore, the vortex dissipated only by viscous diffusion.

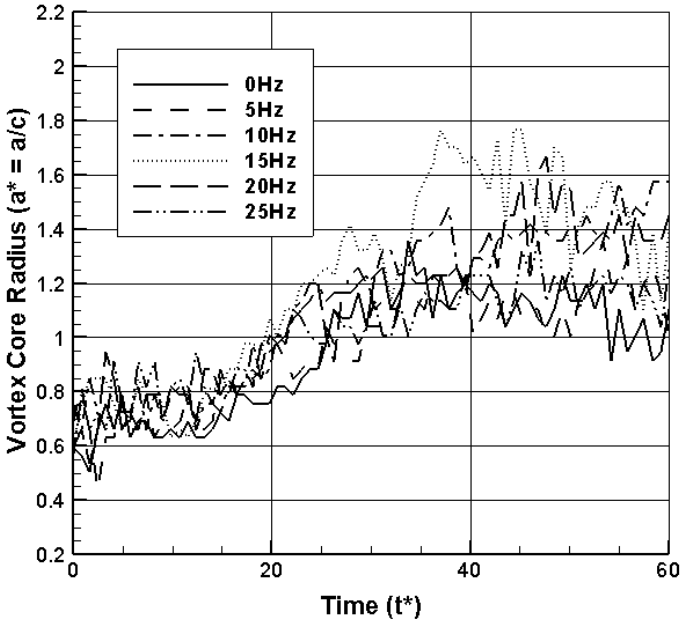

Figure-3.8: Variation of core radius with time (Re_c = 14,000, A = 0.12 cm)

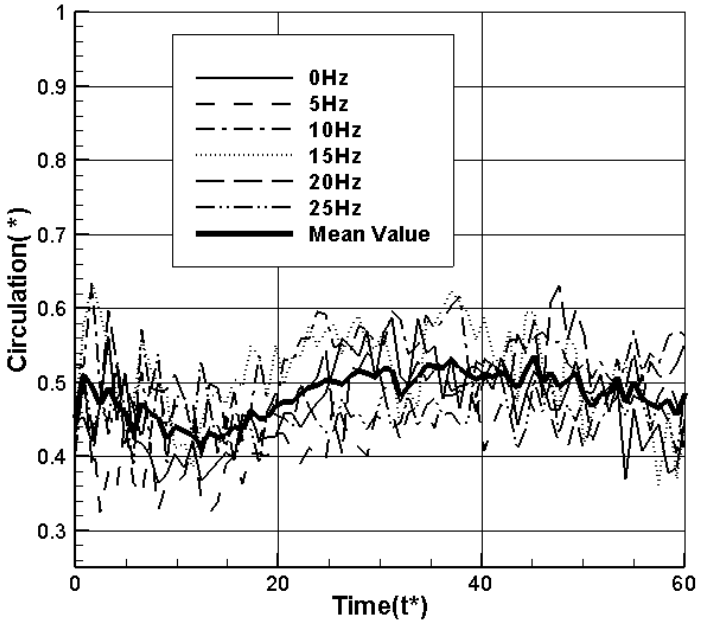

Figure-3.9: Temporal changes in circulation

(Re_c = 14,000, A = 0.12 cm)

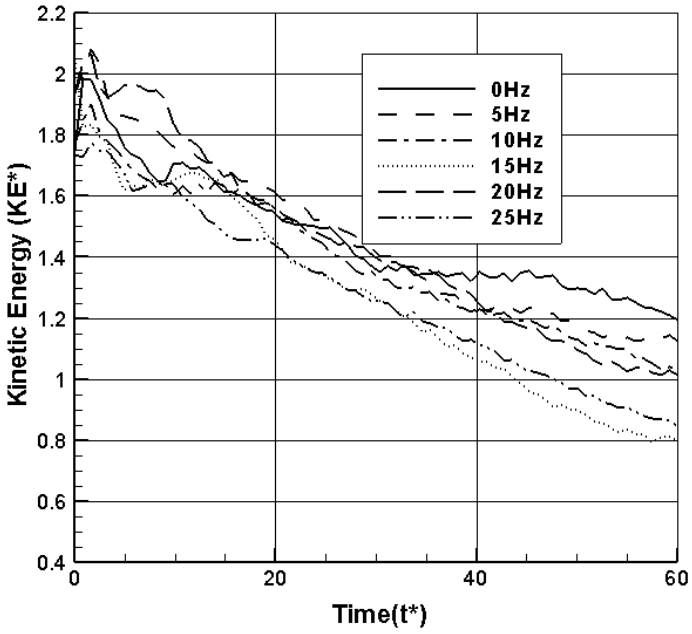

Figure-3.10: Kinetic energy variation with time ($Re_c = 14,000$, A = 0.12 cm)

Table-3.2: Average vortex parameters values for SVS

($Re_c = 14,000$, A= 0.12 cm)

	Single vortex system(SVS)				
Frequency(Hz)	Max Velocity $\left(\frac{V_\theta}{U_\infty}\right)$	Minimum Vorticity $\left(\frac{\omega c}{U_\infty}\right)$	Core Radius $\left(\frac{r}{c}\right)$	Circulation $\left(\frac{\Gamma}{U_\infty c}\right)$	Kinetic Energy $\left(\frac{KE}{{U_\infty}^2 A}\right)$
0	0.082	-1.483	0.951	0.468	1.463
5	0.073	-1.388	0.971	0.43	1.455
10	0.077	-1.272	1.152	0.526	1.377
15	**0.072**	**-1.114**	**1.223**	**0.515**	**1.26**
20	0.075	-1.227	1.122	0.502	1.433
25	0.074	-1.251	1.026	0.462	1.265

The trend in vortex parameters for the case of 0.24 cm oscillation amplitude is similar to the 0.12 cm oscillation amplitude for most cases. The results are presented in the Appendix-B. The maximum change in vortex parameters was observed for the case of 20Hz forcing

frequency. For vortex core radius, maximum change was observed for 15Hz which deviated from the trend observed for other vortex parameters. Overall, for the case of 0.24 cm amplitude, perturbations did not result in significant changes in vortex parameters. Hence low- oscillation-amplitude perturbations for the same conditions produced maximum change in vortex characteristics.

3.2 Results for Counter-Rotating Vortex System (CRVS):

3.2.1 Overview:

The setup was similar to the SVS with few variations. The two vortex generators (NACA 0012) were set at equal AOA with opposite rotation and distance between the tips of the wings was set to 4.4 inches. Two cameras were used side by side to capture the large FOV of the flow field. The details on the post processing of the images are given in chapter 2.

3.2.2 General Characteristics of CRVS:

Figure-3.11 shows the velocity (left) and the vorticity (right) field of the CRVS. Streamlines imposed on the velocity field shows two coherent vortices with low region of velocity at the center. The region between the vortices shows slightly higher value of velocity than the free-stream because of the superposition of velocities of both the vortices. The vorticity field showed two vortices at nearly same height with opposite direction of rotation as indicated by negative and positive value of vorticity. The vortices in the CRVS initially behaved as individual vortices without being affected by vicinity of each other.

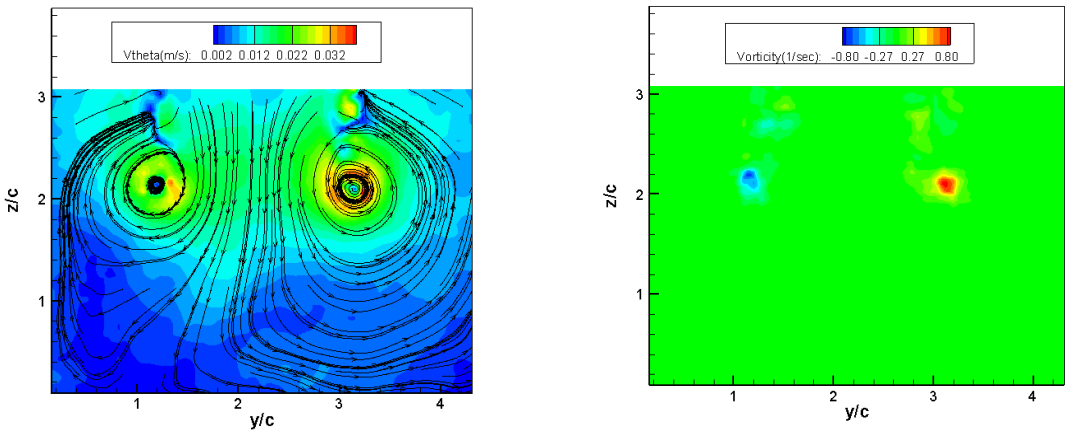

Figure- 3.11: Contour plot of velocity and vorticity of CRVS

Figure-3.12 shows the Lamb-Oseen vortex model fitted to the experimental data for both right and left vortices. In the figure, the left vortex is the one which is being perturbed. The left vortex showed a slight deviation from the theoretical model compared to the right vortex. This may be due the presence of LAROF at the trailing edge of the left wing. The deviation observed was not of significant magnitude; therefore the vortices were initially considered as Lamb-Oseen vortices without any interference effects. The radius of the vortex core measured from these figures was 0.0095 m, which was close to $0.098b_0$, found by Eliason et al [71].

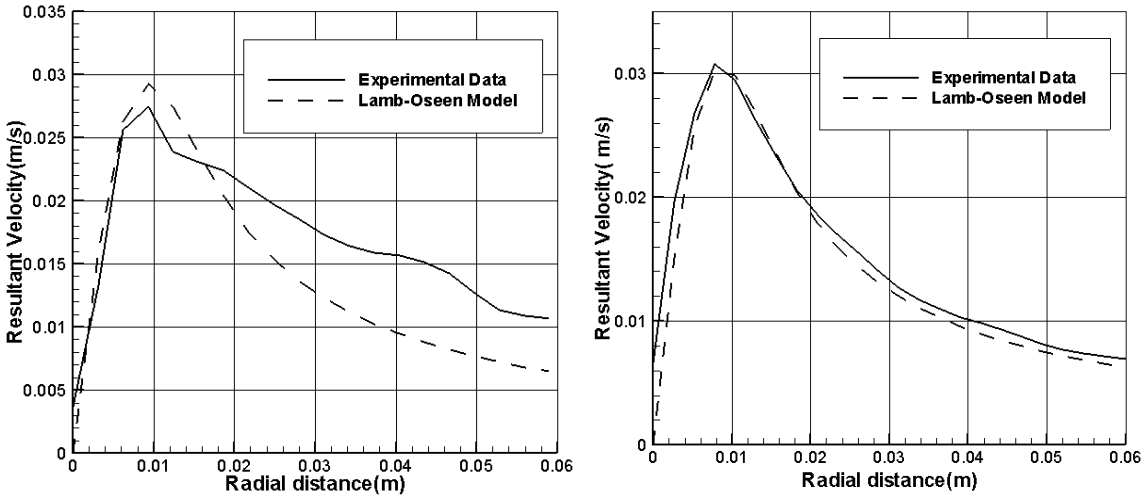

(a) **(b)**

Figure-3.12: A comparison of experimental data with Lamb-Oseen model, a) Left Vortex b) Right vortex

The PIV measurements for CRVS indicated the vortices descending under the effect of mutual induction. The temporal variations in vortex parameters are discussed for Reynolds number (Re_c = 14,000, 25,000) and oscillation amplitudes (A = 0.12 cm, 0.24 cm). Since the field of view of the camera was fixed and the vortices were descending with time, the number of images of the vortices captured in the fixed field of view was restricted. For comparison between different cases, maximum no of images were considered that showed vortices in the field of view. For higher Reynolds number, the number of images collected were even less because of higher descending rate of the vortices. The time was non-dimensionalised as $t^* = t\left(\frac{\Gamma}{2\pi\, b_0^2}\right)$, where Γ is the initial circulation of the one of the vortex.

3.2.3 Effect of forcing on the structure of CRVS:

The interaction characteristics of the CRVS when one of the vortices was perturbed were compared to the no-forcing case. Figure-3.13 shows the streamline plot of the instantaneous velocity field for the no-forcing case at t*= 0.17. A slight deformation of the left vortex was observed with the plane of vortices tilting by some angle to the vertical. This confirmed the initiation of Crow instability [44]. The existence of Crow instability for the no-forcing case was also confirmed by the dye visualization results (Figure-3.14 (a) and (b)). In these figures, the characteristics nature of Crow instability i.e. the sinusoidal displacement of vortices was clearly observed. A rough estimate of a wavelength of instability from these images was close to the theoretical predictions made by Crow [44]. The wavelength of instability was equal to $7.8b_0$, close to $8.6b_0$ predicted from theory. Similar tilting of plane of vortices was observed for 5Hz forcing frequency with vortices deforming to slightly elliptical shape from nearly circular (Figure-3.15 and Figure-3.16). The left vortex in the case of 15Hz forcing case was seen to

become stronger with the right vortex deforming into a dumb-bell shaped structure indicating splitting of a vortex (Figure-3.17).The 20Hz forcing case showed deformation of both the vortices into a nearly elliptical shape (Figure-3.18). The high frequency oscillation i.e. 25Hz seemed to have forced both vortices to move to the left of the FOV. This resulted in the left vortex partially moving out of the FOV (Figure-3.19). Therefore, 25Hz forcing case was discarded from further analysis.

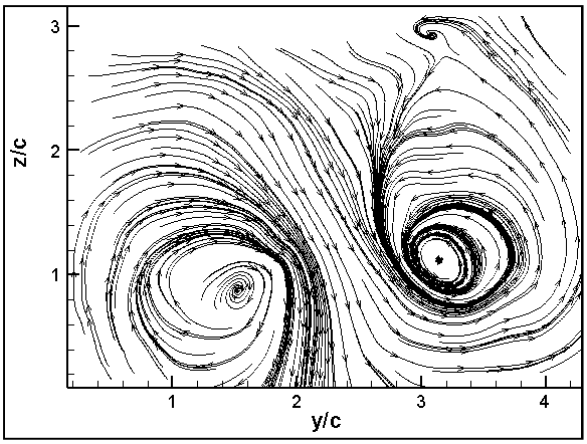

Figure-3.13: Streamline plot for 0Hz case at t* = 0.17 (Re_c = 14,000, A = 0.12 cm)

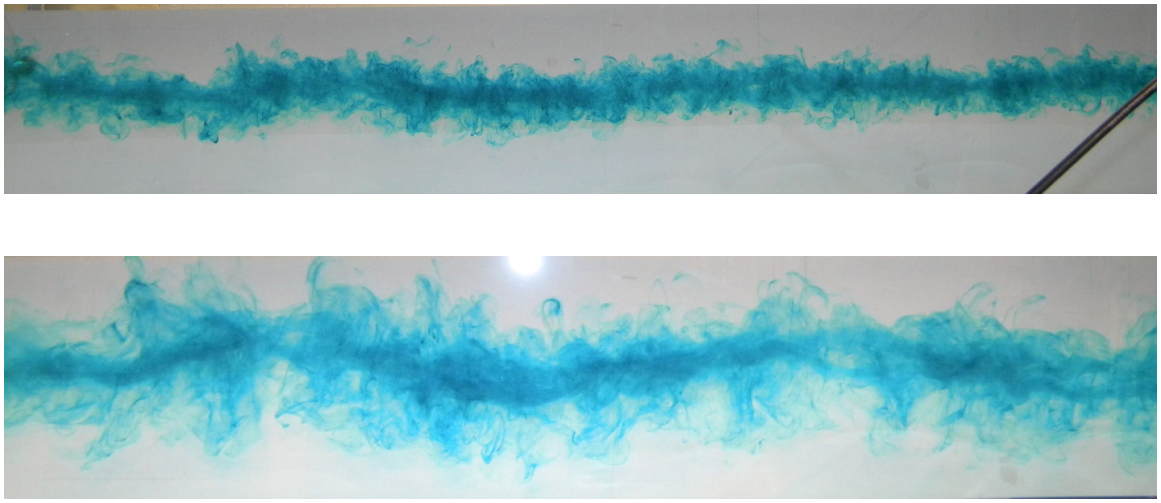

Figure-3.14: Dye Visualization showing the sinusoidal variation of the vortices for no-forcing case (a) after the wing has passed (b) few seconds after the wing has passed. (Re_c = 14,000).

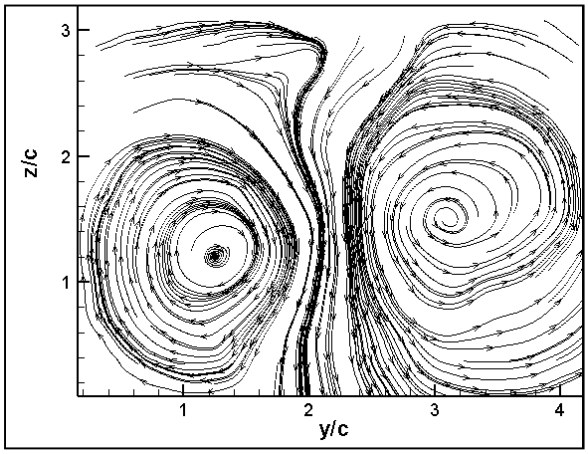

Figure-3.15: Streamline plot for 5Hz case at t* = 0.13 (Re_c = 14,000, A = 0.12 cm)

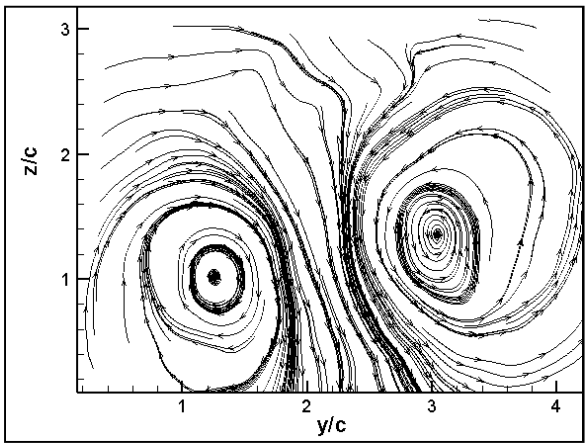

Figure-3.16: Streamline plot for 5Hz case at t* = 0.17(Re_c = 14,000, A = 0.12 cm)

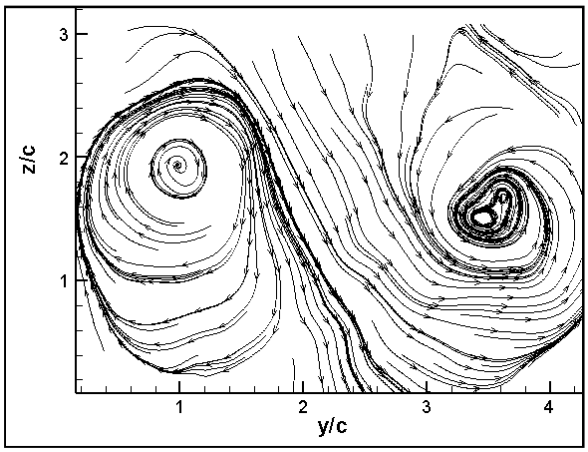

Figure-3.17: Streamline plot for 15Hz case at t* = 0.17(Re_c = 14,000, A = 0.12 cm)

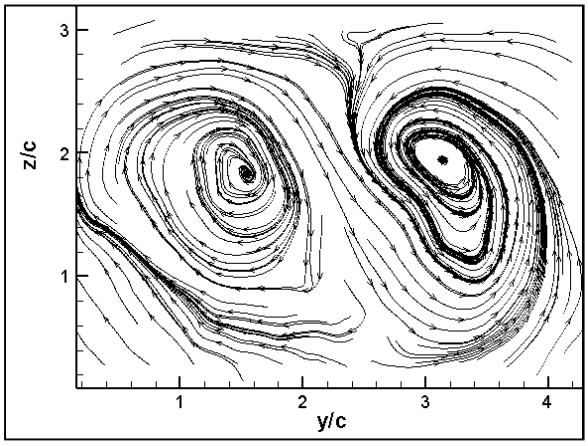

Figure-3.18: Streamline plot for 20Hz case at t* = 0.17(Re_c = 14,000, A = 0.12 cm)

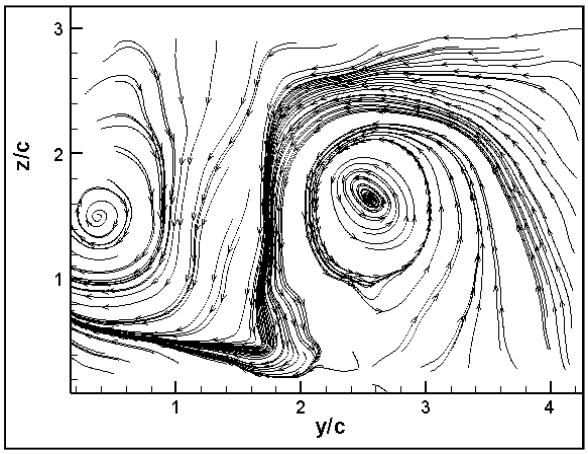

Figure-3.19: Streamline plot for 25Hz forcing t* = 0.17(Re_c = 14,000 and A = 0.12 cm)

Past efforts have shown that the counter rotating vortex pair can develop short wave elliptic instability [72]. In these past efforts, the core of each vortex had an elliptical shape. It was surmised that this effect was due to the interaction of the vorticity with the mutually induced strain [72]. The change in the internal structure of the vortex core was also observed [72]. Leweke [72] has shown that this flow field was capable of exhibiting three dimensional instabilities. Figure-3.20 shows the development of short wave elliptical instability in the counter

rotating vortex pair. For this case, $\frac{r_c}{b_0}$ = 0.2 and Re_Γ was in the range 2400-2800. For the present study, $\frac{r_c}{b_0}$ = 0.09 and Re_Γ was in the range 3800-6800.

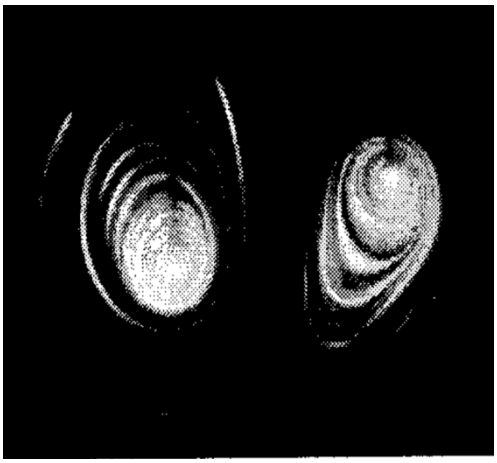

Figure-3.20: Dye visualization at t* = 7.5 showing the development of short wave instability at Re_Γ = 2400. [72]

3.2.4 Effect of forcing on the onset of instabilities:

Figure-3.21 shows the time evolution of the CRVS in the no-forcing condition. The plane of vortices rolled to some angle in the anti-clockwise direction and the spacing between the vortices decreased over time. The structure of vortices did not deform or change significantly (Figure 3.21(b)). The figures-3.21 d), e) and f) did not capture the left vortex because of the field of view restriction .It was assumed that both vortices would develop symmetric instabilities if in case any. The right vortex did not show any significant deformation in the internal structure of the vortex core until t* = 0.49. Therefore, it was clear that up to t* = 0.49, onset of any instability for no-forcing case was not observed.

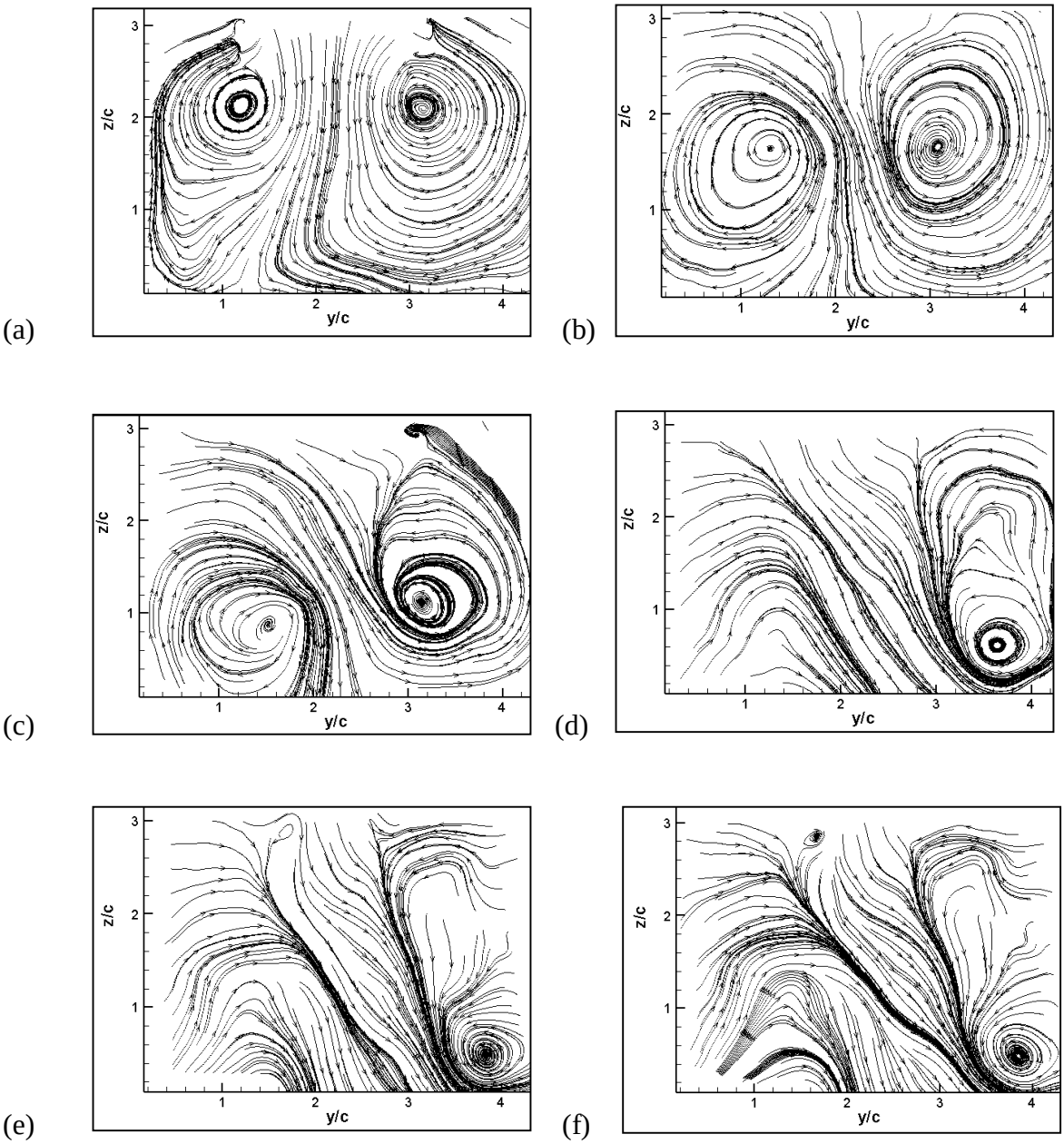

Figure-3.21: Streamline plot for 0Hz forcing at various time a) t* = 0, b) t* = 0.069, c) t* = 0.17, d) t* = 0.39, e) t* = 0.44, f) t* = 0.49 (Re_c = 14,000, A = 0.12 cm)

For 15Hz forcing case and 0.12 cm oscillation amplitude, the CRVS showed splitting and merging of core of right vortex with the left vortex remaining coherent (Figure-3.22). At t* = 0, the vortices had circular structure without any signs of deformation in the structure of the vortex core (Figure-3.22(a)). After some time, at t* = 0.069, the right vortex developed a small bulge as shown by black box (Figure-3.22(b)). This bulge grew with time and at t* = 0.17, it led to splitting of right vortex core (Figure-3.22(d)). At later times, right vortex core merged again and the left vortex remained unaffected (Figure-3.22 (e) and (f)).

When perturbed with 20Hz forcing frequency, the CRVS did show the onset as well as further development of short wave instability (Figure-3.23). At t* = 0.17, the transformation of the circular structure of the core of the vortices to elliptic shape was observed (Figure-3.23(b)). It was an indication of the development of short wave instability. The instability grew with time eventually causing splitting of both the vortices at t* = 0.46(Figure-3.23(e)). After the vortices splitted, the coherence structure of the vortices was no longer observed. The resulted flow field represented random turbulence with no coherent structures. This indicated the dissipation of the vortices (Figure-3.23(f)). Therefore, the onset of instability took place earlier for 20Hz forcing compared to no-forcing case.

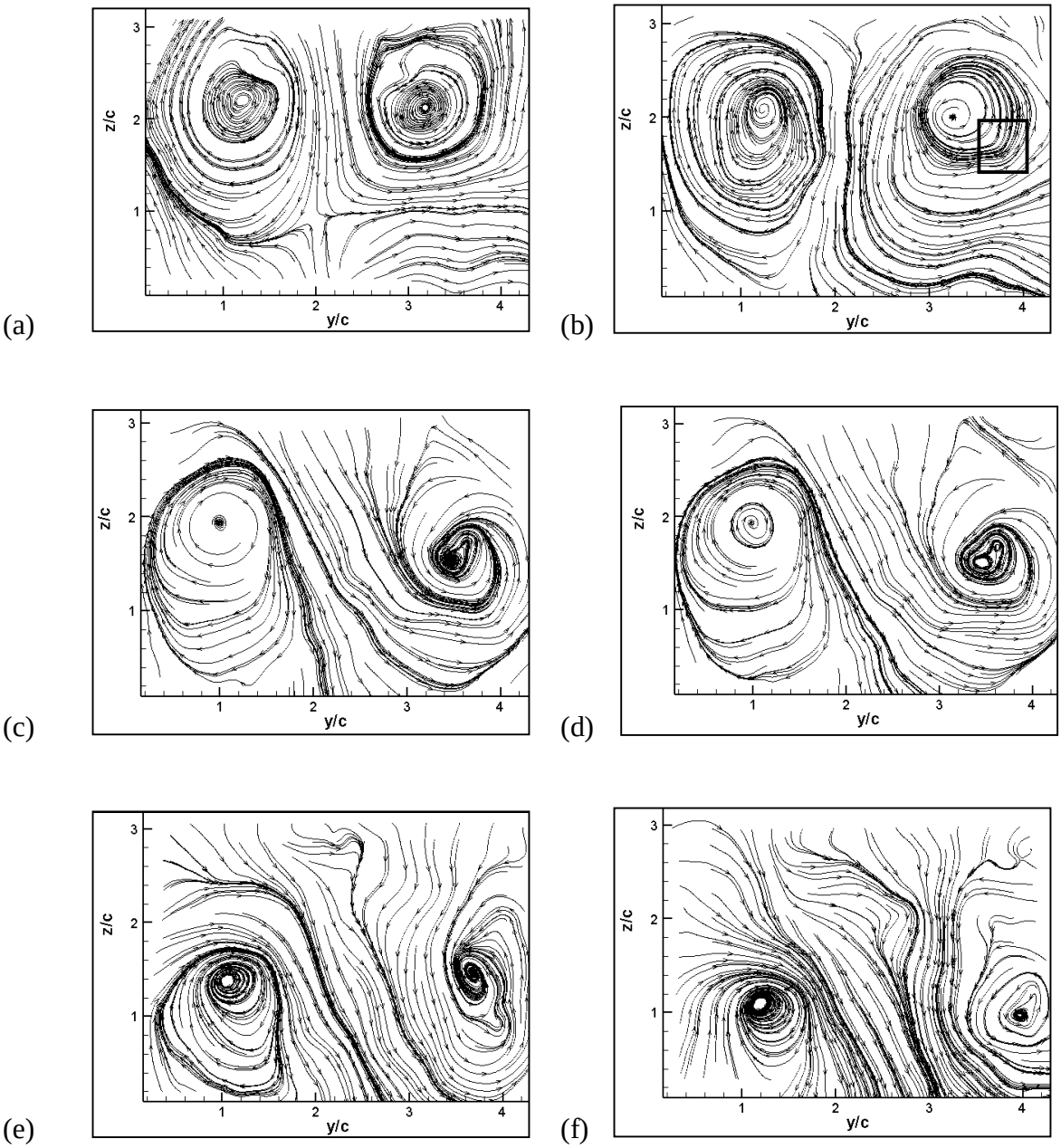

Figure-3.22: Streamline plot for 15 Hz forcing at various time a) t* = 0, b) t* = 0.069 c) t* = 0.169, d) t*=0.17, e) t* = 0.39 f) t* = 0.49(Re_c = 14,000, A = 0.12 cm)

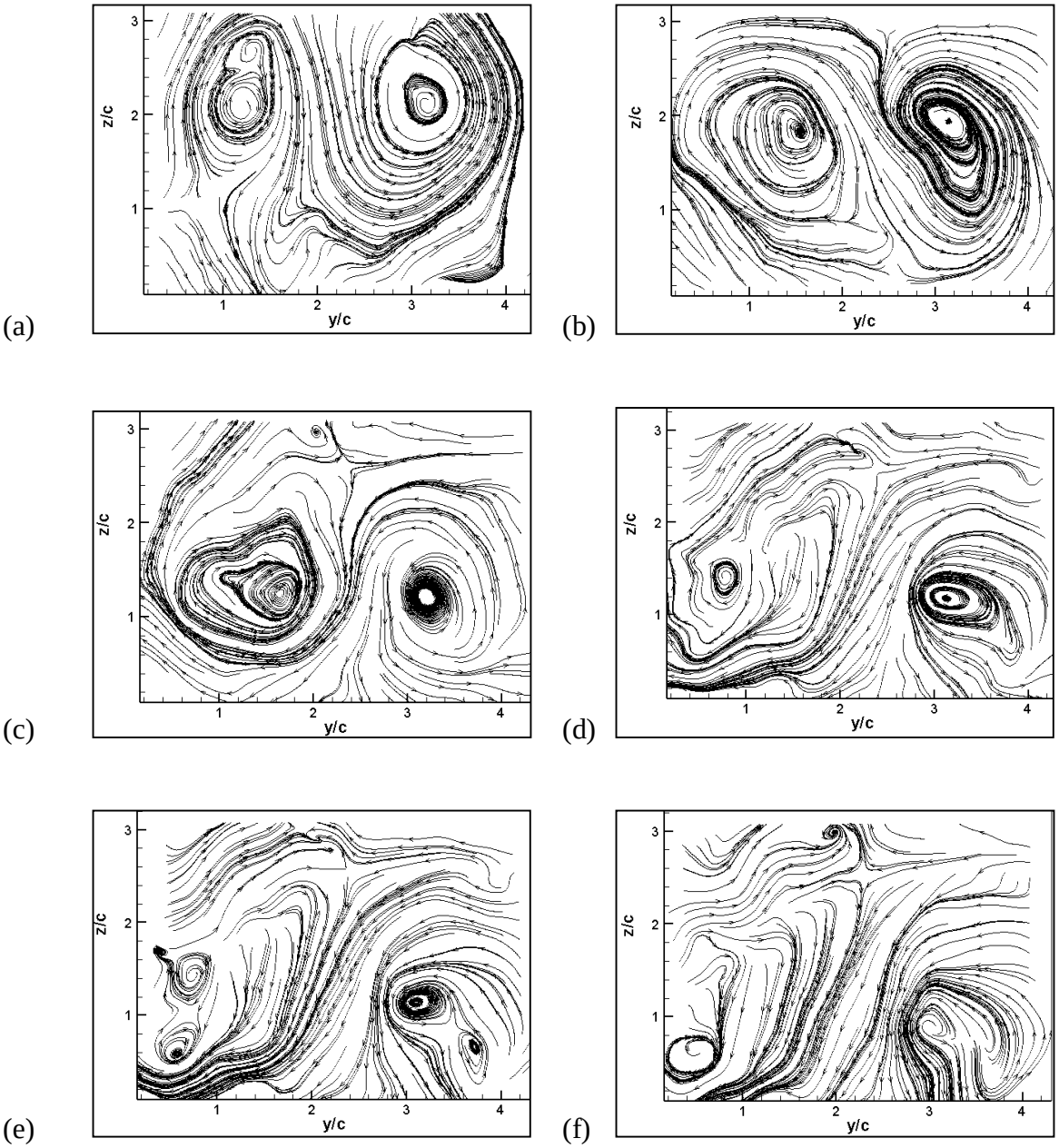

Figure-3.23: Streamline plot for 20Hz forcing at various time a) t* = 0, b) t* = 0.17 c) t* = 0.39, d) t*=0.44, e) t* = 0.46, f) t* = 0.51(Re_c = 14,000, A = 0.12 cm)

3.2.5 Effect of forcing on the various vortex parameters:

The Kinetic energy (Figure-3.24) showed a reduction with time for all forcing cases except for the 5Hz forcing frequency. This parameter represented the energy in the cross-plane

(YZ plane) of the flow field neglecting the energy in the X direction. The sudden rise in KE at t*=0.13for the case of the 5Hz, indicated that the vortices were nearly circular in shape (two-dimensional structure) (Figure-3.15). A sudden reduction in KE was also observed for 5Hz at t*=0.17. This indicated that significant velocity exists in the axial direction apart from cross – plane (Figure-3.16). Figure-3.18 showed the elliptical structure in the cross plane indicating the three –dimensional structure of the vortices [72]. Maximum reduction in KE was observed for the case of 20Hz forcing frequency (Figure-3.24). This implies a critical forcing frequency lead to increased three-dimensional nature of the vortices.

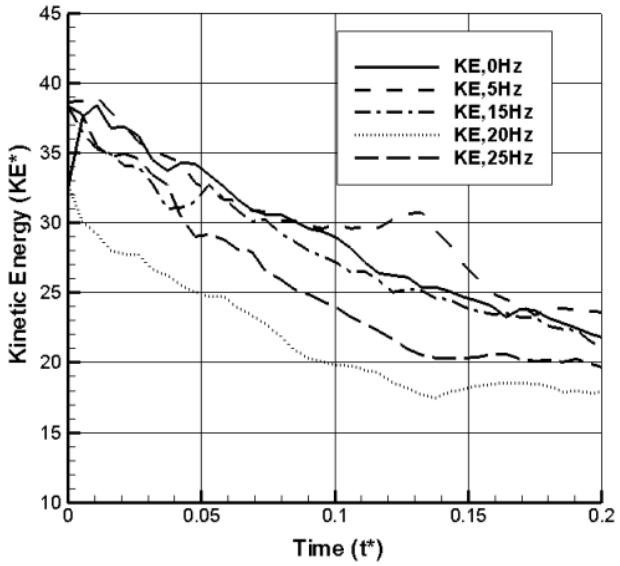

Figure-3.24: Variation of KE with time (Re_c = 14,000, A = 0.12 cm)

Maximum velocity of the left vortex increased when subjected to external perturbations for 5Hz and 15Hz but decreased for 20Hz (Figure-3.25). For the 5Hz and 15Hz case, the external perturbations caused the vortex to become stronger and have more two-dimensional characteristics (Figure-3.16 & 3.17). For the 20Hz case, as discussed earlier the left vortex develops an elliptical instability (Figure-3.18). For the right vortex, the maximum velocity

decreased very slightly for 5Hz and 15Hz where as for 20Hz, it decreased substantially. The change in maximum velocity of the right vortex was more compared to the left vortex. It is hypothesis that the external perturbations introduced in the left vortex amplified the decay of maximum velocity of the right vortex through mutual induction effects.

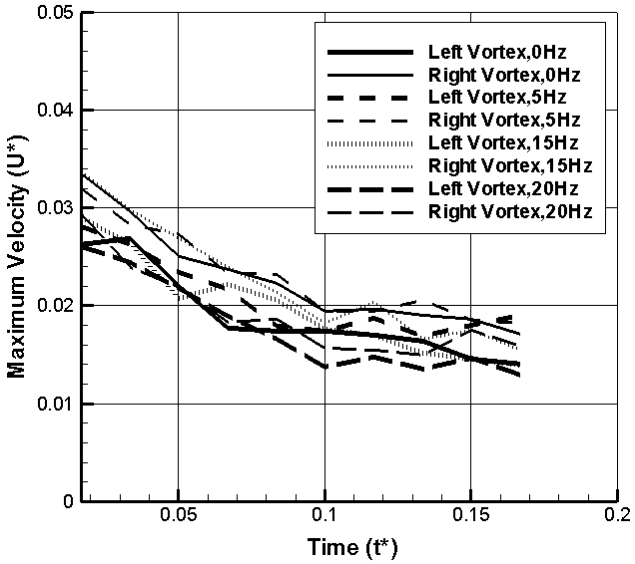

Figure-3.25: Variation of maximum velocity of vortices with time (Re_c = 14,000 and A = 0.12 cm)

Similarly the vortex core radius of the left vortex decreased for 5Hz and 15Hz but remained unchanged for 20Hz. For the right vortex, the core radius increased for all forcing cases with the increment being highest for 20Hz (Figure-3.26). The increase in growth rate of the vortex core when forced was also observed by Jacob et al [73]. Heyes and Smith [74] demonstrated that the vortex structure, growth rate and trajectory could all be altered through forcing with jets.

The maximum value of vorticity of the left vortex increased for 5Hz. This indicated that the external perturbations increased the strength of the vortex. For the 15Hz and 20Hz forcing cases, the maximum value of vorticity showed inconclusive temporal variations (Figure-3.27).

For the right vortex, the maximum vorticity values initially were higher compared to the 0Hz case for all forcing cases except 20Hz (Figure-3.28). Eventually after some time, the vorticity values for various forcing cases become equal to the no-forcing case. Comparison of various forcing cases indicated maximum change in vortex characteristics was observed at 20Hz.

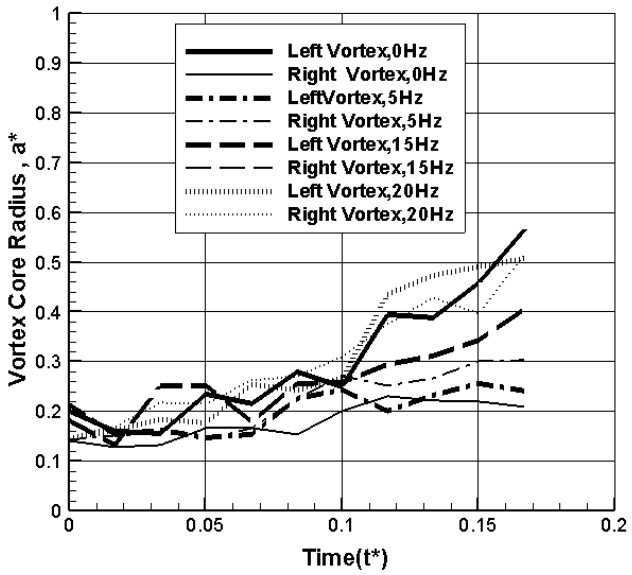

Figure-3.26: Variation of vortex core radius of vortices with time (Re_c = 14,000, A = 0.12 cm)

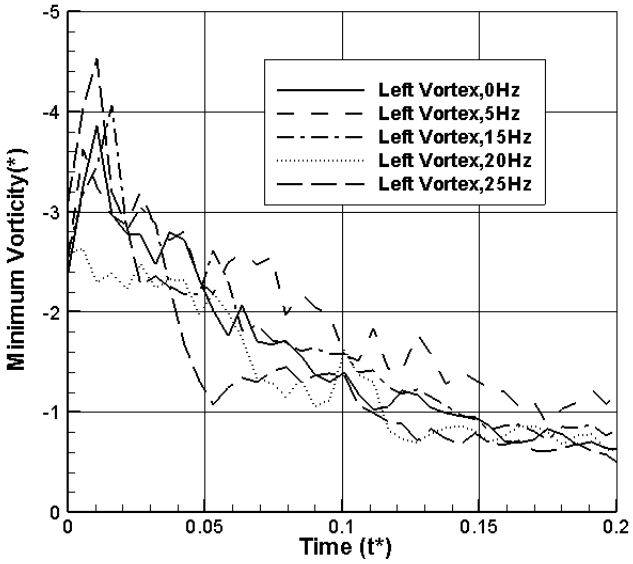

Figure-3.27: Variation of minimum vorticity with time (Re_c = 14,000 and A = 0.12 cm)

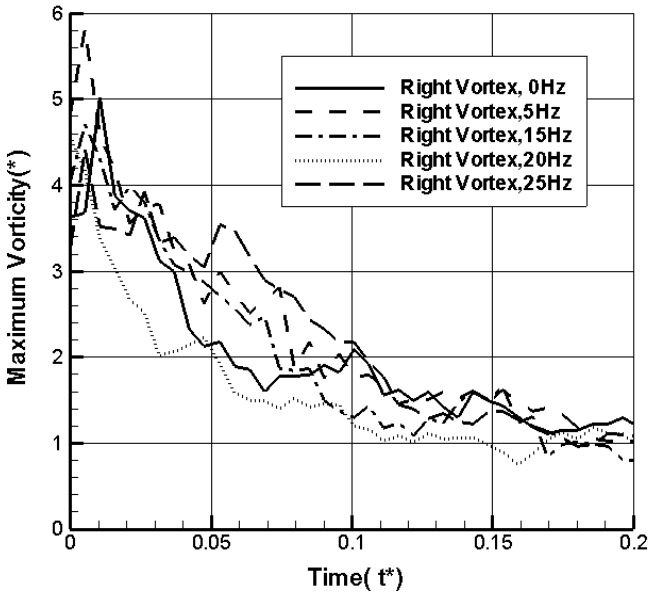

Figure-3.28: Variation of maximum vorticity with time (Re_c = 14,000, A = 0.12 cm)

Figure-3.29 shows the lateral separation between the vortices for Re_c = 14,000 and 0.12 cm oscillation amplitude. The lateral separation for the no-forcing case decreased initially (up to t* = 0.19) and then increased with time (t*= 0.29). The plane of the vortices rolled in an anti-clockwise direction to near vertical position (Figure-3.30). Tombach [75] showed that the majority of wakes rolled up to some degree, and the rolled up wakes have increased lateral separation. Sarpkaya et al and Liu [76, 77] have shown that if the lateral separation increased or decreased and the plane of vortices rolled to a near vertical position, it resulted in sinusoidal instability without vortex linking. For 5Hz forcing frequency, lateral separation remained either constant or did not vary substantially. For the case of 15Hz, lateral separation increased by a substantial amount initially up to t* = 0.16, remained constant up to t* = 0.35 and then decreased thereafter. The increase in separation of a counter–rotating vortex pair when forced was also observed by Jacob et al [74].

For the case of higher amplitude of oscillation i.e. 0.24 cm and Re_c = 14,000, the plane of the vortices tilted for all forcing cases by a variable amount. The maximum reduction in all the parameters except circulation was observed for the case of 15Hz. Any splitting or merging of core of vortices was not observed as in the case of 0.12 cm amplitude. For Re_c = 25,000, the trend observed were similar to the case of Re_c = 14,000 for most of the cases. Since the data was collected for less time at high speeds, it was difficult to comment on the onset of instabilities in most cases. For the case of 15Hz and 20Hz forcing frequencies and 0.12 cm oscillation amplitude, deformation of internal structure of the core of the vortices as well as tilting of the plane was observed. For all other cases, tilting of the plane of the vortices was observed without any deformation of the core. The results for these cases are presented in Appendix-Section-C.

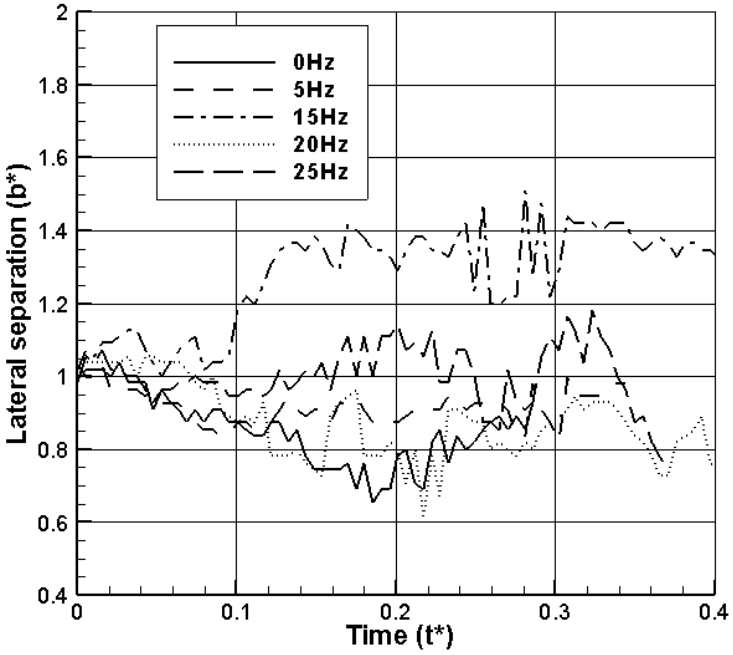

Figure-3.29: Variation of lateral separation with time (Re_c = 14,000, A = 0.12 cm)

Table-C.1 in the Appendix section C shows the descent rate values for various conditions. Figure-3.30 shows the descent rate for various forcing frequencies for Reynolds

number (Re_c = 14,000) and 0.12 cm amplitude of oscillation. The descent rate graph showed a U shaped variation with frequency both for left as well as right vortex. The bottom of the U-shaped curve was higher for the left vortex compared to right vortex. The descent rate was seen as decreasing up to 15Hz indicating that the vortex became spatially stable. Thereafter the descent rate increased for higher frequencies indicating the reduced effect of perturbations. The trend observed for the case of Re_c = 14,000 and 0.24 cm amplitude was similar to the 0.12 cm amplitude case. Outlier points were noted for the case of 30Hz which did not fit into existing U-shaped trend lines. For Re_c = 25,000 the trend observed was similar to a Gaussian distribution with less difference between the forcing and no-forcing descent velocities. The results for other conditions are presented in Appendix section C.

Effect of forcing is more prominent at low free stream velocity and small amplitudes. This is confirmed by the depth of the U-shaped descent velocity graphs which seems to become shallower for higher wing speeds and higher oscillations. Despite this, the inflection points of the U- shaped curve are in the range of 12-17 Hz. For the same conditions, the descent of the left vortex was higher. This was likely due to the diminishing effect of perturbation with distance from the source. Since the left vortex was closer to source, the effect was higher compared to the right vortex which was further away.

The vortex structure can be altered by flow field turbulence. Prior studies [76, 77] have shown that the effect of ambient turbulence is to inhibit the migration and life span of vortices. In weak turbulence, sinusoidal instability and the subsequent instability events destroy the vortices. In medium to strong turbulence, the dominant form of instability is the vortex bursting [77]. For the current effort, a decrease in descent velocity was observed for all forcing cases and is an indication of initiation of one of the two instability mechanisms. Since the LAROF dimensions

were small and the amplitude of oscillations was small, it was expected that this was a case of adding weak turbulence to the flow. Therefore there is a higher possibility of initiation of sinusoidal instability. It was clear that vortex bursting was not the dominant form of instability because a sudden increase in the radius of the core was not observed for any case.

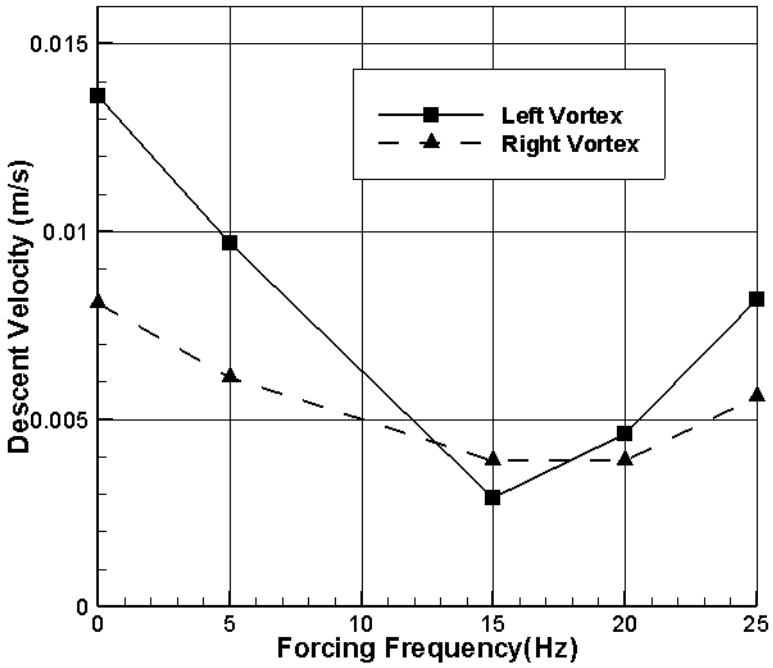

Figure 3.30: Descent rates versus forcing frequencies (Re_c = 14,000, A = 0.12 cm)

4. Hot-Film Anemometry Results

All tests were carried out at two Reynolds numbers: 14,000 and 25,000. LAROF at the tip of the wing was used for introducing 2D perturbations into the flow field at desired frequencies and amplitudes. Hot-film anemometry was used to determine the power spectral density plots for various cases. It was also used to monitor the decay of the voltage at a fixed point in the flow field. The tests were carried out for SVS as well as CRVS.

4.1 Effect of forcing on single tip vortex:

To measure the power spectral density as well the decay time of the signal, a single hot-film was placed alongside the trailing edge of the wing. The decay time of the signal is defined as the time taken for the voltage value to decay from the maximum value to 25 percent of the maximum value (Figure-4.1). The maximum value of the voltage i.e. maximum fluctuations in each case was obtained when the wing passed the hot-film probe. The PSD for SVS for $Re_c = 14{,}000$ and oscillation amplitudes (0.12 cm and 0.24 cm) were plotted. Various forcing frequencies were considered for comparison with the standard case. The frequency scale was limited to be in the range 0-50 Hz.

Figure-4.2 shows the power spectra for the no-forcing case. When the vortex was forced with external perturbations, the power spectra plots showed the dominant frequencies in the system. For 5Hz and 10Hz forcing frequency, the plots (Figure-4.3 and Figure-4.4) showed

random noise without any dominant frequency. In the case of 15Hz forcing frequency, the fundamental frequency was found to be 15Hz with harmonics at 30Hz, 45Hz, 60Hz, 75Hz, and 90Hz. Similarly for 20Hz forcing frequency, the fundamental frequency was found to be 20Hz with harmonics at 40Hz, 60Hz and 80Hz. Therefore, higher frequencies are dominant in power spectra more than the lower frequencies.

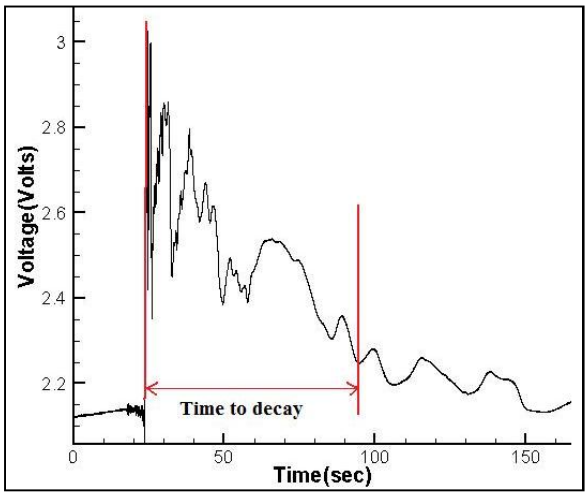

Figure-4.1: Hot-film data for a sample case showing time to decay

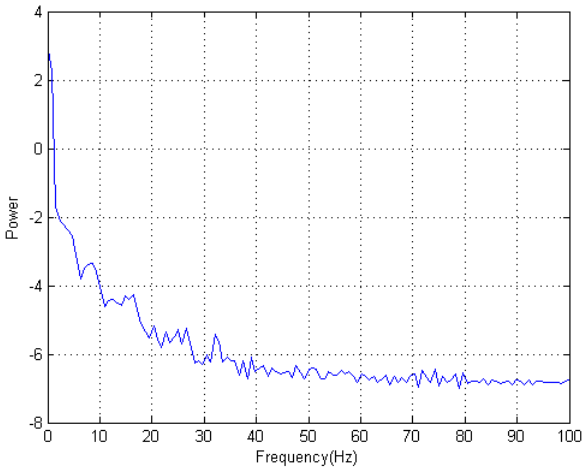

Figure-4.2: PSD plot for no-forcing (Re_c = 14,000)

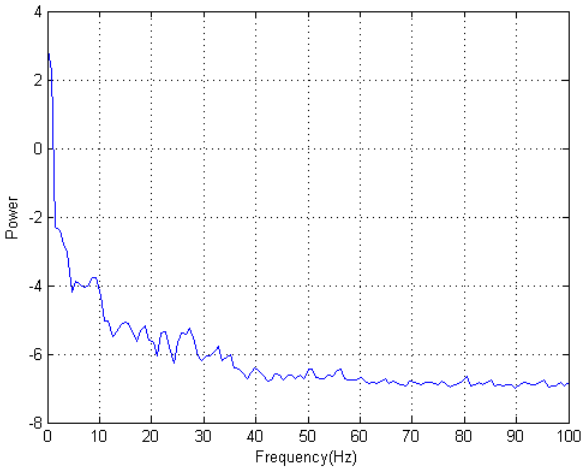

Figure-4.3: PSD plot for 5Hz forcing frequency (Re_c = 14,000, A = 0.12 cm)

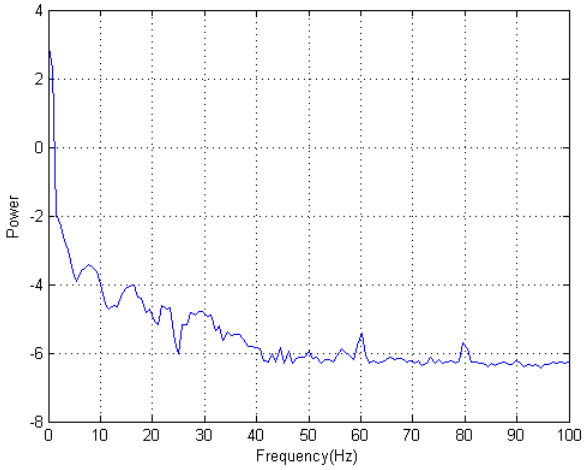

Figure-4.4: PSD plot for 10Hz forcing frequency (Re_c = 14,000, A= 0.12 cm)

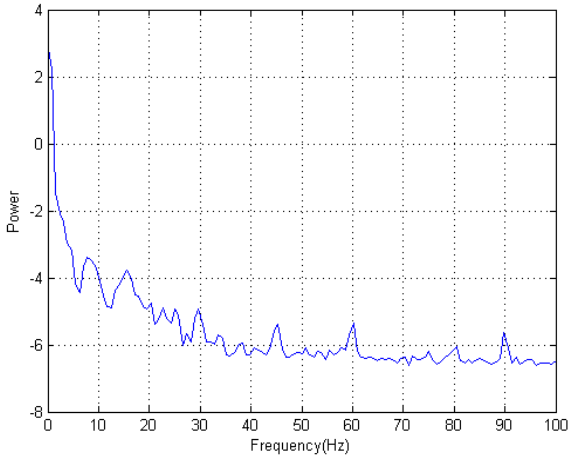

Figure-4.5: PSD plot for 15Hz forcing frequency (Re_c = 14,000 and A = 0.12 cm)

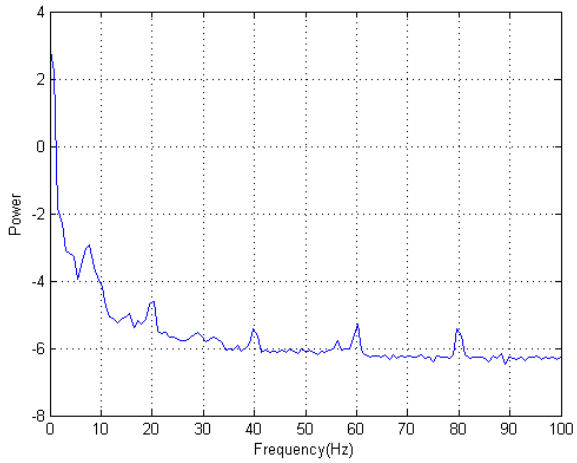

Figure- 4.6: PSD plot for 20Hz forcing frequency (Re_c = 14,000 and A = 0.12 cm)

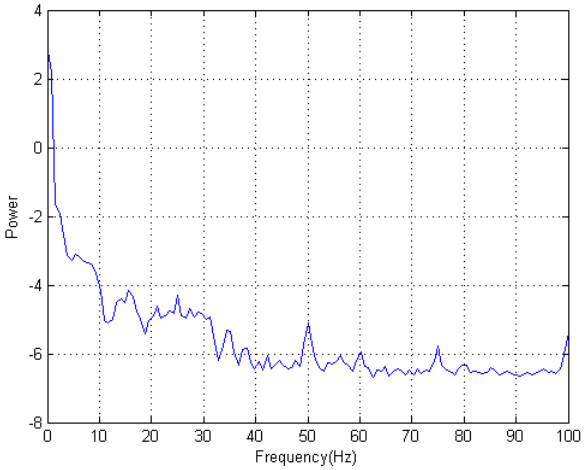

Figure- 4.7: PSD plot for 25Hz forcing frequency (Re_c = 14,000 and A = 0.12 cm)

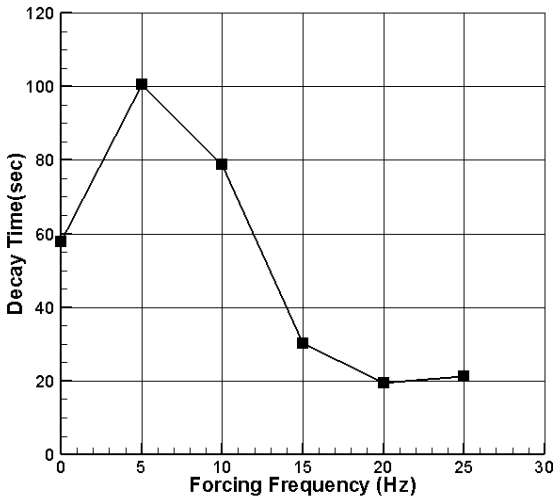

Figure-4.8: Time to decay for different forcing frequencies (Re_c = 14,000, A = 0.12 cm)

The decay time increased for 5 Hz and 10Hz case compared to no-forcing case. This indicated that the vortex dissipated slowly. The decay time was found to be the least for the 20Hz case (Figure-4.8). This indicated that the vortex has dissipated quicker in the case of 20Hz forcing frequency.

For the case of 0.24 cm amplitude and Re_c = 25,000, the decay time is least for 25 Hz forcing frequency. For the similar conditions, the low-amplitude oscillations resulted in quicker decay of fluctuations. Hence, it is an indication of faster decay of vortices. The decay time for Re_c = 25,000, was more for various forcing cases compared to the no-forcing case. The external perturbations introduced at high speeds did not result in quicker decay of vortices. The figures for these additional cases are presented in Appendix-D

4.2 Results for CRVS:

A single hot-film was placed midway between the two wings to measure the power spectral density as well as the decay time of the signal. The PSD for CRVS for Re_c = 14,000 & 25,000 and oscillation amplitudes (0.12 cm & 0.24 cm) were plotted. Various forcing frequencies were considered for comparison with the standard case. Figure-4.9 shows the PSD plots for no-forcing case for CRVS. The dominant frequencies were observed at 9.8Hz and 15Hz. Similar to the single vortex case; the higher frequencies (15Hz, 20Hz, and 25Hz) were visible in the PSD plots compared to the lower frequencies (Figure- 4.11-4.13) .The heights of the peak were higher compared to the SVS for all case. This may be due the effect of mutual induction of the vortices in the CRVS. The figures for these additional cases are presented in Appendix-E.

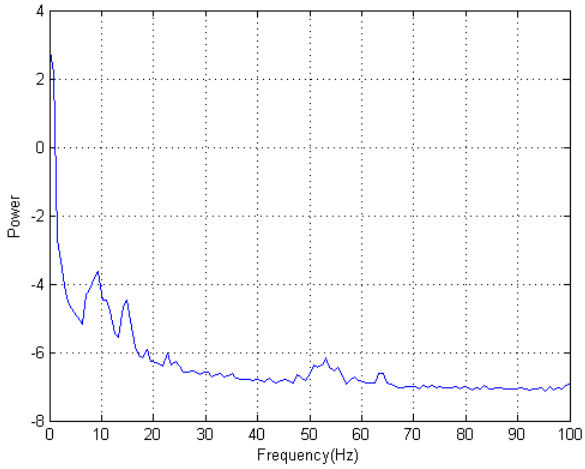

Figure-4.9: PSD plot for no-forcing for CRVS ($Re_c = 14,000$)

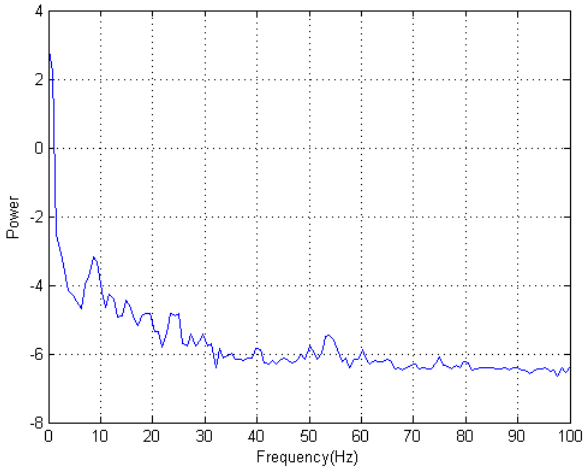

Figure-4.10: PSD plot for 5Hz forcing frequency ($Re_c = 14,000$, A = 0.12 cm)

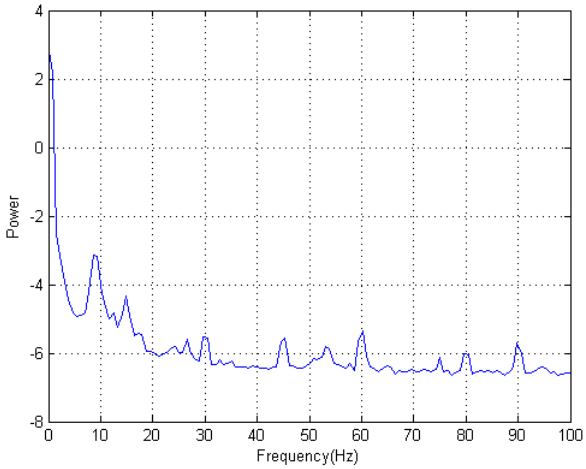

Figure-4.11: PSD plot for 15Hz forcing frequency ($Re_c = 14,000$, A = 0.12 cm)

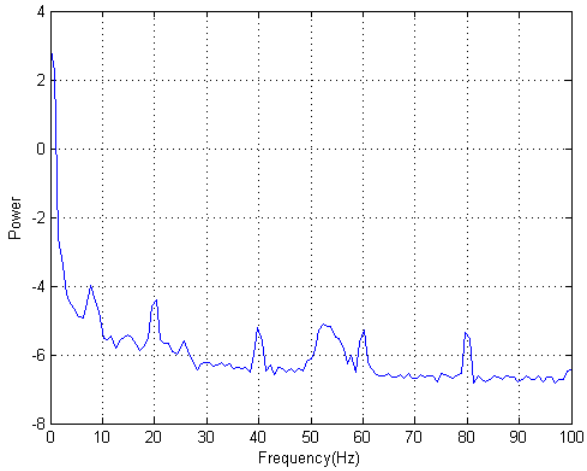

Figure -4.12: PSD plot for 20Hz forcing frequency (Re_c = 14,000, A = 0.12 cm)

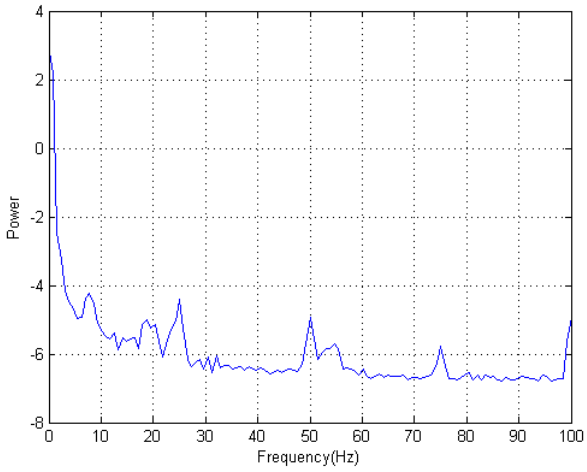

Figure- 4.13: PSD plot for 25 Hz forcing frequency (Re_c = 14,000, A = 0.12 cm)

The decay time increased for 15 Hz case compared to no-forcing case. This indicated that fluctuations caused due to the presence of vortex exist for a longer time for 15Hz case. This implies either the perturbed or unperturbed vortex or both dissipated slowly. PIV results for 15Hz case showed the perturbed vortex strengthens and the unperturbed vortex develops instability. Hence the time to decay is higher for the case of 15Hz. The decay time was found to be the least for the 20Hz case (Figure-4.14). This indicated that the vortices have dissipated quicker in the case of 20Hz forcing frequency. PIV results for 20Hz case shows that both the

vortices developed an elliptic instability which lead to splitting of the vortices. Thereafter the coherence of the vortices was lost. Hence the decay time for the 20Hz forcing was found to be least.

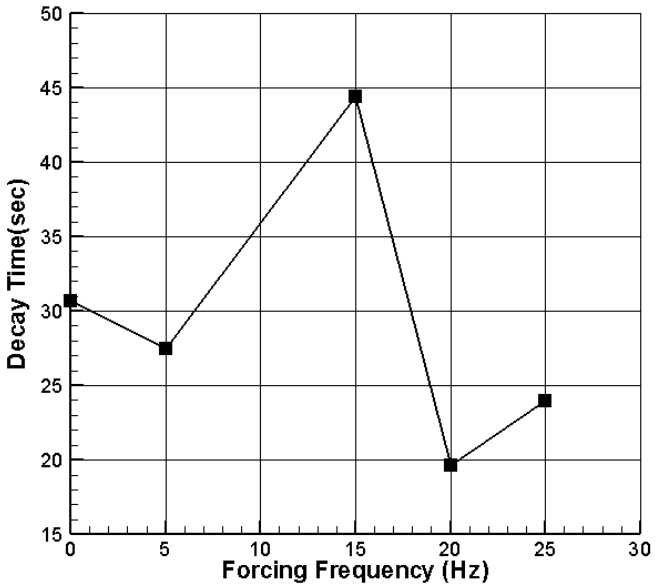

Figure-4.14: Time to decay for different forcing frequencies

(Re_c = 14,000, A = 0.12 cm)

5. Conclusions

The excitation of instabilities inherent in the tip vortices were investigated using external perturbations introduced by a Low-Aspect Ratio Induced Flap (LAROF) at the trailing edge of one of the two wings. Experiments were conducted at two different Reynolds numbers, two different oscillation amplitudes and various forcing frequencies.

For the SVS, theoretical validation was conducted and it was found that the Lamb-Oseen model showed the best fit to the experimental data. For a Reynolds number of 14,000, when forced with external perturbations, the SVS showed signs of reduction in maximum velocity, minimum vorticity, kinetic energy and increment in the vortex core radius for all forcing cases. The circulation of the system remained unchanged. Excitation of instabilities inherent in the SVS was not observed.

For the CRVS, when forced with external perturbations, some cases showed signs of earlier onset of instabilities. For a Reynolds number of 14,000, flow visualization results showed the sinusoidal oscillations of the vortices for the no–forcing case. This indicates the development of the long-wave crow instability. The wavelength of the instability was found equal to $7.8b_0$ which are close to theoretical predictions. The PIV results showed tilting of the plane of the vortices for all forcing case except at 15Hz and 20Hz for 0.12 cm oscillation amplitude. For the case of 15Hz forcing frequency, splitting and merging of the unperturbed vortex was observed.

The perturbed vortex was seen to grow in strength. For the case of 20Hz, short wave elliptical instability was observed with the vortices splitting after some time. This led to quicker decay of the vortices for the case of 20Hz compared to the no-forcing case. Similar trends and instabilities were not observed at higher oscillations amplitudes. The descent rate decreased for the overall system with forcing. The cross-plane kinetic energy of the overall system decreased with forcing indicating three-dimensional effects. At a Reynolds number of 25,000, trends similar to the lower Reynolds number case was observed. Additionally, tilting of the vortex plane was observed for higher Reynolds number case, 15Hz and 20Hz forcing frequencies and 0.12cm oscillation amplitude. Such tilting was not observed for the lower Reynolds number case. Hot-Film Anemometry results showed a reduction in decay time for the overall system for most of the forcing cases. For a Reynolds number of 14,000, the reduction in decay time was highest for 20Hz forcing case for 0.12 cm oscillation amplitude. Higher amplitudes did not result in a significant reduction in decay times for various forcing cases. Hence low oscillation amplitudes at Reynolds number of 14,000 lead to quicker decay of vortices.

This active-control technique was found to be more efficient compared to the previously tried techniques since it involved oscillations of only one surface. Therefore, the power required to control this surface was lesser than the other alternatives. The oscillation of only one control surface at 20Hz showed earlier onset of instabilities compared to the standard case. It is hypothesized that oscillation of two surfaces i.e. one on each wing would result in even quicker decay of vortices. Future work would involve investigating the effect on instabilities with oscillation of two surfaces i.e. one on each wing. The effect of external perturbation on merger characteristics of the co-rotating vortices will also be studied.

References

1. Widnall, S. E., "The Structure and Dynamics of Vortex Filaments," *Annual Review of Fluid Mechanics*, Vol.7, Jan. 1975, pp.141–165.
2. Leweke, T., and Williamson, K. H. C., "Three-Dimensional Instabilities of a Counterrotating Vortex Pair," Lecture notes in physics, Vol. 555, 2000, pp.221-230
3. Chambers, J. R., "Concept to Reality: Contributions of the Langley Research Center to U.S. Civil Aircraft of the 1990s," NASA SP-2003-4529, 2003.
4. Image Reference: www.airliners.net
5. Hallock, J. N., and Ebeile, W .R, "Aircraft Wake Vortices, a State of the Art Review of the United States," FAA-RD-77-23, 1977.
6. Matalanis, G. C., and Eaton, K. J., "Wake Vortex Alleviation Using Rapidly Actuated Segmented Gurney Flaps," Report No 102, Stanford University, Jan. 2007.
7. Mack, G. R., "Wake Vortices Effects and the Need for Prompt Action–A U.S.View," AGARD CP-58.1996
8. National Research Council "Wake Turbulence – An Obstacle to increased Air Traffic Capacity,"
9. Green, S.I., "Wing Tip Vortices," *Fluid Vortices*, 1st ed., Springer, March.1995, pp. 427-460.
10. McCluer, S.M., "Helicopter Blade-Vortex Interaction Noise with Comparisons to CFD Calculations," NASA Technical Memorandum 110423, Dec. 1996

11. Crouch, J.D., et al, “Active Control System for Breakup of Trailing Vortices,” *AIAA Journal*, Vol. 39, No.12, 2001, pp.2374–2381.
12. Huffaker, R. M., and Jelalian, A.V., and Thomson, J. A. L., “Laser-Doppler System for Detection of Aircraft Trailing Vortices,” *Proceedings of the IEEE*, Vol. 58, No.3, 1970, pp.322–326.
13. Thomson, J. A. L., and Meng, J. C. S., “Scanning Laser Doppler Velocimeter System Simulation for Sensing Aircraft Wake Vortices,” *Journal of Aircraft*, Vol.13, No.8, 1976, 605–613.
14. Hannon, S. M., and Thomson, J. A., “Aircraft Wake Vortex Detection and Measurement with Pulsed Solid-State Coherent Laser Radar,” *Journal of Modern Optics,* Vol.41, No.11, 1994, pp. 2175–2196.
15. Harris, M., Young, R. I., Kopp, F., Dolfi, A., and Cariou, J.P., “Wake Vortex Detection and Monitoring,” *Aerospace Science and Technology*, Vol.6, 2002, pp. 325–331.
16. Keane, M., Buckton, D., and Redfern, M., “Axial Detection of Aircraft Wake Vortices Using Doppler Lidar,” *Journal of Aircraft*, Vol.39, No.5, 2002, pp.850–861.
17. Rubin, W. L., “Radar-Acoustic Detection of Aircraft Wake Vortices,” *Journal of Atmospheric and Oceanic Technology*, Vol.17, 2000, pp.1058–1065.
18. Boluriaan, S. and Morris, P. J., “Numerical Simulation of Wake Vortex Detection Using a Radio Acoustic Sounding System,” *AIAA Journal* ,Vol,39, No.6, 2001, pp.1097–1105.
19. Boluriaan, S. and Morris P. J., “Two-Dimensional Simulations of Wake Vortex Detection Using Radio Acoustic Sounding Systems,” *AIAA Journal*, Vol.40, No.11, 2002, pp. 2247–2256.

20. Shariff, K., and Wray, A., “Analysis of the Radar Reflectivity of Aircraft Vortex Wakes,” *Journal of Fluid Mechanics*, Vol.463, 2002, pp.121–161.

21. Hinton, D. A., “An Aircraft Vortex Spacing System (AVOSS) for Dynamical Wake Vortex Spacing Criteria” AGARD CP-584, 1996.

22. Rossow, V. J., “Theoretical Study of Lift Generated Vortex Wakes Designed to Avoid Rollup,” *AIAA Journal*, Vol.13, No.4, 1975, pp.476–484.

23. Holbrook, G. T., Dunham, D. M., and Greene, G. C., “Vortex Wake Alleviation Studies With a Variable Twist Wing”, NASA TP 2442, 1985.

24. Corsiglia, V. R., and Dunham, R. E., “Aircraft Wake-Vortex Minimization by Use of Flaps in Wake Vortex Minimization,” SP-409, 1976.

25. Graham, W. R., Park, S.W., and. Nickels, T. B., “Trailing Vortices from a Wing with a Notched Lift Distribution,” *AIAA Journal*, Vol.41, No.9, 2003, pp.1835–1838.

26. Lezius, D. K., “Unstable Wing Vortex Rollup Induced by Lift Tailoring in the Wing-Tip Region,” *In Proceedings of the Aircraft Wake Vortices Conference* - Vol. 1, 1975.

27. Patterson, J. C., “Vortex Attenuation Obtained in the Langley Vortex Research Facility,” *Journal of Aircraft*, Vol.12, No.9, 1975, pp.745–749.

28. Traub, L. W., Mani, S., and Rediniotis, O. K., “Application of the Vortex Breakdown Phenomenon in the Attenuation of Trailing Vortices,” *The Aeronautical Journal*, Vol. 102, 1998, 439–444.

29. Croom, D. R., “Evaluation of Flight Spoilers for Vortex Alleviation,” *Journal of Aircraft* Vol. 14, No. 8, 1977, pp.823–825.

30. Rossow, V. J., “Effect of Wing Fins of Lift-Generated Wakes,” *Journal of Aircraft*, Vol.15, No.3, 1978, pp.160–167.

31. Schell, I., Ozger, E., and Jacob, D., "Influence of Different Flap Settings on the Wake-Vortex Structure of a Rectangular Wing with Flaps and Means of Alleviation with Wing Fins," *Aerospace Science and Technology*, Vol. 4, 2000, pp.79–90.
32. Ozger, E., Schell, I., and Jacob, D., "On the Structure and Attenuation of an Aircraft Wake," *Journal of Aircraft*, Vol.38, No.5, 2001, pp.878–887.
33. Heyes, A. L., and Smith, D.A.R., "Modification of a Wing Tip Vortex by Vortex Generators", *Aerospace Science and Technology*, Vol.9, 2005, pp.469–475.
34. Scholl, R. H., Buxel, C., and Neuwerth, G., "Influence of Spanwise Loading and Fins on Extended Near-Field Vortex Wake," AIAA Paper-62, 2006.
35. Tanaka, S., Kaibara, M., and Tanaka, A., "Decay and Modification of Trailing Vortex," Bulletin of the JSME, Vol.21, No.151, 1978, pp.98–103.
36. Simpson, R. G., Ahmed, N. A., and Archer, R. D., "Near Field Study of Vortex Attenuation Using Wing-Tip Blowing," *The Aeronautical Journal*, 2002, pp.117–120.
37. Zhou, Y., and Zhang, H. J., "Wing-Tip Vortex Measurement with Particle Image Velocimetry," AIAA Paper-2433, 2004.
38. Bearman, P., Heyes, A., Lear, C., and Smith, D., "Natural and Forced Evolution of a Counter Rotating Vortex Pair," *Experiments in Fluids*, Vol. 40, No.1, 2006, pp.98-105.
39. Ortega, J. M., Bristol, R. L., and Savas, O., "Wake Alleviation Properties of Triangular-Flapped Wings," *AIAA Journal*, Vol.40, No.4, 2002, pp.709–721.
40. Ortega, J. M., Bristol, R. L., and Savas, O., "Experimental Study of the Instability of Unequal-Strength Counter-Rotating Vortex Pairs," *Journal of Fluid Mechanics*, No.474, 2003, pp.35–84.

41. Stumpf, E., “Numerical Study of Four-Vortex Aircraft Wakes and Layout of corresponding High-Lift Configurations,” AIAA Paper-1067, 2004.
42. Durston, D. A., Walker, S.M., Driver, D. M., and Smith, S.C., “Wake-Vortex Alleviation Flow field Studies,” *Journal of Aircraft*, Vol.42, No.4, 2006, pp.894–907.
43. Haverkamp, S., Neuwerth, G., and Jacob, D., “Active and passive vortex wake mitigation using control surfaces,” *Aerospace Science and Technology*, Vol.9, 2005, pp.5–18.
44. Crow, S.C., “Aircraft Wake Turbulence and Its Detection,” 1971, pp. 551–582.
45. Chevalier, H., “Flight Test Studies of the Formation and Dissipation of Trailing Vortices,” *Journal of Aircraft*, Vol.10, No.1, 1973, pp.14–18.
46. Crow, S.C., and Bate, E.R., “Lifespan of trailing vortices in a turbulent atmosphere,” *Journal of Aircraft*, Vol.13, 1976, pp.476–482.
47. Bilanin, A.J., and Widnall, S.E., “Aircraft wake dissipation by sinusoidal instability and vortex breakdown,” AIAA Paper No.73-107, 1973.
48. Barber, M. R., and Tymczyszyn, J.J., “Wake Vortex Attenuation Flight Tests,” NASA CP-2170, 1980.
49. Jordan, F. L. J., “Flow Visualization of the Wake of a Transport Aircraft Model with Lateral-Control Oscillations”, NASA TM-84623, 1983.
50. Rossow, V. J., “Wake Hazard Alleviation Associated with Roll Oscillations of Wake Generating Aircraft,” *Journal of Aircraft*, Vol.23, No.6, 1986, pp.484-491.
51. Crouch, J.D., “Stability of multiple trailing-vortex pairs,” AGARD-CP-584, 1996, pp.17-1–17-8.
52. Crouch, J.D., et al, “Instability and transient growth for two trailing-vortex pairs,” *Journal of Fluid Mechanics*, Vol.350, 1997, pp.311–330.

53. Rennich, S.C., and Lele, S.K., “A method for accelerating the destruction of aircraft wake vortices,” *Journal of Aircraft*, Vol.36, 1999, pp.398–404.

54. Fabre, D., and Jacquin, L., "Stability of a four-vortex aircraft wake model,” *Physics of Fluids*, Vol. 12, 2000, pp.2438–2443.

55. Fabre, D., Jacquin, L., and Loof, A., “Optimal perturbations in a four-vortex aircraft wake in counter-rotating configuration,” *Journal of Fluid Mechanics*, Vol. 451, 2002, pp. 319–328.

56. Ortega, J., and Savas, O., “Rapidly growing instability mode in trailing multiple-vortex wakes,” *AIAA Journal*, Vol. 39, 2001, pp.750–754.

57. Jacquin, l., Fabre, D., Geffroy, P., and Coustols, E., “The properties of a transport aircraft wake in the extended near-field: an experimental study,” AIAA Paper No.1038, 2001.

58. Kauertz, S., and Neuwerth, G., “Excitation of instabilities in the wake of an airfoil by means of active winglets,” *Aerospace Science and Technology*, 2006, pp.551-562.

59. Abbott, I. H., and Doenhoff, A.E.V., “Airfoil Co-ordinates,” *Theory of Wing Section*, Dover, Jun.1959, pp. 406-449.

60. Savas, O., “Experimental Investigations on Wake Vortices and their Alleviation,” C.R.Physique, Vol.6, 2005, pp.415-429.

61. Rokhsaz, K., “Exploratory study of aircraft wake vortex filaments in water tunnel,” *Journal of aircraft*, Vol.37, No.6, 2000, pp.1022-1027.

62. Williamson, C.H.K., and Leweke, T., “Fundamental Instabilities in a spatially – Developing Wing Wakes and Temporally-Developing Vortex Pairs,” *Proceedings of FEDSM’98*, ASME Fluids Engineering Division Summer Meeting, Washington DC, 1998.

63. Gerz, T., Holzapfel, F., and Darracq D., “Commercial aircraft wake vortices,” *Progress in Aerospace Sciences*, Vol. 38, 2002, pp.181-208.

64. Lamb, H., “Viscosity,” *Hydrodynamics*, 6th ed., Dover, New York, 1923, pp. 592.

65. Burnham, D.C., and Hallock, J.N., “Chicago monostatic acoustic vortex sensor system,” Report No. DOT-TSC-FAA-79- 103.IV, July 1982, pp.206.

66. Proctor, F.H., “The NASA-Langley wake vortex modeling effort in support of an operational aircraft spacing system,” *AIAA Conference Proceeding*, 1998-0589, 1998, pp.14.

67. Winckelmans, G.S., Thirifay, F., and Ploumhans, P., “Effect of non-uniform wind shear onto vortex wakes: parametric models for operational systems and comparison with CFD studies,” Amsterdam, Netherlands, October 16–17, 2000.

68. Orgeta, M. J., “Stability Characteristics of Counter Rotating Vortex Pairs in the Wakes of Triangular-Flapped Airfoils ," Ph. D. Dissertation, Department of Aerospace Engineering , University of California, Berkeley, 2001.

69. Kelvin, “On the Vibrations of a columnar vortex,” Pilos.Mag.10,155,1880

70. Rossow, J. V., “Lift-generated vortex wakes of subsonic transport aircraft,” *Progress in Aerospace Sciences*, Vol. 35, 1999, pp.507-660.

71. Eliason, B. G., Gartshore, I. S., and Parkinson, G. V., “Wind Tunnel Investigation of Crow Instability,” *Journal of Aircraft*, Vol.12, Dec. 1975, pp.985-988.

72. Leweke, T., and Williamson, C. H. K., “Cooperative elliptic instability of a vortex pair,” *Journal of fluid mechanics*, Vol.360, 1998, pp.85-119.

73. Jacob, Liepmann, J.D, and Savas, O., “Characterisation and Modification of Wakes from Lift,” Vehicles in Fluids, AGARD, CP-584, 1996, pp 27:1-12.

74. Heyes , A. L., and Smith, D. A. R., “Spatial perturbation of a wing-tip vortex using pulsed span-wise jets,” *Experiments in Fluids,* Vol.37, No.1,2004,pp.120-127.

75. Tombach, I., “Observations of Atmospheric Effects on Vortex Wake Behavior,” *Journal of Aircraft,* Vol.10, No.11, Nov 1973, pp.641-647.

76. Sarpkaya, T., and Daly, J.J., “Effect of Ambient Turbulence on Trailing Vortices,” *Journal of Aircraft,* Vol. 26, No.6, June 1987, pp.399-404.

77. Liu, H.T., "Effects of Ambient Turbulence on the Decay of a Trailing Vortex Wake," *Journal of Aircraft,* Vol. 29, No.2, March - April, 1992, pp. 255 - 263.

78. ITTC, 2008, “Uncertainty Analysis,” Particle Image Velocimetry.

Appendix-A (Details of motor and amplifier)

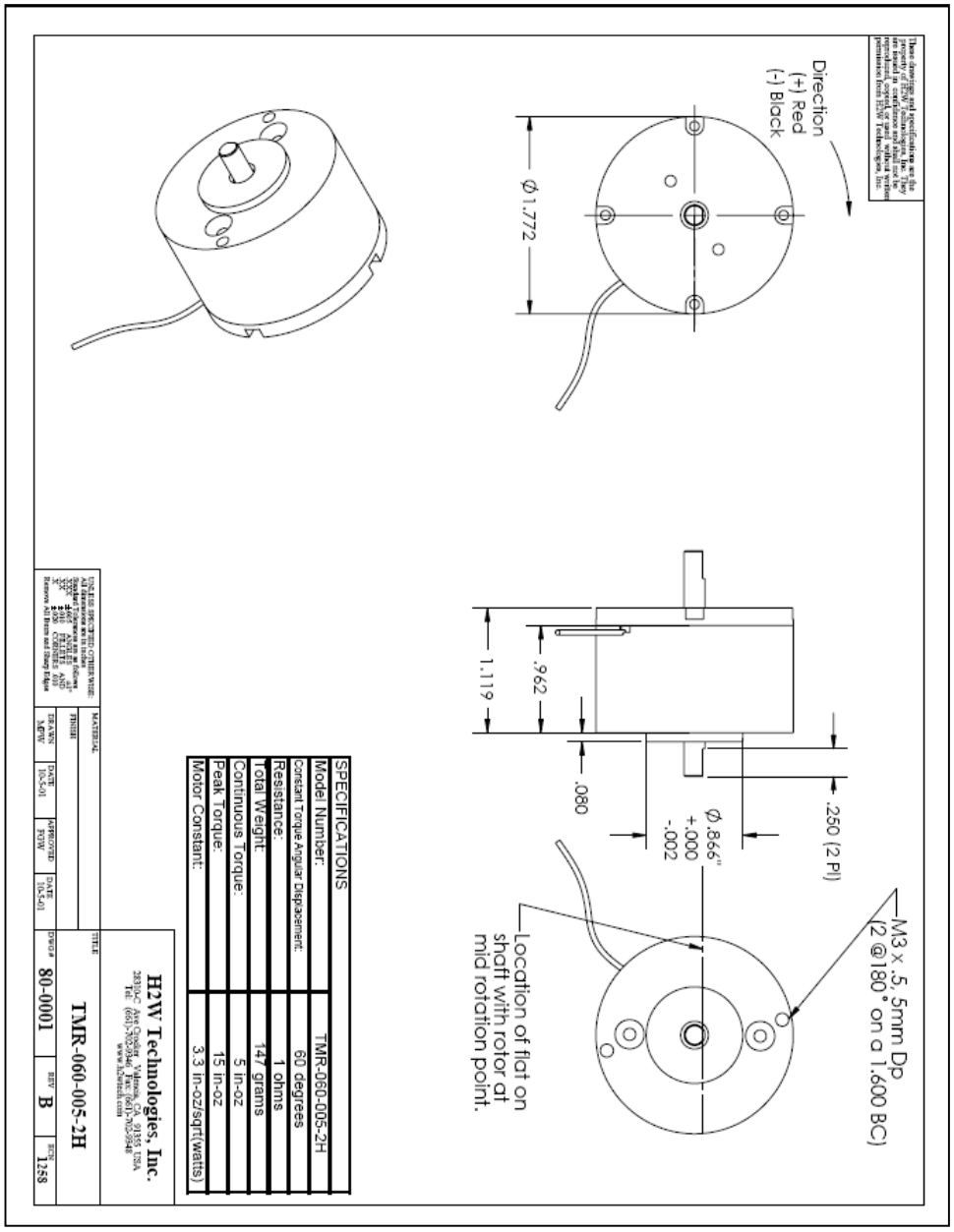

Figure A.1: Motor Specifications purchased from H2W technologies

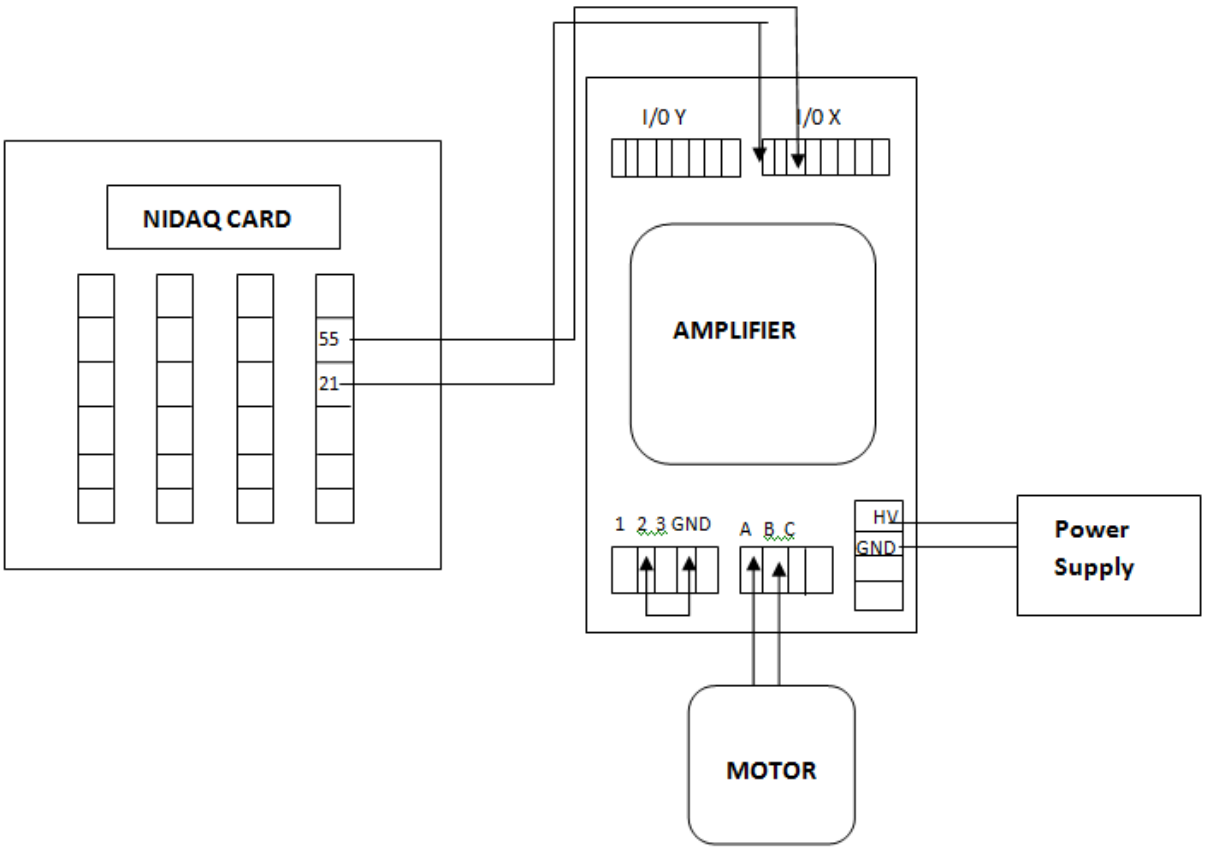

Figure A.2: Detailed wiring of Amplifier and motor

Appendix-B (Results for SVS)

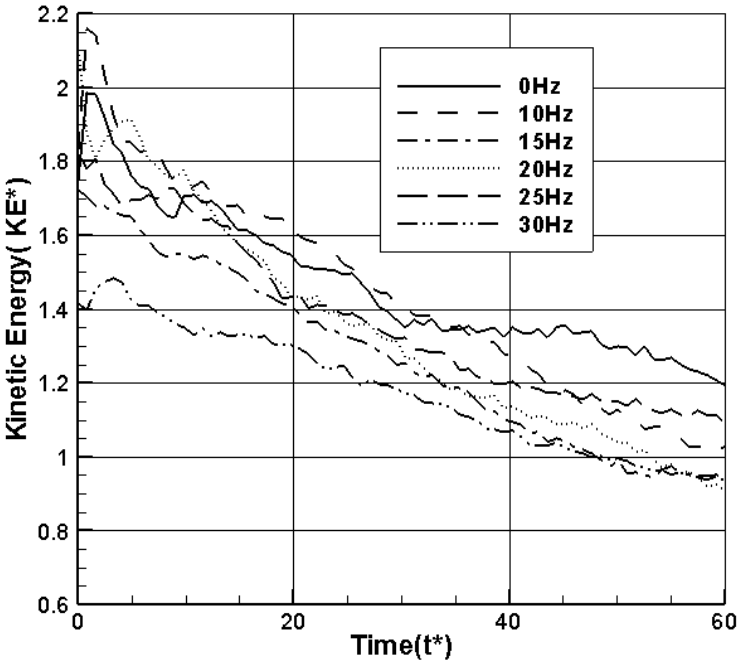

Figure-B.1: Variation of KE with time ($Re_c = 14,000$, A = 0.24 cm)

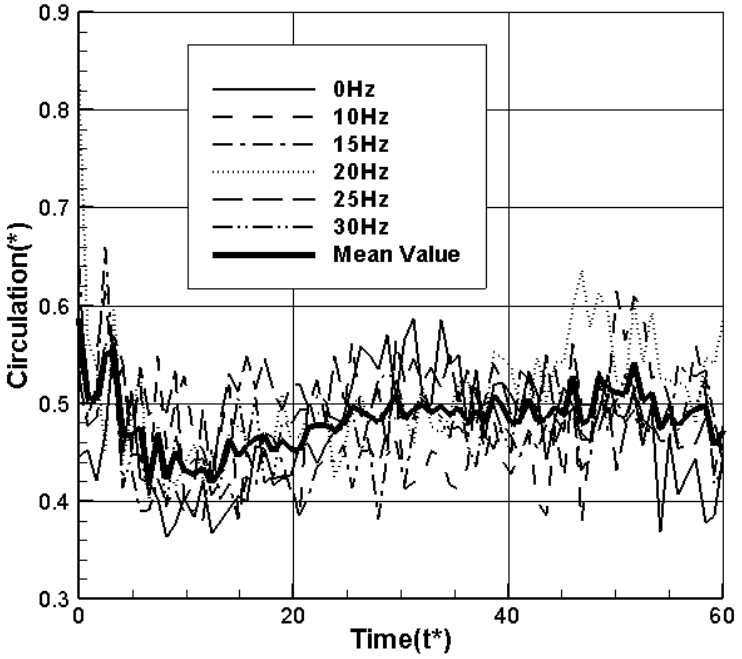

Figure-B.2: Variation of circulation with time (($Re_c = 14,000$, A = 0.24 cm)

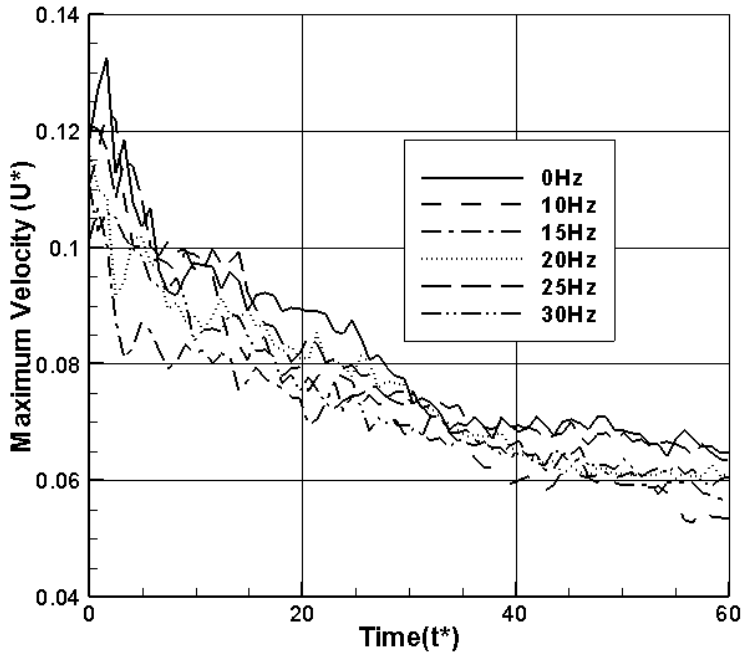

Figure-B.3: Variation of maximum velocity with time ($Re_c = 14,000$, A = 0.24 cm)

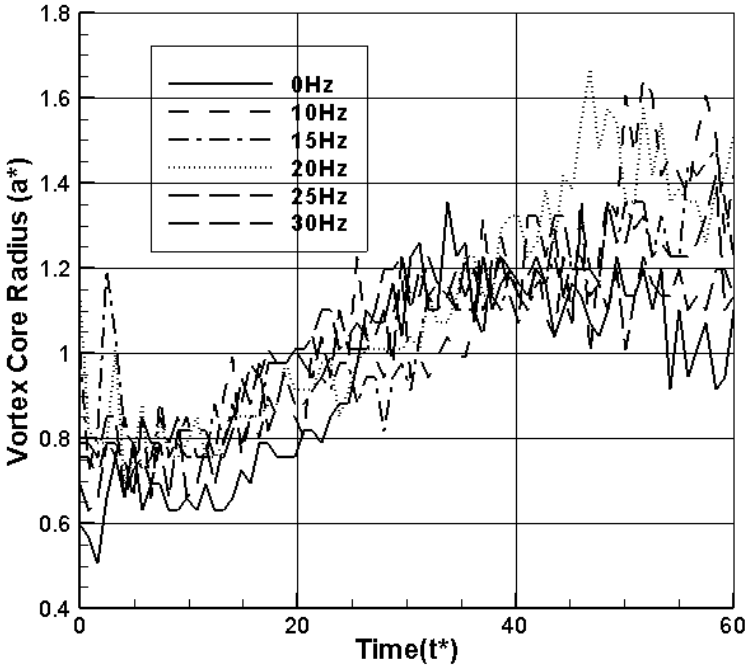

Figure-B.4: Variation of vortex core radius with time ($Re_c = 14,000$, A = 0.24 cm)

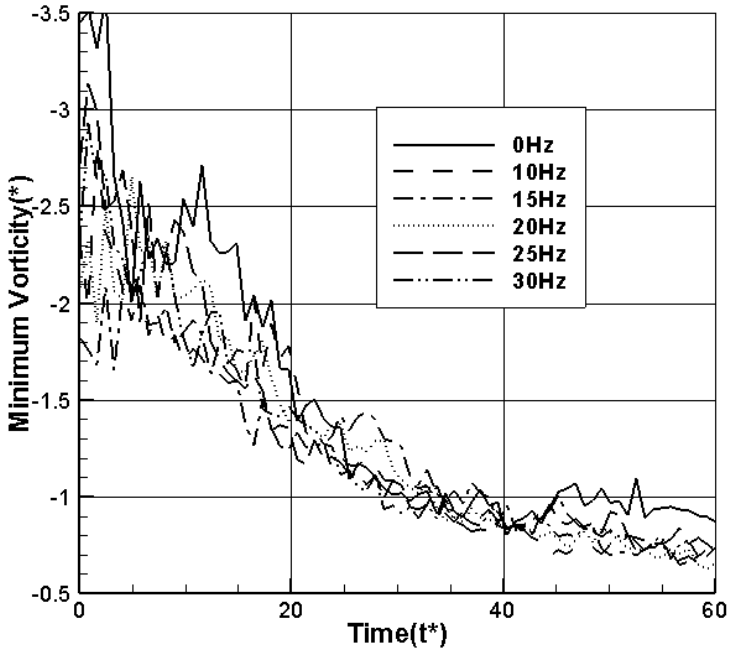

Figure-B.5: Variation of vorticity with time ($Re_c = 14,000$, A = 0.24 cm)

Table-B.1: Average vortex parameters values ($Re_c = 14,000$, A = 0.24 cm)

	Single vortex system(SVS)				
Frequency(Hz)	**Max Velocity**	**Minimum Vorticity**	**Radius of Core**	**Circulation**	**Kinetic Energy**
0	0.082	-1.483	0.951	0.468	1.463
10	0.074	-1.236	1.074	0.478	1.435
15	0.071	-1.219	1.054	0.46	1.259
20	0.076	-1.277	1.114	0.51	1.335
25	0.08	-1.306	1.026	0.5	1.364
30	0.074	-1.268	1.067	0.48	1.174

Appendix-C (Results for CRVS)

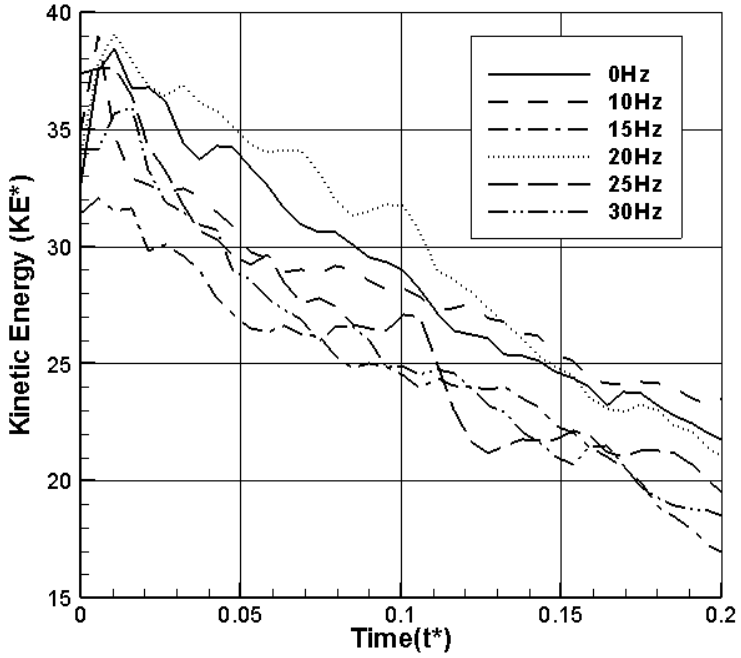

Figure-C.1: Variation of kinetic energy with time ($Re_c = 14,000$, A = 0.24 cm)

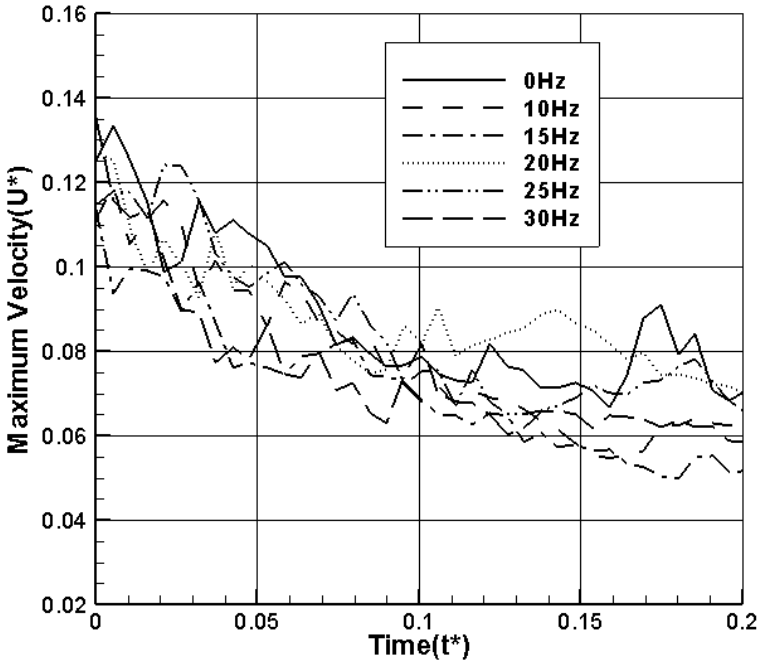

Figure-C.2: Variation of maximum velocity of left vortex with time

($Re_c = 14,000$, A = 0.24 cm)

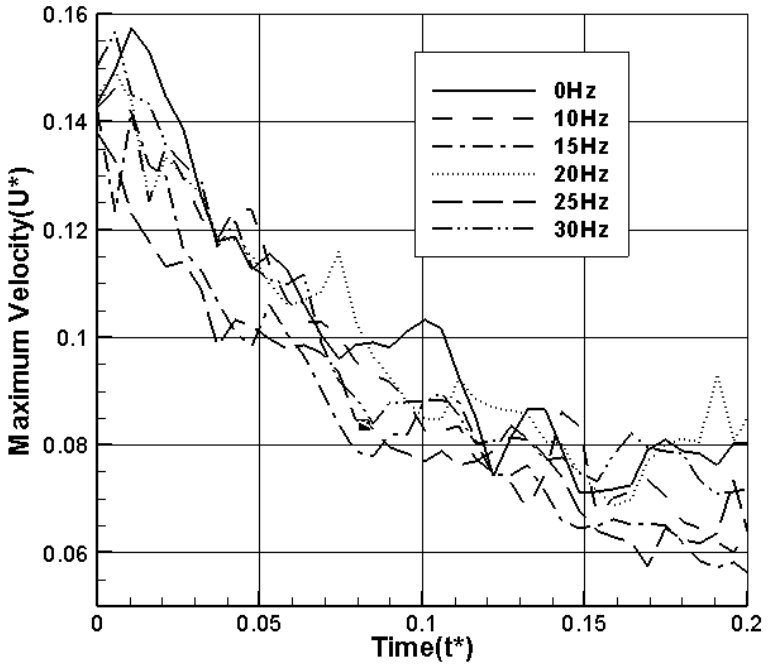

Figure-C.3: Variation of maximum velocity of right vortex with time

(Re_c = 14,000, A = 0.24 cm)

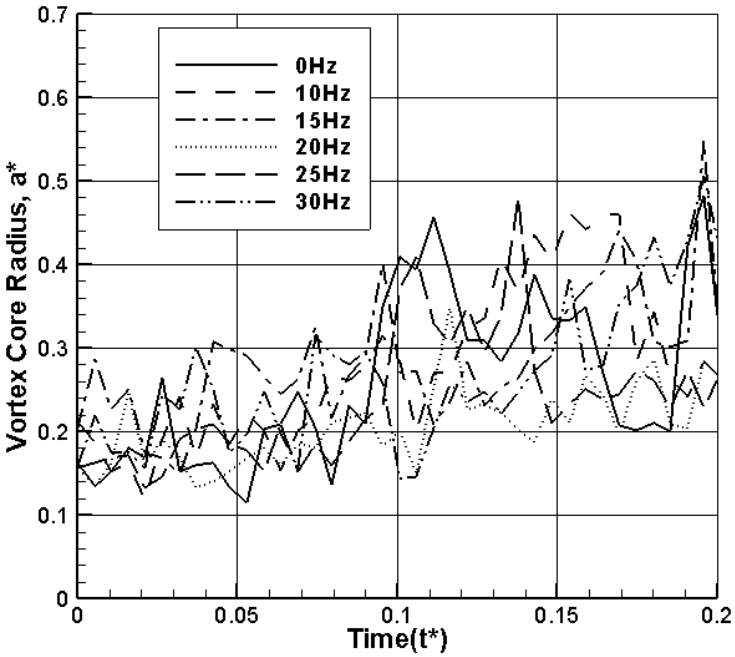

Figure-C.4: Variation of vortex core radius of left vortex with time

(Re_c = 14,000, A = 0.24 cm)

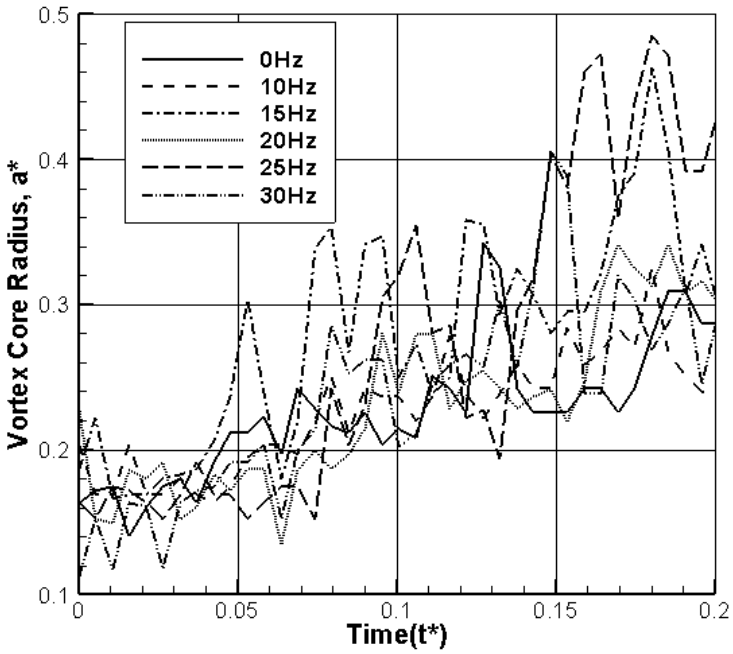

Figure-C.5: Variation of vortex core radius of right vortex with time

($Re_c = 14,000$, A = 0.24 cm)

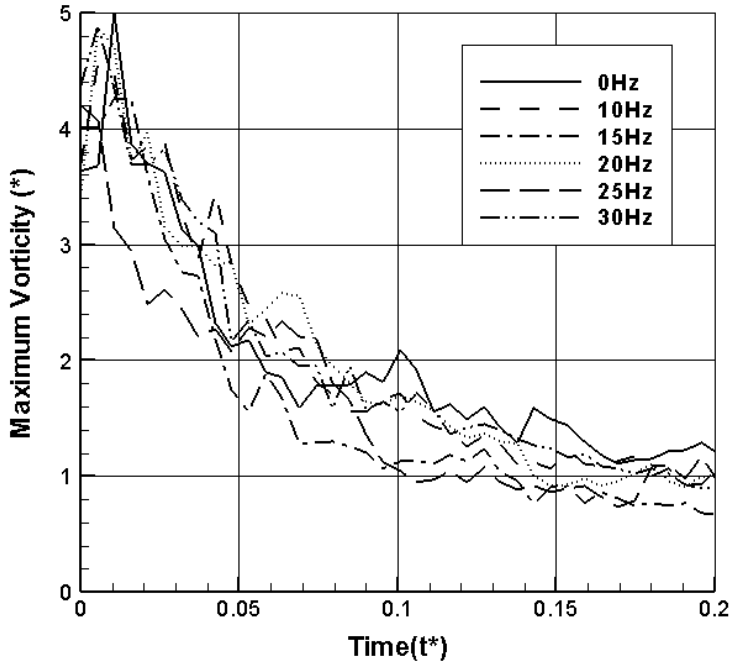

Figure-C.6: Variation of maximum vorticity of right vortex with time

($Re_c = 14,000$, A = 0.24 cm)

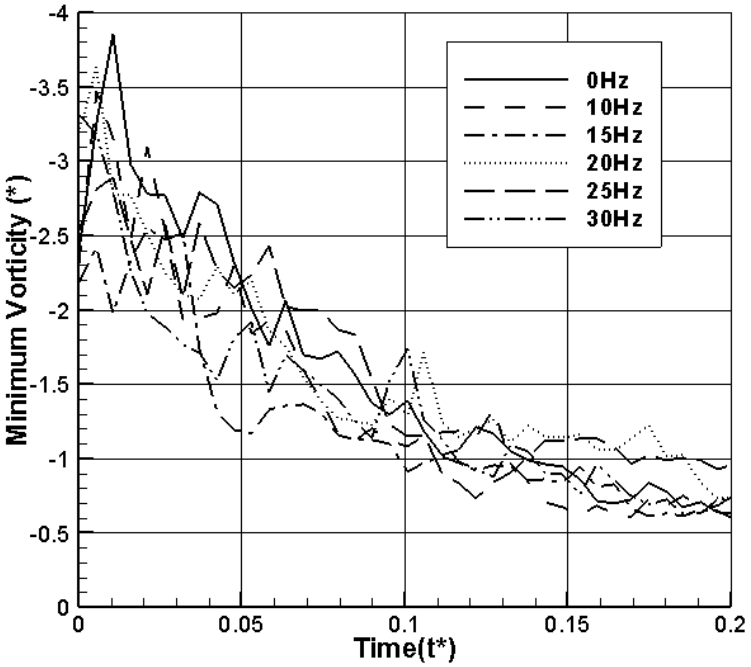

Figure-C.7: Variation of minimum vorticity of left vortex with time

(Re_c = 14,000, A = 0.24 cm)

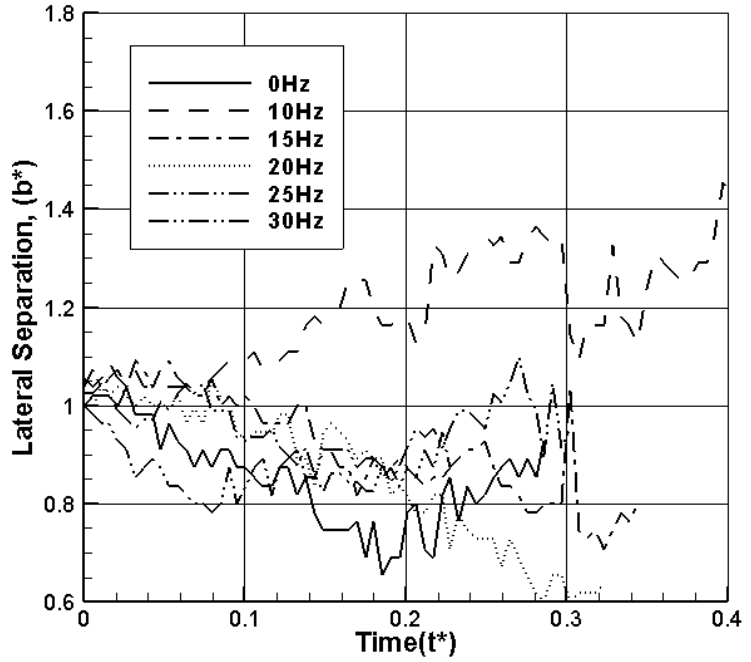

Figure-C.8: Variation of lateral separation with time

(Re_c = 14,000, A = 0.24 cm)

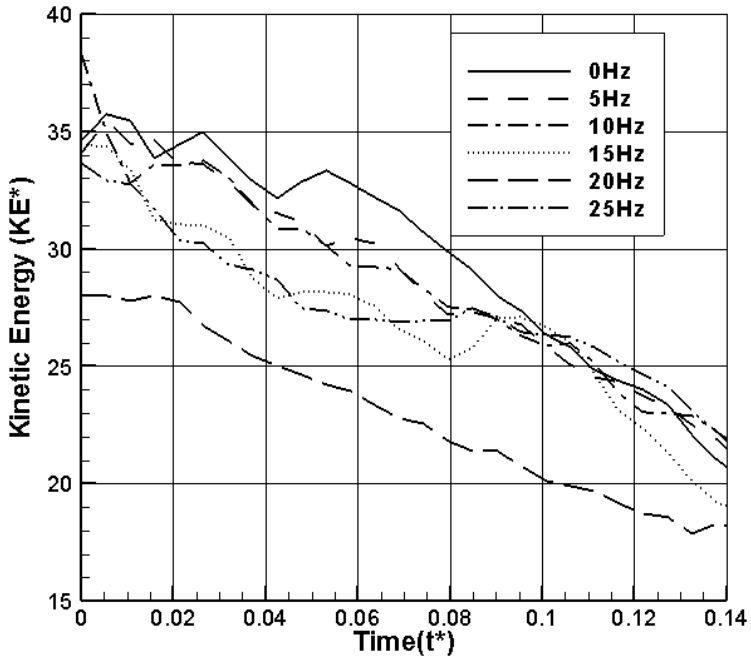

Figure-C.9: Variation of KE with time

(Re_c = 25,000, A = 0.12 cm)

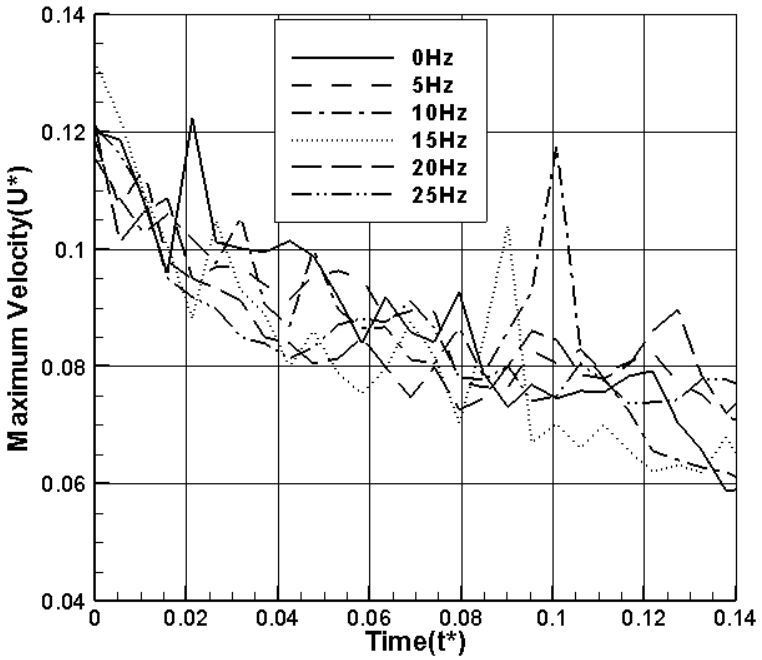

Figure-C.10: Variation of maximum velocity of left vortex with time

(Re_c = 25,000, A = 0.12 cm)

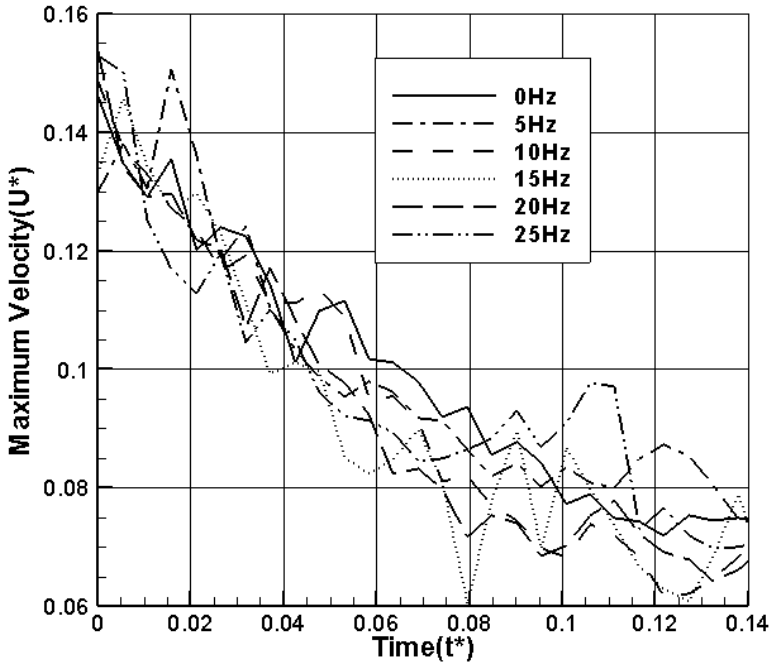

Figure-C.11: Variation of maximum velocity of right vortex with time

(Re_c = 25,000, A = 0.12 cm)

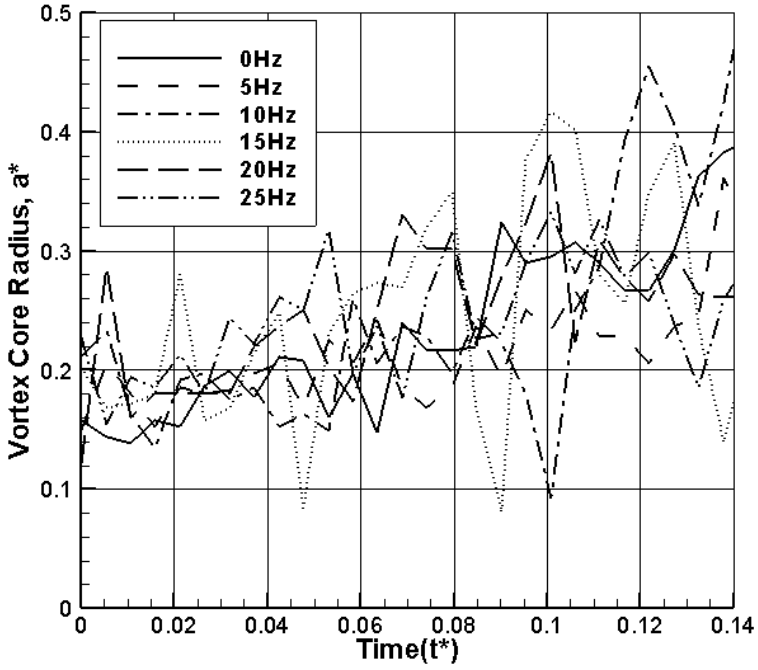

Figure-C.12: Variation of vortex core radius of left vortex with time

(Re_c = 25,000, A = 0.12 cm)

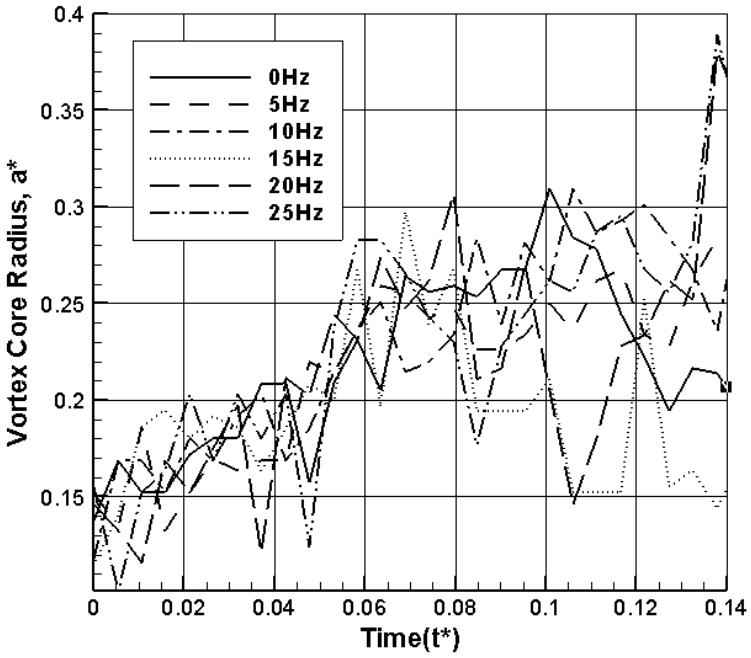

Figure-C.13: Variation of vortex core radius of right vortex with time

(Re_c = 25,000, A = 0.12 cm)

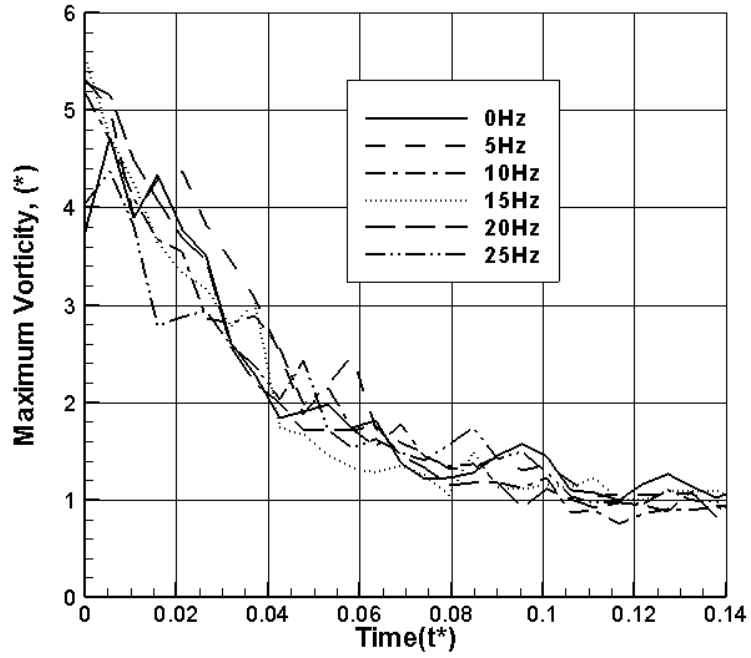

Figure-C.14: Variation of maximum vorticity of right vortex with time

(Re_c = 25,000, A = 0.12 cm)

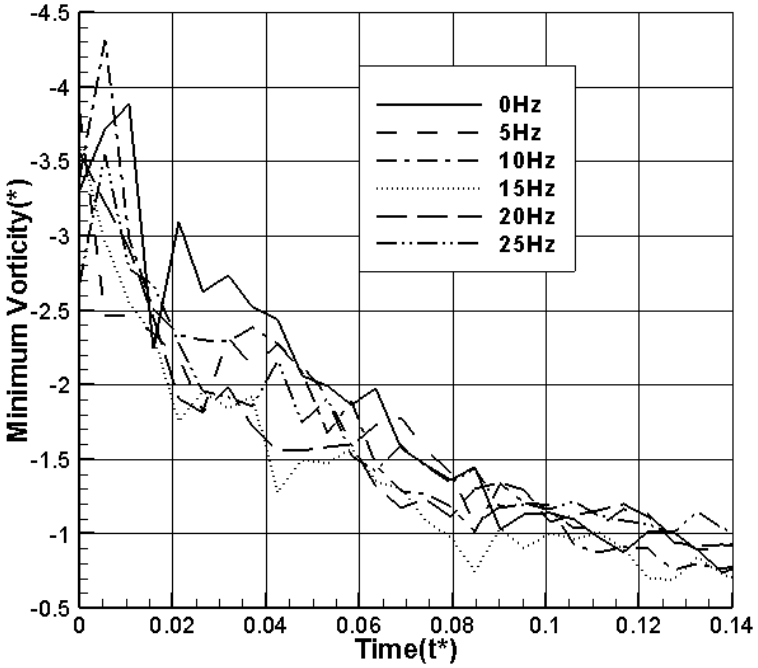

Figure-C.15: Variation of minimum vorticity of left vortex with time

(Re_c = 25,000, A = 0.12 cm)

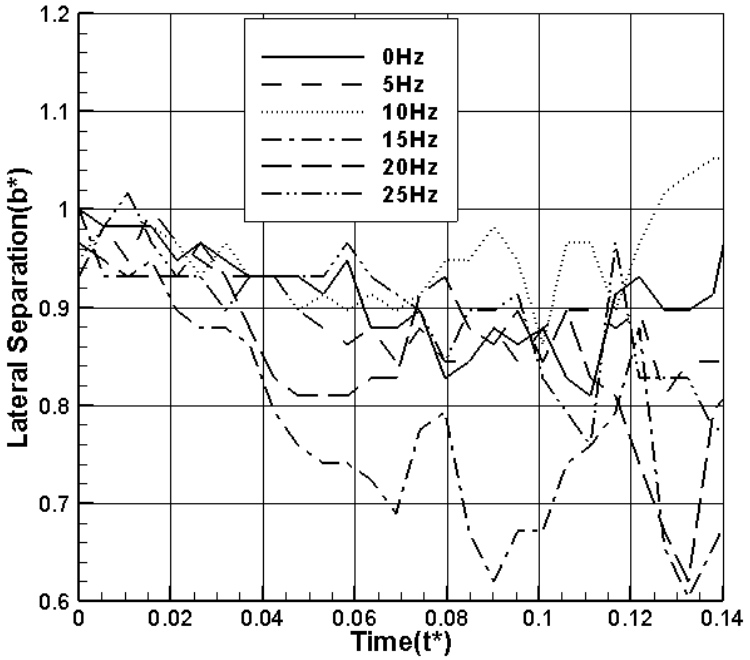

Figure-C.16: Variation of lateral separation with time

(Re_c = 25,000, A = 0.12 cm)

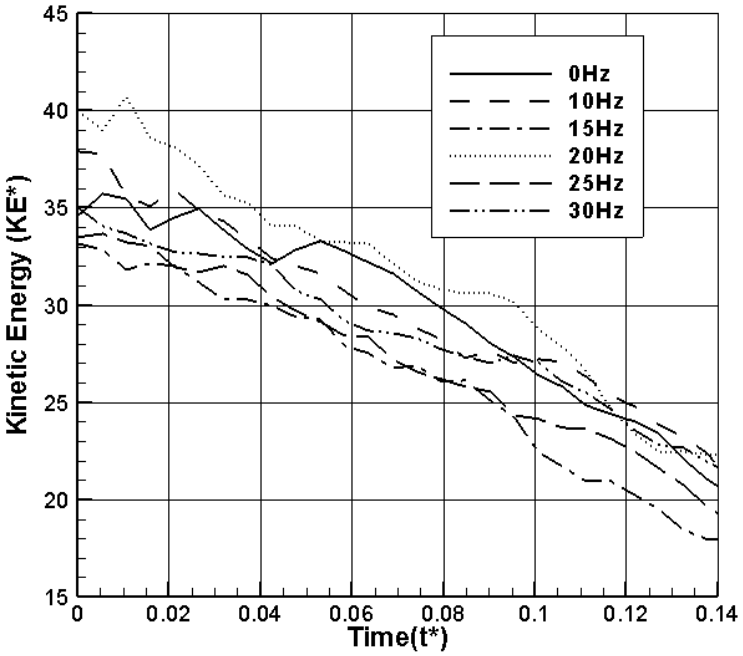

Figure-C.17: Variation of KE with time ($Re_c = 25,000$, A = 0.24 cm)

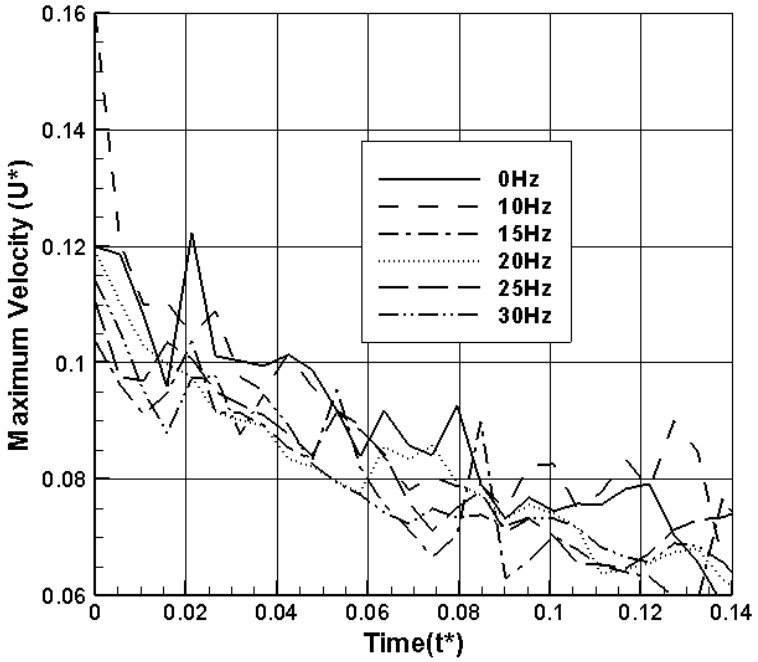

Figure-C.18: Variation of maximum velocity of left vortex with time

($Re_c = 25,000$, A = 0.24 cm)

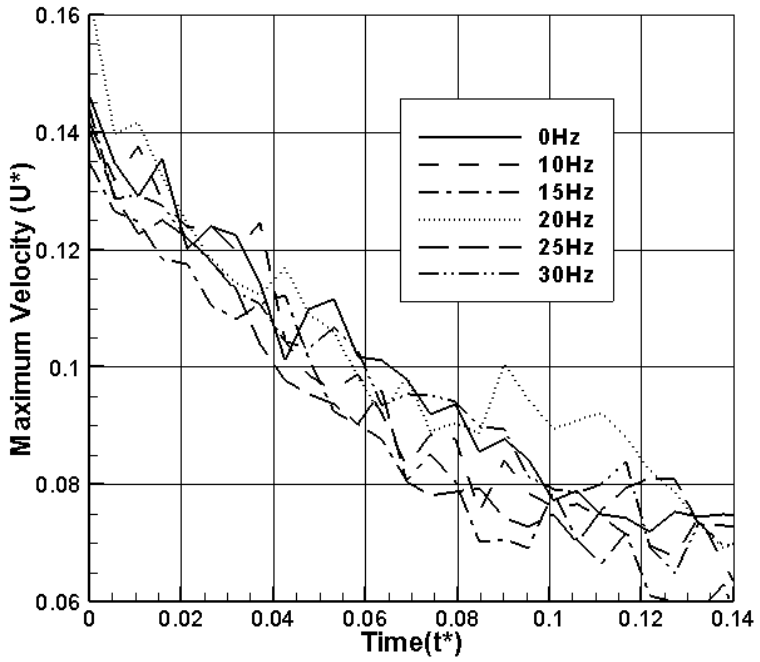

Figure-C.19: Variation of maximum velocity of right vortex with time

(Re_c = 25,000, A = 0.24 cm)

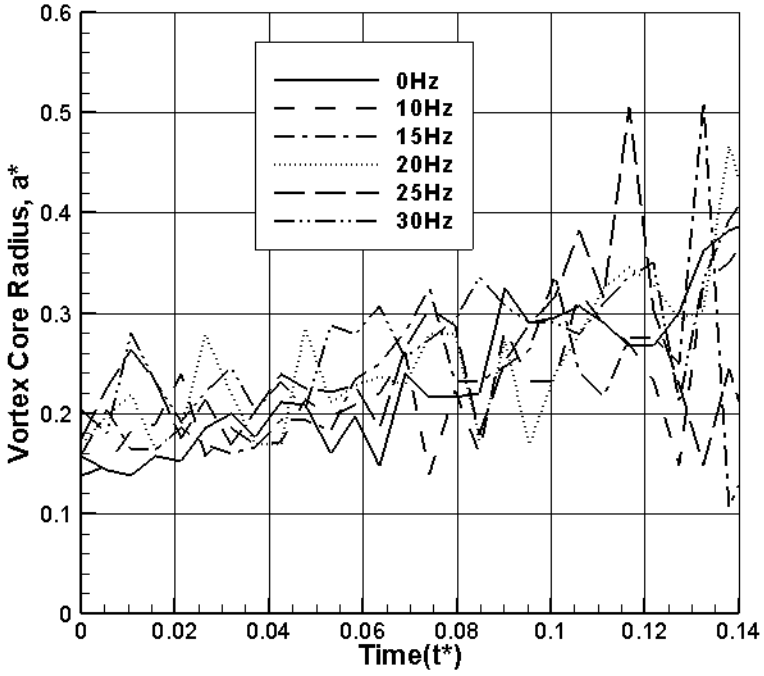

Figure-C.20: Variation of vortex core radius of left vortex with time

(Re_c = 25,000, A = 0.24 cm)

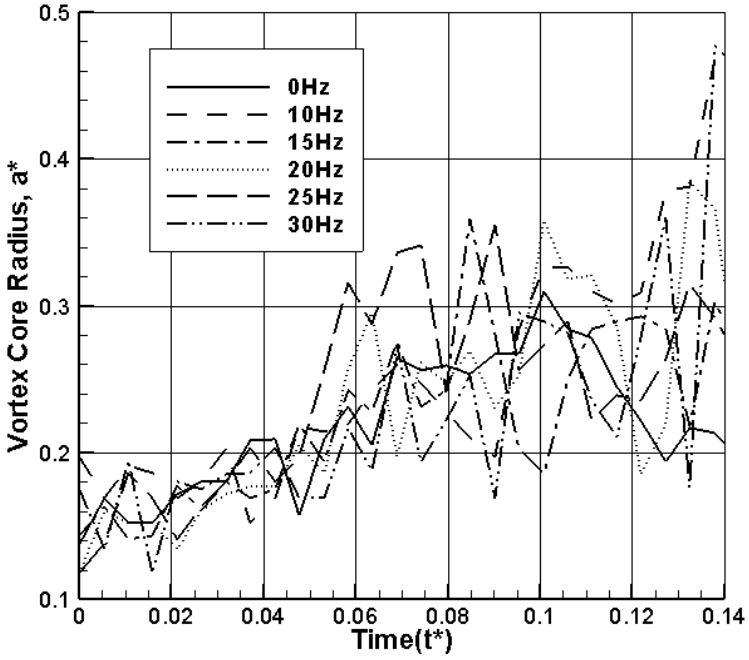

Figure-C.21: Variation of vortex core radius of right vortex with time

(Re_c = 25,000, A = 0.24 cm)

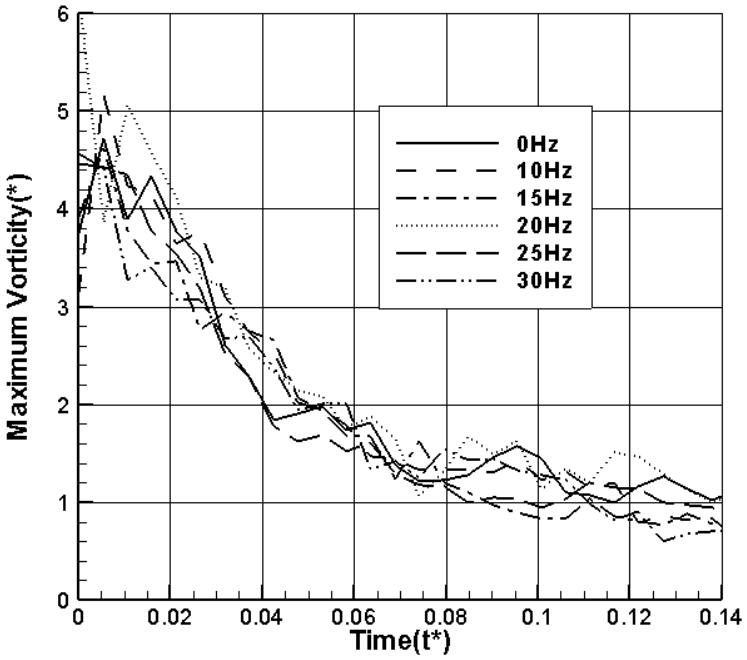

Figure-C.22: Variation of maximum vorticity of right vortex with time

(Re_c = 25,000, A = 0.24 cm)

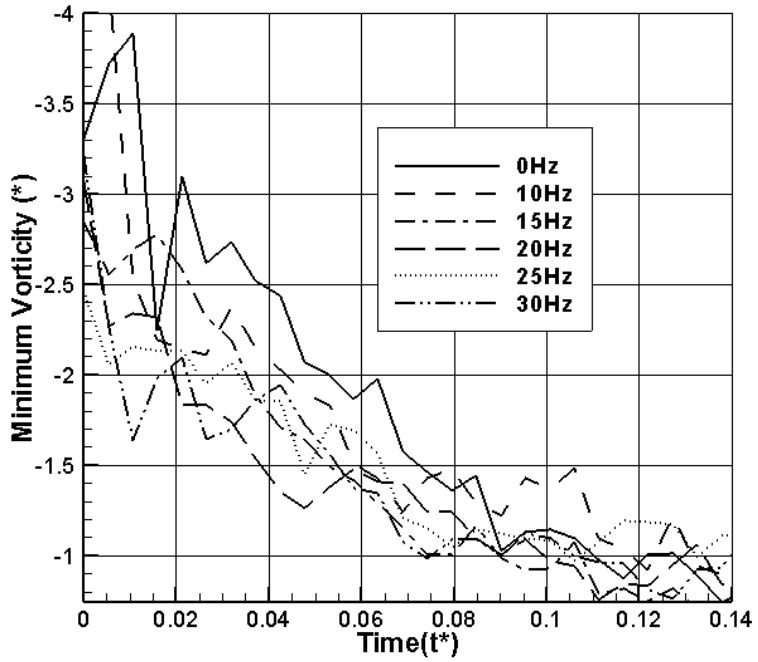

Figure-C.23: Variation of minimum vorticity of left vortex with time

(Re_c = 25,000, A = 0.24 cm)

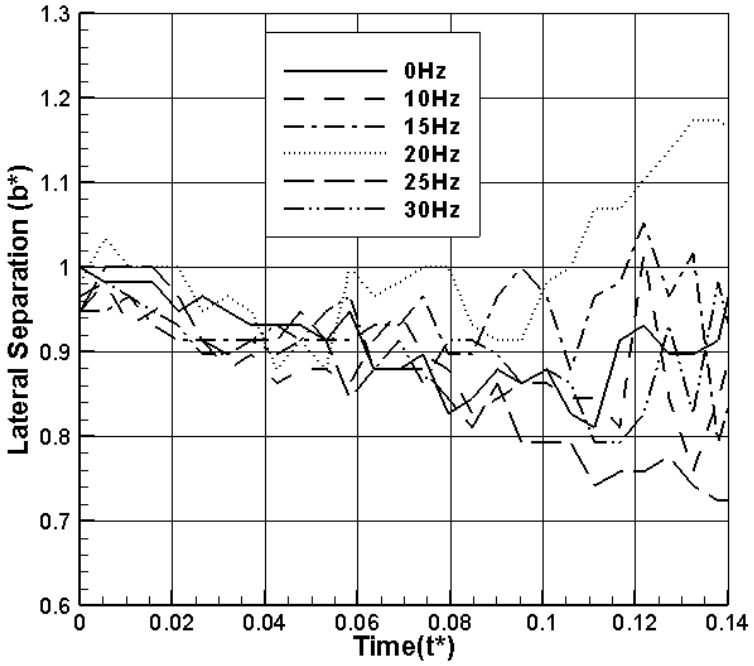

Figure-C.24 Variation of lateral separation with time

(Re_c = 25,000, A = 0.24 cm)

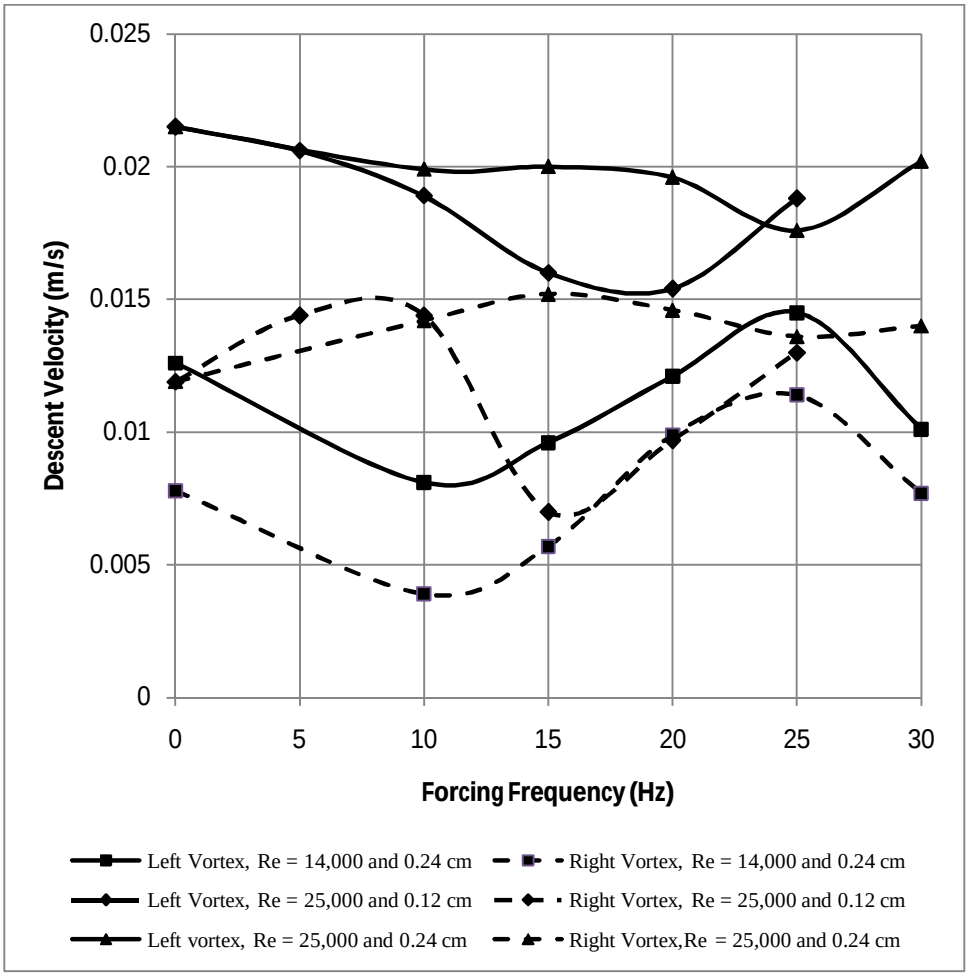

Figure-C.25: Descent rates versus forcing frequencies

Table C.1 Descent rates of vortices for various conditions

Amplitude	Frequency	Descent velocity of perturbed wing	Descent velocity of unperturbed wing
Re_c = 14,000	0Hz	0.0136	0.0081
0.12cm	5Hz	0.0097	0.0061
	15Hz	0.0029	0.0039
	20Hz	0.0046	0.0039
	25Hz	0.0082	0.0056
0.24 cm	10Hz	0.0081	0.0039
	15Hz	0.0096	0.0057
	20Hz	0.0121	0.0099
	25Hz	0.0145	0.0114
	30Hz	0.0101	0.0077
Re_c = 25,000	0Hz	0.0215	0.0119
0.12 cm	5Hz	0.0206	0.0144
	10Hz	0.0189	0.0144
	15Hz	0.016	0.007
	20Hz	0.0154	0.0097
	25Hz	0.0188	0.013
0.24 cm	10Hz	0.0199	0.0142
	15Hz	0.02	0.0152
	20Hz	0.0196	0.0146
	25Hz	0.0176	0.0136
	30Hz	0.0202	0.014

Appendix-D (Hot-Film Measurements for SVS case)

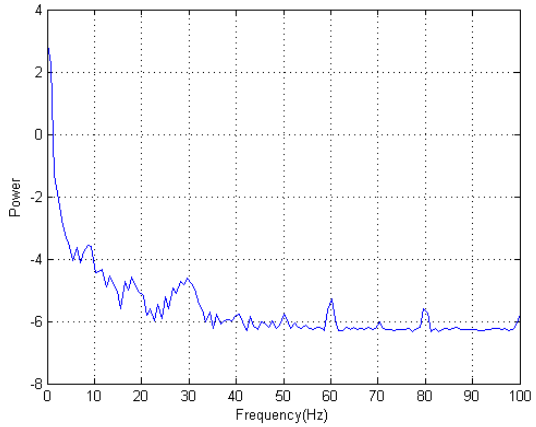

Figure-D.1: PSD plot for 10Hz forcing frequency ($Re_c = 14,000$, A = 0.24 cm)

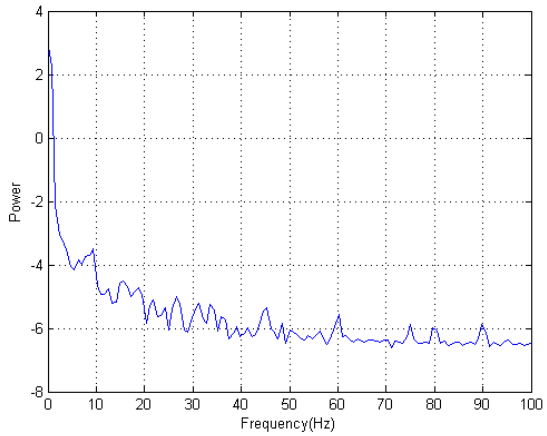

Figure-D.2: PSD plot for 15Hz forcing frequency ($Re_c = 14,000$, A = 0.24 cm)

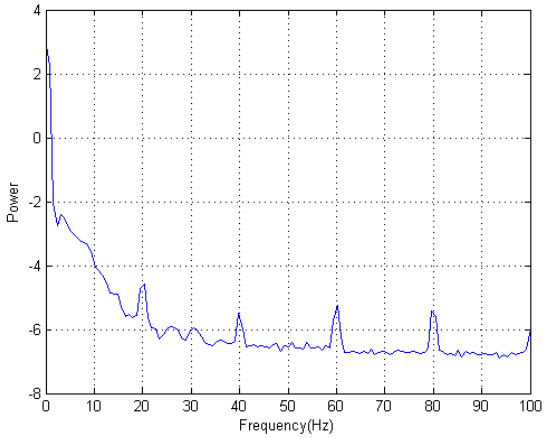

Figure-D.3: PSD plot for 20Hz forcing frequency ($Re_c = 14,000$, A = 0.24 cm)

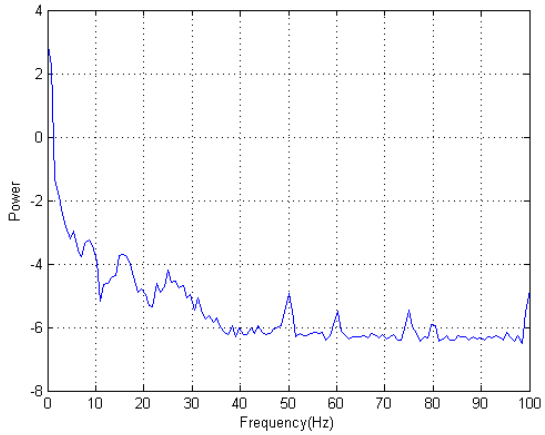

Figure-D.4: PSD plot for 25Hz forcing frequency ($Re_c = 14,000$, A = 0.24 cm)

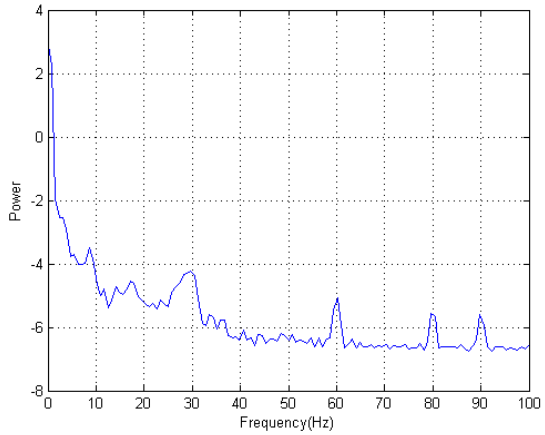

Figure-D.5: PSD plot for 30 Hz forcing frequency ($Re_c = 14,000$, A = 0.24 cm)

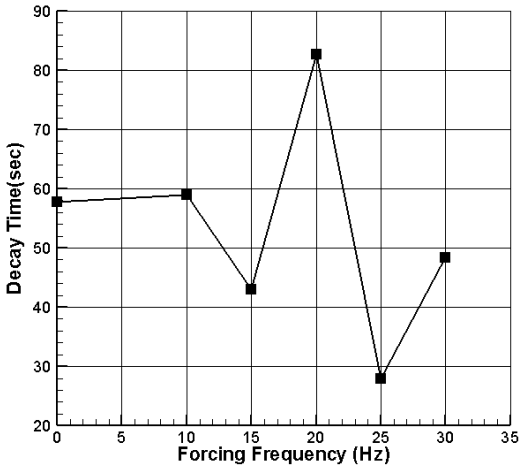

Figure-D.6: Time to decay for different forcing frequencies ($Re_c = 14,000$, A = 0.24 cm)

Appendix-E (Hot-Film Measurements for CRVS)

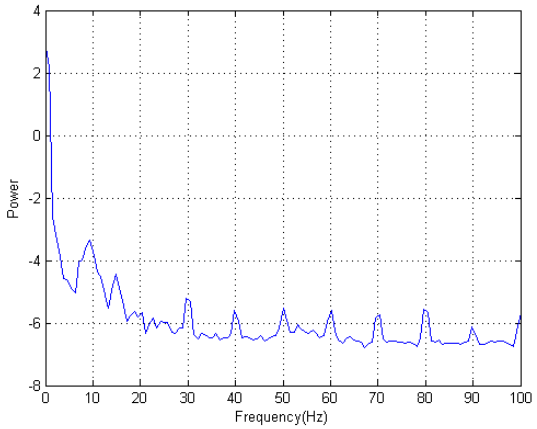

Figure-E.1: PSD plot for 10 Hz forcing frequency ($Re_c = 14,000$, A = 0.24 cm)

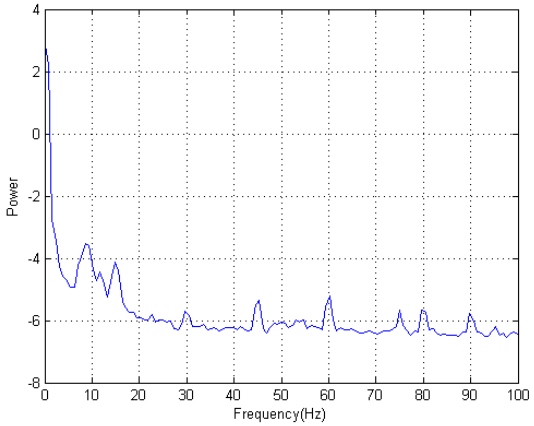

Figure-E.2: PSD plot for 15 Hz forcing frequency ($Re_c = 14,000$, A = 0.24 cm)

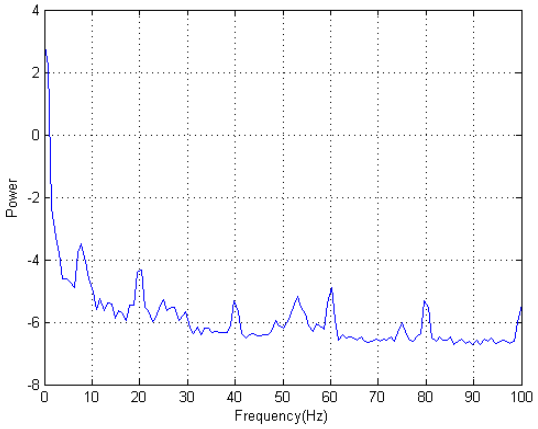

Figure-E.3: PSD plot for 20 Hz forcing frequency ($Re_c = 14,000$, A = 0.24 cm)

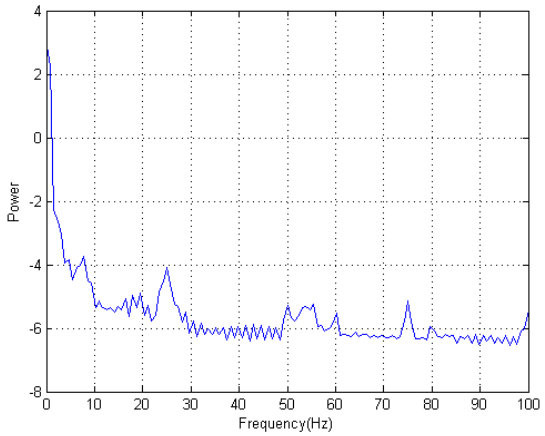

Figure-E.4: PSD plot for 25 Hz forcing frequency ($Re_c = 14,000$, A = 0.24 cm)

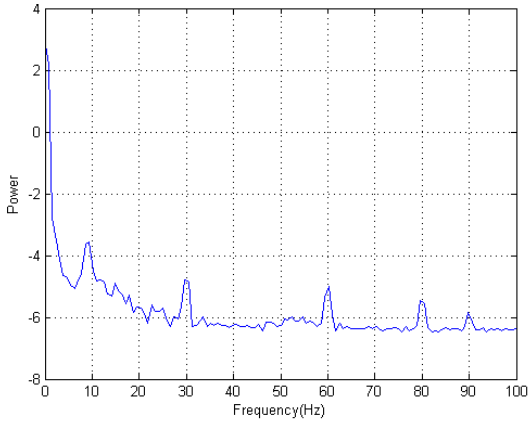

Figure-E.5: PSD plot for 30 Hz forcing frequency ($Re_c = 14,000$, A = 0.24 cm)

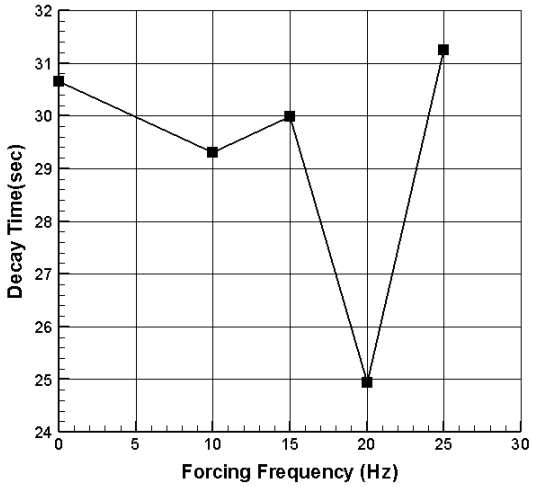

Figure-E.6: Decay time for different forcing frequencies ($Re_c = 14,000$, A = 0.24 cm)

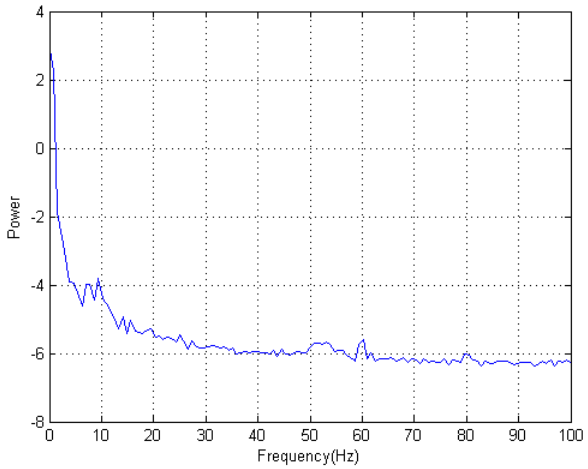

Figure-E.7: PSD plot for No-forcing case ($Re_c = 25,000$)

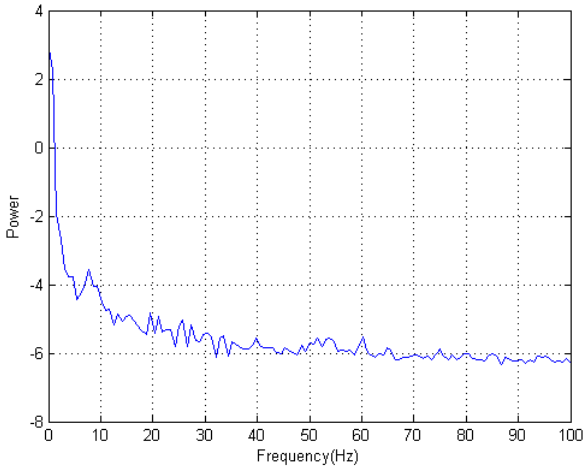

Figure-E.8: PSD plot for 5 Hz forcing frequency ($Re_c = 25,000$, A = 0.12 cm)

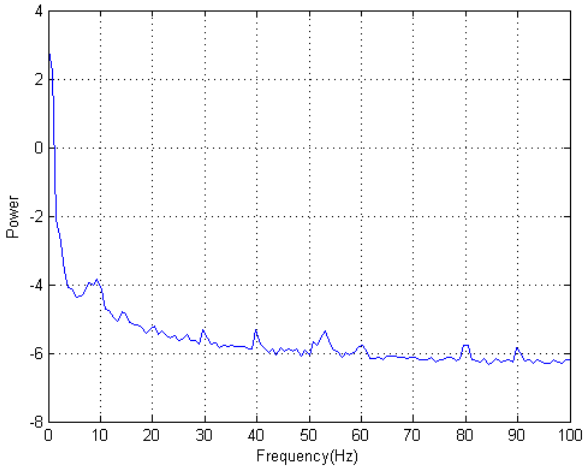

Figure:-E.9 PSD plot for 10Hz forcing frequency ($Re_c = 25,000$, A = 0.12 cm)

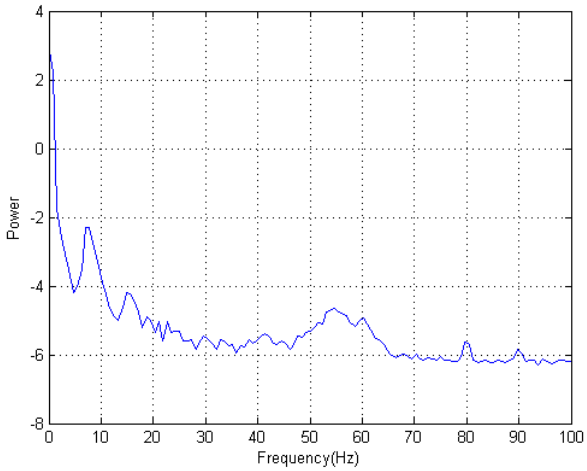

Figure-E.10: PSD plot for 15 Hz forcing frequency ($Re_c = 25,000$, A = 0.12 cm)

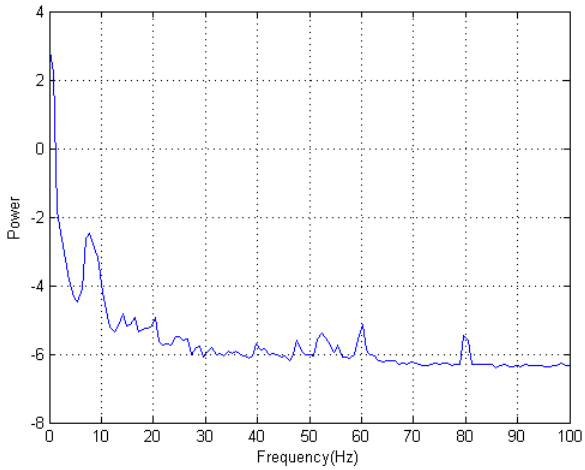

Figure-E.11: PSD plot for 20 Hz forcing frequency ($Re_c = 25,000$, A = 0.12 cm)

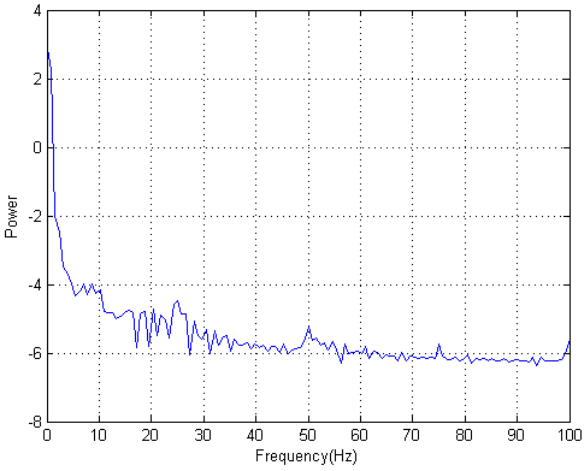

Figure-E.12: PSD plot for 25 Hz forcing frequency ($Re_c = 25,000$, A = 0.12 cm)

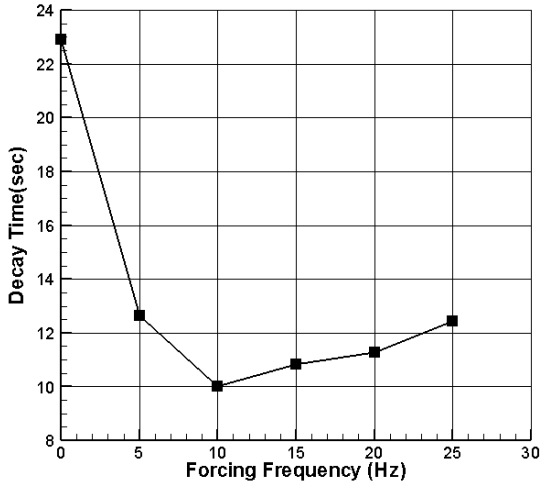

Figure-E.13: Decay time for different forcing frequencies ($Re_c = 25,000$, A = 0.12 cm)

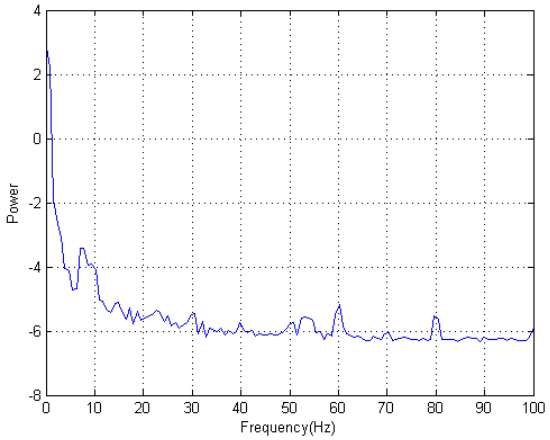

Figure-E.14: PSD plot for 10 Hz forcing frequency ($Re_c = 25,000$, A= 0.24 cm)

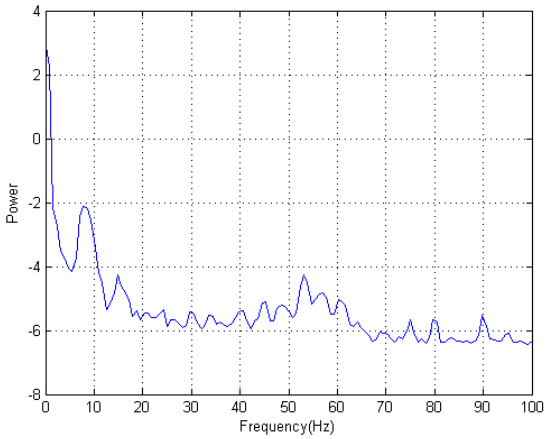

Figure-E.15: PSD plot for 15 Hz forcing frequency ($Re_c = 25,000$, A = 0.24 cm)

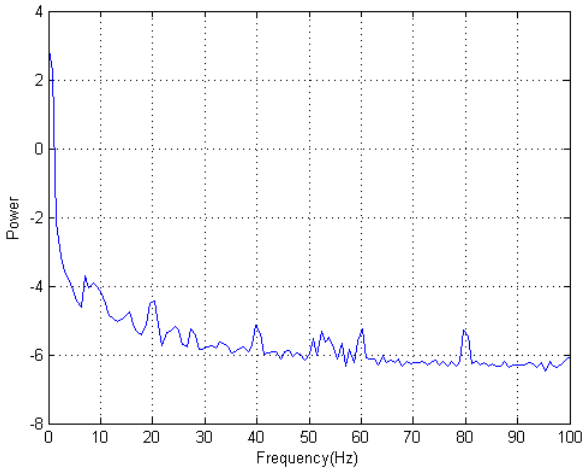

Figure-E.16: PSD plot for 20 Hz forcing frequency ($Re_c = 25,000$, A = 0.24 cm)

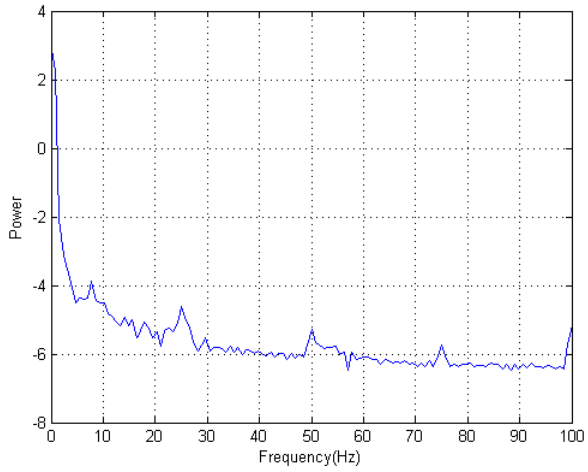

Figure-E.17: PSD plot for 25 Hz forcing frequency ($Re_c = 25,000$, A = 0.24 cm)

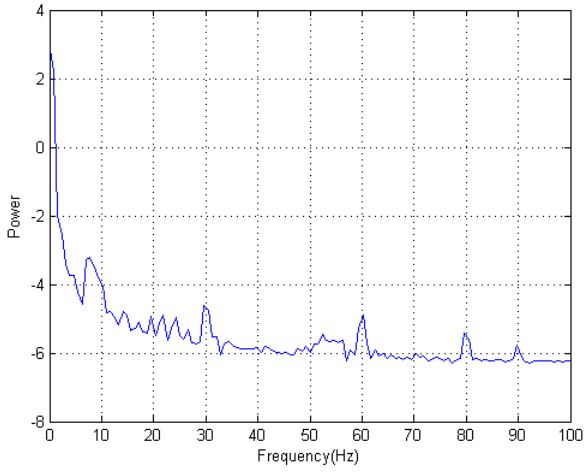

Figure-E.18: PSD plot for 30 Hz forcing frequency ($Re_c = 25,000$, A= 0.24 cm)

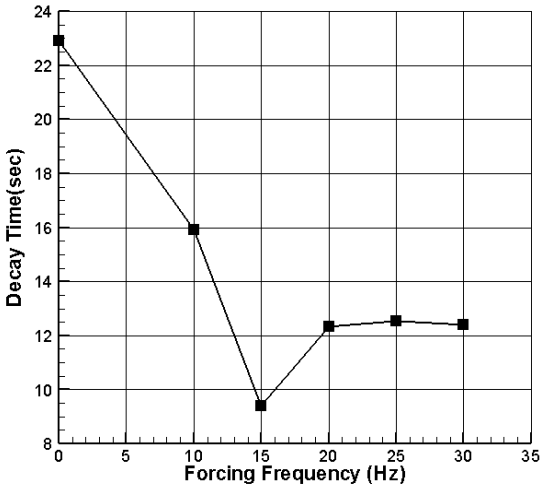

Figure-E.19: Decay time for different forcing frequencies ($Re_c = 25,000$, A = 0.24 cm)

Appendix-F (Uncertainty analysis of PIV Measurements)

The purpose of this procedure was to describe the method for uncertainty analysis on flow field measurement by means of particle image velocimetry (PIV). The PIV system consists of several subsystems and evaluation of measurement needs to consider the coupling between the sub systems. The current procedure was based on guideline of Visualization Society of Japan [78] (VSJ) recommendation. The reference case selected for the uncertainty evaluation was that of Reynolds number of 14,000 which corresponds to 0.24 m/sec.

F.1 General Theory

The PIV system detects the velocity of the particle by measuring the displacement of the particle images Δx, and the time of successive images Δt. The magnification factor m need to be identified through calibration and it gives the physical amount of flow speed. The PIV measurement based on the visualized flow image, and the information of the image differs from the flow field because of the velocity lag of the tracer particles from acceleration and the projection procedure of 3D physical space to 2D image plane. These uncertainty factors of flow visualization were consolidated in a parameter δu. The principle of the PIV measurement on flow speed u can be described by Equation (F.1).

$$u = m(\Delta x/\Delta t) + \delta u \tag{F.1}$$

The PIV measurement system detects the displacement of the particle image by means of the correlation of particle pattern in successive particle image. Most commercial PIV systems use cross correlation analysis .The correlation between successive particle images f(X, Y), g(X, Y) is evaluated by the applying fast Fourier Transform (FFT) shown by (F.2) & (F.3),

$$S_{fg}\,(\xi,\eta) = F\hat{}* \{f(X,Y)\}F\{g(X,Y)\} \tag{F.2}$$

$$C_{fg}(X,Y) = \mathcal{F}^{-1}\{S_{fg}(\xi,\eta)\} \tag{F.3}$$

The target position and time are also the objective of measurement. The measurement of point and time were defined by equations (F.4) & (F.5). In equation (F.4), X_0 is the location of the origin of the image plane, and X_s ,X_e show the starting and ending position of correlation area. The physical location can be obtained by transferring it with magnification factor m. The location X_s and X_e are generally defined by the center locations of the correlation area. The measurement time is defined by the mean value of the pulse time of the laser light sheet as shown by the equation (F.5), where t_s and t_e show the first and second pulse time. All the measurement parameters u, x, t were the objectives of the uncertainty analysis, and they were analyzed independently in the procedure.

$$x = m[(X_s + X_e)/2 - X_0 \tag{F.4}$$

$$t = (t_s + t_e)/2 \tag{F.5}$$

The calibration was conducted by insertion of a calibration board at the same position as the laser light sheet. The distance of the image reference point l_r and its distance on the image plane L_r were used to determine the magnification factor, m, as

$$m = l_r \cos\theta / L_r \approx l_r(1 - \frac{\theta^2}{2}) / L_r \tag{F.6}$$

Table F.1: Principal dimensions of PIV measurement

Target Flow of the Measurement	
Measurement facility	Towing Tank
Measurement area	193.9 x 155.1 mm^2
Uniform flow speed	0.24 m/s and 0.43 m/s
Calibration	
Distance of the reference point(l_r)	5mm
Distance of the reference image(L_r)	33.0067 pixels
Magnification factor(m)	0.1515 mm/pixel
Flow Visualization	
Tracer particles	Hollow glass sphere
Average diameter (d_p)	20 μm
Light source	Double Pulsed Nd:YAG laser
Laser power	200 mJ
Thickness of the laser light sheet	2.5-3 mm
Time interval(Δt)	8000 μs and 12000 μs
Image Detection	
Camera	
Spatial resolution	1280 x 1024 pixels
Sampling frequency	4.5Hz
Gray resolution scale	8 bit
Pixel pitch	9 μm x 9 μm
Optical system	
Distance from target (l_t)	1014 mm
Length of focus	60 mm
F number of lens	f 5.6
Data Processing	
Pixel unit analysis	Cross correlation method
Correlation area size	32 x 32 pixels
No of refinement steps	16 x 16 pixels

F.2 Error sources and propagation of errors:

F.2.1 Calibration board:

Image distance of reference points: L_r

The distance of the reference points were measured from the image plane. If the positions of the reference points were detected from single point of image, the uncertainty band will be 0.5 pixels, and the total amount of the uncertainty band will be 0.7 pixels. The sensitivity factor for m was from equation (F.6),

$$\frac{\partial m}{\partial L_r} = -\frac{l_r}{{L_r}^2} = -4.6 \text{ x } 10^{-3} \text{ [mm/}pixel^2\text{]}$$

Physical distance of reference points: l_r

The uncertainties of the physical length of the reference points affect the accuracy of the magnification factor (m).The well-controlled calibration board has the less than a 20 μm error. The sensitivity factor of it was from equation (F.6).

$$\frac{\partial m}{\partial L_r} = -\frac{1}{L_r} = 3.03 \text{ x } 10^{-2} \text{ [1/pixel]}$$

F.2.2 Optical system:

Image distortion:

The image could be distorted by the aberration of lenses. The distortion of image affects the error of magnification factor. The distortion of the image will be less than 0.5 % of the total length, and 0.005 L_r = 0.1650 pixel. The sensitivity factor for m was from equation (F.6),

$$\frac{\partial m}{\partial L_r} = -\frac{l_r}{{L_r}^2} = -4.6 \text{ x } 10^{-3} \text{ [mm/}pixel^2\text{]}$$

F.2.3 Experimental condition

Parallel reference board.

Ideally, the calibration board should be in a plane parallel to the laser light sheet for visualization. When the angle between original laser sheet plane and calibration board deviated at most θ_1 = 2° = 0.035 rad from parallel, the sensitivity factor was from Equation (F.6)

$$\frac{\partial m}{\partial \theta} = -l_r . \theta / L_r = \text{-0.0053[mm/pixel]}$$

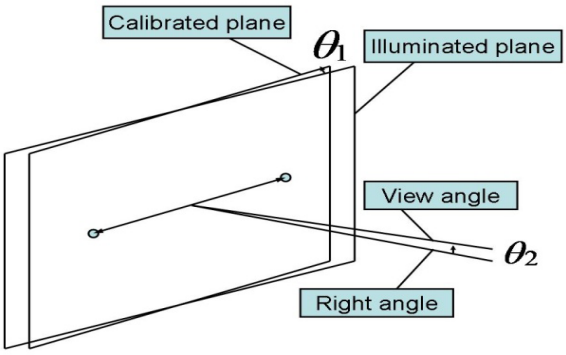

Figure F.1: Angles for the calibration board and view

F.2.4 Displacement of Particle Image: ΔX

F.2.4.1 Image detection:

CCD distortion

The CCD distortion is the same error source with one in the calibration of the optical system, and the amount of error could be 0.0056 pixels. The error may be different cell by cell, and then the error should take into account here again.

Normal view angle

The normal or perpendicular view angle to the illumination plane could affect the uncertainty of the displacement. The angle could be estimated as θ_2= 2°, and the sensitivity factor was $\frac{\partial m}{\partial \theta} = -l_r . \theta / L_r$ = -0.0053[mm/pixel].

F.2.4.2 Data processing:

Mis-matching error

In the pixel unit analysis, mis-matching of pair particle images could happen. Large serious error can be detected by comparing the candidate vector with surrounding ones, but small errors of mis-matching cannot be detected usually. The uncertainty band of the pixel unit analysis could be estimated statistically, and it could be about 0.2 pixels.

F.2.5 Time Interval: (Δt)

Delay generator

The delay generator controls the pulse timing, and the possible fluctuation will be 2 ns, which was obtained from the user manual. The sensitivity factor for the measurement time was 1.

Pulse timing accuracy

The pulse laser itself has an uncertainty for the pulse timing. The uncertainty band for it will be 5 ns, which was obtained from manual. The sensitivity factor for the measurement time was 1.

F.2.6 Experiment: δu.

Three-dimensional effects on perspective of velocity

The perspective of out-of-plane velocity component affects the in-plane measured value. The measured velocity can be described as follows:

$$u_m = u + w \tan\theta \tag{F.7}$$

where w is the normal velocity component. Then $w \cdot \tan\theta$ indicates the error component. The perspective angle θ can be estimated by the distance from the target plane and the size of measurement area. When the out of plane component of velocity is assumed as 1.0% of uniform flow, the error could be estimated as

240 x 0.01x tan (193.9/ (2*1014)) = 0.2302[mm/s]

F.2.7 Measurement position: *x*

Non-uniformity of tracer particle distribution:

The flow speed was identified from the displacement of a particle image. When the particle distribution was not uniform in the correlation area, the centre position of the measured velocity field could be apart from the centre of correlation area. The possibility of the bias was at most one fourth of the correlation area size, and the sensitivity factor from Equation (F.4) was:

$$\frac{\partial x}{\partial X} = \text{m} = 0.1515[\text{mm/pixel}]$$

Magnification factor:

The coordinates of each measurement point are obtained by transferring the image position to physical space by Equation F.4.

F.3 Summary of Uncertainties:

The uncertainties of *u*, *x*, and *t* are analyzed independently. When accumulation for total performance of the measurement system by the uncertainty for the flow speed is needed, the following summation can be applied, where u_u , u_x and u_t represent the uncertainties of *u*, *x*, and *t*, respectively:

$$u_c = \sqrt{{u_u}^2 + \left(u_x \frac{\partial u}{\partial x}\right)^2 + \left(u_t \frac{\partial u}{\partial t}\right)^2} \quad \text{(F.8)}$$

Table F.2 Summary of uncertainties for velocity *u*

Parameter	Category	Error Sources	u(x_i)(unit)	c_i (unit)	c_i u(x_i)	u_c
m(mm/pix)	Calibration	Reference image Physical distance Image distortion by lens Parallel Board	0.70(pix) 0.02(mm) 0.1650(pix) 0.035(rad)	0.0046 0.0303 0.0046 .0053	0.00322 0.000606 0.000759 0.00018	0.00464
ΔX(pix)	Acquisition	Image Distortion by CCD Normal view angle	0.0056(pix) 0.035(rad)	1 0.0053	0.0056 0.0018	0.205
	Reduction	Mis- matching error	0.20(pix)	1	0.20	
Δt	Acquisition	Delay generator Pulse time	2.00E-09 5.00E-09	1 1	2.00E-09 5.00E-09	5.59E-09
δu (mm/s)	Experiment	3-D effects	0.2302	1	0.2302	0.2302

Parameter	Category	Error sources	$u(x_i)$ (unit)	c_i (unit)	$c_i u(x_i)$ (unit)
α		Magnification factor	0.00464	1580 (pix/s)	7.3312
ΔX		Image displacement	0.205	12.625 (mm/ pix/s)	2.588
Δt		Image interval	5.59E-09	6 (mm/s^2)	3.354E-08
δu		Experiment	0.2302	1.0	0.2302
			Combined uncertainty	u_u	10.149 mm/s

Table F.3 Summary of uncertainties for position, *x*, and time, *t*

Parameter	Category	Error sources	$u(x_i)$ (unit)	c_i (unit)	$c_i u(x_i)$ (unit)
*X*s, *X*e	Acquisition	Non-uniformity of distribution	8 (pix)	0.1515(mm/pix)	1.2
α		Magnification factor	0.00178 (mm/pix)	640.0 (pix)	1.139
			Combined uncertainty	u_x	2.35 (mm)

Parameter	Category	Error sources	$u(x_i)$ (unit)	c_i (unit)	$c_i u(x_i)$ (unit)
t_s, t_e	Acquisition	Delay generator Pulse time	2.00E-09(s) 5.00E-09(s)	1.0 1.0	2.00E-09 5.00E-09
			Combined uncertainty	u_t	5.39E-09 (s)

The experimental error in resultant velocity calculated from above mentioned method was 4.2 %. The standard deviation in circulation was 5 %. The total error in vorticity calculated using data reduction method was 4.8 %

Appendix-G (MATLAB PIV CODE)

```
****************** PROGRAM WRITTEN TO STITCH TWO IMAGES TOGETHER AS WELL AS
CALCULATE PARAMETERS OF CRVS  ************************
U_inf = 0.24;
c = 0.0584;
dt = 12000*10^(-6);
 ppi = 1280/193.9;
den = 1000;
mu = 1.004* 10^(-6);        %*******DENSITY IN KG/M3******%
c =0.0584;              %*********** CHORD IN METERS
b = 0.1842;             %********** EFFECTIVE SPAN OF THE WING
AOA = 5;                %*********** AOA IN DEGREES
%********************** READING THE FILES*****************************%
%********************** FOR CAMERA1_B (PROCESSED FILE) AND CAMERA 2_A
for k = 1:100
        if (k<10)
                str = num2str(k,1);
                S_1 = horzcat('0Hz0.24ms_B00',str,'.VEC');
                S_2 = horzcat('0Hz0.24ms_A00',str,'.VEC');
        elseif (k<=99);
                str = num2str(k,2);
                S_1 = horzcat('0Hz0.24ms_B0',str,'.VEC');
                 S_2 = horzcat('0Hz0.24ms_A0',str,'.VEC');
        else
                str = num2str(k,3);
                S_1 = horzcat('0Hz0.24ms_B',str,'.VEC');
                S_2 = horzcat('0Hz0.24ms_A',str,'.VEC');
        End
        fid1 = fopen(S_1,'r');                                  %****** OPENS A FILE TO READ
         fid2 = fopen(S_2,'r');
        if fid1 == -1
                fprintf('CANNOT OPEN FILE FROM CAMERA 1')
                return;
        end
         if fid2 == -1
                fprintf('CANNOT OPEN FILE FROM CAMERA 2')
                return;
        end
        DATA_1 = fscanf(fid1,'%f ,%f ,%f, %f ,%f',[5 inf]);   %******** READS DATA ****
        while isempty(DATA_1)
                fgetl(fid1);
                DATA_1 = fscanf(fid1,'%f,%f ,%f, %f ,%f',[5 inf]);
        end
        DATA_2 = fscanf(fid2,'%f ,%f ,%f, %f ,%f',[5 inf]);             %******** READS
        while isempty(DATA_2)
                fgetl(fid2);                                    %*****   READS DATA WITH
                DATA_2 = fscanf(fid2,'%f,%f ,%f, %f ,%f',[5 inf]);
         end
        y1(:,1) = (DATA_1(1,:));
        z1(:,1) = (DATA_1(2,:));
        u1(:,1) = (DATA_1(3,:));
        v1(:,1) = (DATA_1(4,:));
```

```
        F1(:,1) = (DATA_1(5,:));
        y2(:,1) = (DATA_2(1,:));
        z2(:,1) = (DATA_2(2,:));
        u2(:,1) = (DATA_2(3,:));
        v2(:,1) = (DATA_2(4,:));
        F2(:,1) = (DATA_2(5,:));
        y1(:,1) = y1(:,1).*(1./ppi)*0.001;
        z1(:,1) = z1(:,1).*(1./ppi)*0.001;
        u1(:,1) = u1(:,1).*(1./ppi).*(1./dt)*10^(-3);
        v1(:,1) = v1(:,1).*(1./ppi).*(1./dt)*10^(-3);
        y2(:,1) = y2(:,1).*(1./ppi)*0.001;
        z2(:,1) = z2(:,1).*(1./ppi)*0.001;
        u2(:,1) = u2(:,1).*(1./ppi).*(1./dt)*10^(-3);
        v2(:,1) = v2(:,1).*(1./ppi).*(1./dt)*10^(-3);
        zdash   = unique(z1(:,1));
        ydash   = unique(y1(:,1));
         len_z   = length (zdash);
        len_y   = length (ydash);
        ********************** MATRIX FORM ***************************
   for j =len_z:-1:1
        for i = 1:1:len_y
        Y_CAM1(i,j)      = y1((j-1)*len_y+i);
        Z_CAM1(i,j)      = z1((len_z-j)*len_y + i);
                U_CAM1(i,j)      = u1((len_z-j)*len_y + i);
                V_CAM1(i,j)      = v1((len_z-j)*len_y + i);
        Tot_vel_CAM1(i,j) = sqrt( U_CAM1(i,j).^2+ V_CAM1(i,j).^2);
        Y_CAM2(i,j)      = y2((j-1)*len_y+i);
        Z_CAM2(i,j)      = z2((len_z-j)*len_y + i);
        U_CAM2(i,j)      = u2((len_z-j)*len_y + i);
        V_CAM2(i,j)      = v2((len_z-j)*len_y + i);
                 Tot_vel_CAM2(i,j) = sqrt( U_CAM2(i,j).^2+ V_CAM2(i,j).^2);
        End
    end
%********* ROTATE VECTORS TO ALIGN WITH PHYSICAL COORDINATES ****
   Y_PHY1 = Z_CAM1;
   Z_PHY1 = -1.*Y_CAM1 + (1252*(1./ppi)*0.001) ;
   U_PHY1 = V_CAM1;
   V_PHY1 = -1.*U_CAM1;
 %*************************************************************************
    Y_PHY2 = -1.* Z_CAM2 + (1052*(1./ppi)*0.001);
   Z_PHY2 = Y_CAM2;
   U_PHY2 = -1.* V_CAM2;
   V_PHY2 = U_CAM2;
   %*CONVERTING THE I ANF J COUNTER TO MATCH WITH  PHYSICAL SPACE *
    for j = 1:1:len_z
        for i = 1:1:len_y
        Y_TRANS1(i,j)=  Y_PHY1(i,j);
        Z_TRANS1(i,j) = Z_PHY1(len_y-(i-1),len_z-(j-1));
        U_TRANS1(i,j) = U_PHY1(len_y-(i-1),j);
                 V_TRANS1(i,j) = V_PHY1(len_y-(i-1),j);
                Z_TRANS2(i,j)=  Z_PHY2(i,j);
        Y_TRANS2(i,j) = Y_PHY2(len_y-(i-1),len_z-(j-1));
        U_TRANS2(i,j) = U_PHY2(i,len_z-(j-1));
        V_TRANS2(i,j) = V_PHY2(i,len_z-(j-1));
        Tot_vel__TRANS1(i,j) = sqrt(U_TRANS1(i,j).^2+V_TRANS1(i,j).^2);
        Tot_vel__TRANS2(i,j) = sqrt(U_TRANS2(i,j).^2+V_TRANS2(i,j).^2);
```

```
        end
    end
    % %******************** FOR STICHING/ CONCATENATING THE VECTORS
    U_CON = [U_TRANS1(1:end-1,1:end-6) U_TRANS2(2:end,4:end)];
    V_CON = [V_TRANS1(1:end-1,1:end-6) V_TRANS2(2:end,4:end)];
    [m n] = size(U_CON);
    dy_TRANS =  Y_TRANS1(1,2) - Y_TRANS1(1,1);
    dz_TRANS =  Z_TRANS1(2,1) - Z_TRANS1(1,1);
    Y_CON(1,1) = 0.0092;
    Z_CON(1,1) = 0.0052;
    for i = 1:1:m-1
        for j = 1:1:n-1
        Y_CON(i+1,j)  = Y_CON(i,j);
        Y_CON(i,j+1)  = Y_CON(i,j) + dy_TRANS ;
        Z_CON(i+1,j)  = Z_CON(i,j) + dz_TRANS;
        Z_CON(i,j+1)  = Z_CON(i,j);
        end
    end
    Y_CON(m,n) = Y_CON(m-1,n);
    Z_CON(m,n) = Z_CON(m,n-1);
    figure(1),contourf(Y_CON,Z_CON,sqrt(U_CON.^2 + V_CON.^2))
% ************************** INITIALIZATION OF REFINED GRID ***********%
    yini = Y_CON(1,1);
    yfin = Y_CON(1,n);
    zfin = Z_CON(m,1);
    zini = Z_CON(1,1);
    nptsj = len_y;
    nptsi = len_z;
    dy_delta = (yfin-yini)./(nptsj-1);
    dz_delta = (zfin-zini)./(nptsi-1);
    y0 = yini;
    z0 = zini;
    for j = 1:nptsj
       z0 = zini;
         for i = 1:nptsi
        yref(i,j) = y0;
                zref(i,j) = z0;
        z0 = z0 + dz_delta;
         end
     y0 = y0 + dy_delta;
    end
    %****************************** Grid Check Files **********************
    jpts = n;
    ipts = m;
    %************************* Interpolation Loop ***************************
    for jref = 1:1:nptsj
       for iref = 1:1:nptsi
          %********* Locate Refined Grid Cell Position inside Coarse Grid
          yval = yref(iref,jref);
          zval = zref(iref,jref);
          for j = 1:1:jpts-1
             if (Y_CON(1,j+1)>= yval)
                jcheck = j;
                break;
             end
          end
```

```
        for i = 1:1:ipts-1
           if (Z_CON(i+1,1)>= zval)
              icheck = i;
              break;
           end
        end
        %************ Declare Grid Reference in terms of Coarse Grid
        y1dash = Y_CON(icheck,jcheck);
        y2dash = Y_CON(icheck,jcheck+1);
        y3dash = Y_CON(icheck+1,jcheck);
        y4dash = Y_CON(icheck+1,jcheck+1);
        z1dash = Z_CON(icheck,jcheck);
        z2dash = Z_CON(icheck,jcheck+1);
        z3dash = Z_CON(icheck+1,jcheck);
        z4dash = Z_CON(icheck+1,jcheck+1);
         u1dash = U_CON(icheck,jcheck);
        u2dash = U_CON(icheck,jcheck+1);
        u3dash = U_CON(icheck+1,jcheck);
        u4dash = U_CON(icheck+1,jcheck+1);
        umxu = (u2dash-u1dash)*(yval-y1dash)/(y2dash-y1dash) + u1dash;
        umxl = (u4dash-u3dash)*(yval-y3dash)/(y4dash-y3dash) + u3dash;
        uint = (umxl-umxu)*(zval-z1dash)/(z3dash-z1dash) + umxu;
        uref(iref,jref) = uint;
        v1dash = V_CON(icheck,jcheck);
        v2dash = V_CON(icheck,jcheck+1);
        v3dash = V_CON(icheck+1,jcheck);
        v4dash = V_CON(icheck+1,jcheck+1);
        vmxu = (v2dash-v1dash)*(yval-y1dash)/(y2dash-y1dash) + v1dash;
        vmxl = (v4dash-v3dash)*(yval-y3dash)/(y4dash-y3dash) + v3dash;
        vint = (vmxl-vmxu)*(zval-z1dash)/(z3dash-z1dash) + vmxu;
        vref(iref,jref) = vint;
        totref_vel(iref,jref) = sqrt(uref(iref,jref).^2 + vref(iref,jref).^2);
      end
   end
%*************** Circulation/Vorticity Code Higher Order ******************
   dy = abs(yref(1,2)-yref(1,1));
   dz = abs(zref(2,1)-zref(1,1)) ;
   [UX,UY] = gradient(uref,dy,dz);
   [VX,VY] = gradient(vref,dy,dz);
   vor_z = (VX-UY);
%******* TO LOCATE THE VORTICITY CENTROID ****************************
   [minval(k) minloc(k)] = min(vor_z(:));
   [maxval(k) maxloc(k)] = max(vor_z(:));
   [minloc_row(k) minloc_col(k)] = ind2sub(size(vor_z), minloc(k));
   [maxloc_row(k) maxloc_col(k)] = ind2sub(size(vor_z), maxloc(k));
   i_min = minloc_row(k);
   j_min = minloc_col(k);
   i_max = maxloc_row(k);
   j_max = maxloc_col(k);
   ymin(k) = yref(i_min,j_min);
   zmin(k) = zref(i_min,j_min);
   ymax(k) = yref(i_max,j_max);
   zmax(k) = zref(i_max,j_max);
   dist(k) = ymax(k)- ymin(k);
   cen(k) = ymin(k)+ dist(k)/2;
   squared_v(k) = 0;
```

```
   for i = 1:1:nptsi
      for j= 1:1:nptsj
         squared_v(k) = squared_v(k) + ((totref_vel(i,j)).^2);
      end
   end
%********************************* KINETIC ENERGY *********
     K_E(k) = (squared_v(k))./((U_inf).^2) ;
%************************ FOR VORTEX WITH FORCING (LEFT)VORTEX
%*************CALCULATING MAXIMUM VELOCITY / RADIUS OF THE CORE *
%********************* IN THE POSITIVE X DIRECTION ***************************
   Vmax11 = totref_vel(i_min,j_min);
   jcounter1 = 1;
   for j = j_min:1:j_min+20
      if totref_vel(i_min,j)> Vmax11
         Vmax11 = totref_vel(i_min,j);
         r11core = jcounter1*dz;
      end
      jcounter1 = jcounter1+1;
      U1_0(jcounter1-1,1) = totref_vel(i_min,j);
      r_11core(jcounter1-1,1) = (jcounter1-1)*dz;
   end
%************************ IN THE NEGATIVE X DIRECTION*****************%
   Vmax12 = totref_vel(i_min,j_min);
   jcounter1 = 1;
   for j = j_min:-1:j_min-20
      if totref_vel(i_min,j)> Vmax12
         Vmax12 = totref_vel(i_min,j);
         r12core = jcounter1*dz;
      end
      jcounter1 = jcounter1+1;
      U1_180(jcounter1-1,1) = totref_vel(i_min,j);
      r_12core(jcounter1-1,1) = (jcounter1-1)*dz;
   end
%*********************** IN THE POSITIVE Y DIRECTION*******************
   Vmax13 = totref_vel(i_min,j_min);
   icounter1 = 1;
   for i = i_min:1:i_min+30
      if totref_vel(i,j_min)> Vmax13
         Vmax13 = totref_vel(i,j_min);
         r13core = icounter1*dy;
      end
      icounter1 = icounter1+1;
      U1_90(icounter1-1,1) = totref_vel(i,j_min);
      r_13core(icounter1-1,1) = (icounter1-1)*dy;
   end
%************************************ IN THE NEGATIVE Y DIRECTION
   Vmax4 = totref_vel(i_min,j_min);
   icounter1 = 1;
   for i = i_min:-1:i_min-10
      if totref_vel(i,j_min)>Vmax4
         Vmax4 = totref_vel(i,j_min);
         r14core = icounter1*dy;
      end
      icounter1 = icounter1+1;
      U1_270(icounter1-1,1) = totref_vel(i,j_min);
      r_14core(icounter1-1,1) = (icounter1-1)*dy;
```

```
    end
    V1max(k) = (Vmax11 + Vmax12 + Vmax13 )/3;
    r1core(k) = (r11core + r12core + r13core)/3;
    vorstrength1(k) = (V1max(k)*2*pi*r1core(k));
    % FOR VORTEX WITH NO FORCING(RIGHT)VORTEX **********************
%**CALCULATING MAXIMUM VELOCITY / RADIUS OF THE CORE
%*****IN THE POSITIVE X DIRECTION ***************************
    Vmax21 = totref_vel(i_max,j_max);
    jcounter2 = 1;
    for j = j_max:1:j_max+20
        if totref_vel(i_max,j)> Vmax21
            Vmax21 = totref_vel(i_max,j);
            r21core = jcounter2*dz;
        end
        jcounter2 = jcounter2+1;
        U2_0(jcounter2-1,1) = totref_vel(i_max,j);
        r_21core(jcounter2-1,1) = (jcounter2-1)*dz;
    end
%************************ IN THE NEGATIVE X DIRECTION*****************%
    Vmax22 = totref_vel(i_max,j_max);
    jcounter2 = 1;
    for j = j_max:-1:j_max-20
        if totref_vel(i_max,j)> Vmax22
            Vmax22 = totref_vel(i_max,j);
            r22core = jcounter2*dz;
        end
        jcounter2 = jcounter2+1;
        U2_180(jcounter2-1,1) = totref_vel(i_max,j);
        r_22core(jcounter2-1,1) = (jcounter2-1)*dz;
    end
%********* IN THE POSITIVE Y DIRECTION*******************
    Vmax23 = totref_vel(i_max,j_max);
    icounter2 = 1;
    for i = i_max:1:i_max+10
        if totref_vel(i,j_max)> Vmax23
            Vmax23 = totref_vel(i,j_max);
            r23core = icounter2*dy;
        end
        icounter2 = icounter2+1;
        U2_90(icounter2-1,1) = totref_vel(i,j_max);
        r_23core(icounter2-1,1) = (icounter2-1)*dy;
    end
%******** IN THE NEGATIVE Y DIRECTION *********%
    Vmax4 = totref_vel(i_min,j_min);
    icounter1 = 1;
    for i = i_min:-1:i_min-10
        if totref_vel(i,j_min)>Vmax4
            Vmax4 = totref_vel(i,j_min);
            r14core = icounter1*dy;
        end
        icounter1 = icounter1+1;
        U1_270(icounter1-1,1) = totref_vel(i,j_min);
        r_14core(icounter1-1,1) = (icounter1-1)*dy;
    end
    V2max(k) = (Vmax21 + Vmax22 + Vmax23 )/3;
    r2core(k) = (r21core + r22core + r23core)/3;
```

```
    vorstrength2(k) = (V2max(k)*2*pi*r2core(k));
    end
V1max = V1max'./U_inf;
V2max = V2max'./U_inf;
r1core = r1core./c;
r2core = r2core'./c;
r1core = r1core(r1core~=0);
r2core = r2core(r2core~=0);
vorstrength1 = vorstrength1'./(U_inf*c);
vorstrength2 = vorstrength2'./(U_inf*c);
vorstrength1 = vorstrength1(vorstrength1~=0);
vorstrength2 = vorstrength2(vorstrength2~=0);
 minval = (minval*c)./(U_inf);
 maxval = (maxval*c)./(U_inf);
ymin = ymin./c;
zmin = zmin./c;
ymax = ymax./c;
zmax = zmax./c;
ymin1 = ymin(ymin~=0);
zmin1 = zmin(zmin~=0);
ymax1 = ymax(ymax~=0);
zmax1 = zmax(zmax~=0);
V1max = V1max(V1max~=0);
V2max =V2max(V2max~=0);
minval = minval(minval~= 0);
maxval = maxval(maxval~= 0);
ymax1 = ymax1';
zmax1 = zmax1';
minval = minval';
maxval = maxval';
K_E = K_E';
K_E = K_E(K_E ~=0);
dist = dist';
dist = dist(dist~=0);
bmax = max(dist);
bmin = min(dist);
crowfactor = (bmax - bmin)/(bmax + bmin);
cmax = max(zmax1);
cmin = min(zmax1);
cmax1 = max(zmin1);
cmin1 = min(zmin1);
g1 = (cmax-cmin)./(cmax+cmin);
g2 = (cmax1-cmin1)./(cmax1+cmin1);
bmin = min(dist);
plot(ymin1 , zmin1,'r')
hold on
plot(ymax1 , zmax1,'c')
title('vorticity centroid locations-0.24 m/s-5 AOA-0hz,2.5deg');
xlabel('y/c');
ylabel('z/c');
legend('Vorticity centroid with time for left vortex','Vorticity centroid with time for right vortex')
axis([0 4 0 4]);
hold off

%%%%%%%%%%%%%%%%%%%%%%%%%%%%%%%%%%%%%%%%%%%%%%%%%%%%%%%%%%%%%%%%%%%%%%%%%%%%%%%
```